Dissertation

submitted to the
Combined Faculties for the Natural Sciences and for Mathematics
of the Ruperto-Carola University of Heidelberg, Germany
for the degree of
Doctor of Natural Sciences

by

Diplom-Physiker Patrick Gemünden
Born in Bad Kreuznach, Germany

Oral examination: 29th April 2015

Top-down Modeling of Hierarchically Structured Soft Matter: Liquid Crystalline Mesophases of Polymeric Semiconductors

Referees:	Prof. Dr. Kurt Kremer
	Prof. Dr. Ulrich Schwarz

Kurzzusammenfassung

In dieser Arbeit werden generische, teilchenbasierte Modelle für die Beschreibung von hierarchisch geordneter, polymerischer weicher Materie entwickelt, deren makroskopische Struktur mit mikroskopischen, molekularen Eigenschaften verknüpft ist. Dazu wird ein *Top-down*-Ansatz verwendet, um makroskopische Eigenschaften wie beispielsweise das generelle Phasenverhalten zu reproduzieren. Methodisch werden die Modelle ausgehend von effektiven Funktionalen (Hamiltonfunktion) entwickelt, die von lokalen skalaren und tensoriellen Ordnungsparametern abhängen, um flüssigkristalline (FK) Phasen zu beschreiben.

Elastische Eigenschaften von nematischen FK Polymerschmelzen werden untersucht. Als eines der Hauptresultate wird in der Simulation eine lineare Abhängigkeit der Frank elastischen Spreizkonstante von der Kettenlänge gemessen, was die Auflösung eines Widerspruchs in bestehenden theoretischen Vorhersagen nahelegt.

Des Weiteren wird ein Modell zur Beschreibung der Morphologie von polymerischen Halbleitern auf großer Längenskala am Beispiel des Moleküls Poly-(3-Hexylthiophen) (P3HT) entwickelt. Die Modellierung der lamellaren, teilkristallinen Morphologie von realem P3HT wird im ersten Schritt für die weniger geordnete FK Phase entwickelt. Die nicht-gebundenen Modellwechselwirkungen sind weich und anisotropisch, wobei zusätzliche biaxiale Symmetrie die lokale Molekülarchitektur und die π-Wechselwirkungen generisch beschreibt. Makroskopische Materialeigenschaften, z.B. die Abhängigkeit des isotrop-nematischen Übergangs von der Kettenlänge, werden reproduziert. Die

Morphologien werden in Hinblick auf Landungstransporteigenschaften untersucht.
Im letzten Teil der Arbeit wird ein Multiskalenansatz zur Wiedereinführung von atomistischen Details entwickelt.

Abstract

This thesis addresses the development of generic, particle-based models for hierarchically structured polymeric soft matter, in which the macroscopic structure is linked to microscopic, molecular properties. The models are developed in a *top-down* approach, tailored to reproduce macroscopic properties of the real system, such as the general phase behavior. Methodologically, the models are derived from effective functionals (Hamiltonians) that depend on local scalar and tensorial order parameters, capturing liquid crystalline (LC) phases. The elastic properties of nematic LC polymer melts are studied. As one of the main results, a linear scaling of the splay Frank elastic constant with the chain length is found in the simulations, providing evidence for resolving a disagreement of existing theoretical predictions.

Subsequently, a model is developed describing the large-scale morphology of polymeric semiconductors, as a test case for poly(3-hexylthiophene) (P3HT). The modeling of the lamellar, semi-crystalline morphology of real P3HT is, in a first step, developed for the less ordered LC phase. The non-bonded model interactions are soft and anisotropic, with additional biaxial symmetry capturing generically the anisotropy of the molecular architecture and the π-stacking interactions. Macroscopic features of the real material, such as the dependence of the isotropic-nematic transition on the chain length, are reproduced. The morphologies are analyzed with respect to charge transport related properties.

In the last part of the thesis, a multiscale scheme for the reconstruction of atomistic detail is presented.

List of related publications

[1] Gemünden, P.; Poelking, C.; Kremer, K.; Andrienko, D.; Daoulas, K. C.: Nematic Ordering, Conjugation, and Density of States of Soluble Polymeric Semiconductors. *Macromolecules*, **2013**, 46, 5762–5774 (cover article).

[2] Gemünden, P.; Daoulas, K. C.: Fluctuation Spectra in Polymer Nematics and Frank Elastic Constants: A Coarse-Grained Modelling Study. *Soft Matter*, **2015**, 11, 532–544.

[3] Gemünden, P.; Poelking, C.; Kremer, K.; Daoulas, K. C.; Andrienko, D.: Effect of Mesoscale Ordering on the Density of States of Polymeric Semiconductors. *Accepted for publication in: Macromolecular Rapid Communications*, **2015**, DOI: 10.1002/marc.201400725.

Contents

1 Introduction

1.1 Motivation

Soft condensed matter concerns our everyday life. Most of our food is soft matter, and so are, for example, rubber and soap. These materials can be deformed with moderate force and their macroscopic properties can neither be classified as simply liquid-like nor as purely solid-like.
Soft matter consists of large molecules. In many cases, these molecules are polymers, i.e. molecules which are composed of a large number of repeated, covalently linked subunits.

The large scale structures and dynamics of soft matter are governed by weak intermolecular forces on the order of the thermal energy k_BT (about 2.5 $\frac{kJ}{mol}$ at room temperature). Therefore, thermal fluctuations are sufficient to significantly change the structure of the material. Often, for entropic reasons, the macromolecules exhibit spontaneous self-organization into complex, ordered structures.

These structures in soft matter systems may occur hierarchically, ranging from length scales comparable to the size of a single molecule to higher order, super-molecular scales. Typical examples are the spontaneously formed nanometer-sized patterns found in block-copolymer systems, or the hierarchical assembly of lipid molecules into membranes in biological materials.

Fig. 1.1c shows a (model) system of a membrane structure, which itself organizes into spherical super-structures (vesicles).

Since a molecule may consist of several hundreds or thousands of atoms, the typical length scales at which self-organizing structures occur are large from the microscopic (atomistic) point of view. For the same reason, collective, super-molecular assembly is observed on large time scales, i.e. on scales of seconds to days or years.

One way of studying complex soft matter systems, besides the experiment and analytical theory, is to investigate them with computer simulations. Usually, one formulates a computer model in terms of a set of idealized degrees of freedom and interactions (e.g. defining interactions between atoms with a *force-field*) and, based on these, derives macroscopic system properties with the tools of statistical mechanics ("computer experiments") [4]. The rapid development of modern computers in the last decades permits an investigation of models with increasing complexity. Nevertheless, large structures and slow processes in complex soft matter are often still far from length and time scales which can be accessed with well-developed, conventional simulation schemes. In light of this, soft matter modeling has benefitted from the development of coarse-graining techniques in order to account only for the relevant physical processes involved and neglect unnecessary details.

Conceptually, coarse-graining is a process to "average out" certain local details and thereby reduce the number of degrees of freedom which describe a system (see Fig. 1.1 for an illustration of the successive reduction of details in order to describe the same system at different levels of resolution).

In the molecular simulation community, several variants thereof have been proposed over the past years. Coarse-graining schemes help to turn the intractable problem of sampling large systems "brute force" with techniques on the level

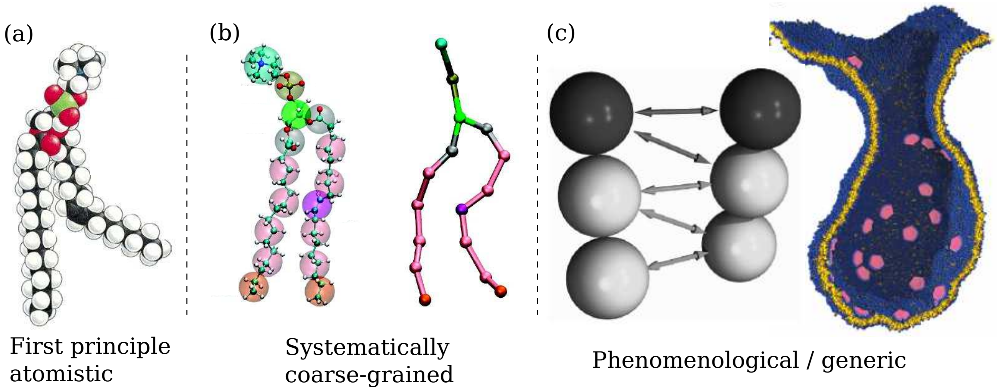

Figure 1.1: Scheme which illustrates the concept of coarse-graining for the example of a lipid bilayer membrane. (a) Atomistically resolved lipid molecule (From Ref. [5]). (b) Systematically coarse-grained model of a lipid (From Ref. [6]). (c) Generic representation of lipids with only a few beads, used for studying collective phenomena in lipid bilayers on large scales (From Ref. [7]).

of atoms into that of sampling a reduced set of (coarse-grained or collective) degrees of freedom, evolved by simple, effective interactions (coarse-grained force-field).

The major challenge is to find a suitable set of such coarse degrees of freedom and to define the effective interactions accordingly.

In this respect, systematic strategies have been proposed, in order to "derive" coarse-grained models solidly based on statistical mechanics [8–15]. They usually combine an explicit analytical mapping of atoms on the coarse-grained sites with the calculation of effective interactions from an atomistic reference system, i.e. force field. Once the coarse-grained model is parameterized, quantitative results may in principle be obtained from simulations thereof.

Balancing the degree of coarse-graining with the ability to describe certain phenomena of interest, e.g. self-assembly or, in general, large scale phenomena, is difficult within an ansatz focussed on deriving effective interactions *bottom-up* from the atomistic force fields. In some situations, atomistic reference simulations might not be feasible, e.g. simply because an accurate atomistic force-field is not known. Furthermore, for the simulation of macroscopic phase separation or self-assembly, where the bulk structure can change during the simulation, effective interactions usually cannot be transferred between thermodynamic states [16]. It is, for example, difficult to find an effective coarse-grained potential which generates reliable predictions for the same system at different temperatures.

In these cases, models are frequently developed phenomenologically, capturing only some key aspects of the described real system and reproducing a desired macroscopic (thermodynamic) property or phase behavior. The molecular representation and, in particular, the molecular architecture in such frameworks is generic, i.e. coarse-grained degrees of freedom are not explicitly connected to atomistic coordinates. Still, the parameterization of the model can be matched with the thermodynamic behavior of the real system. Even though not easy to categorize, the latter strategies are often called *top-down* methods, emphasizing the fact that certain effective interactions are imposed directly on a coarse level of description in order to reproduce macroscopic behavior. This is conceptually different from the previously discussed bottom-up schemes, which are based on atomistic reference data. If no parameter matching is involved at all, i.e. when a model is *generic*, one can still learn about general physical concepts which govern macroscopic behavior of soft matter systems.

Phenomenological, generic molecular modeling is frequently guided by the assumption of scale separation, a concept applying to various soft materials. Scale separation refers to the case when the structure and dynamics on large length and time scales (e.g. center-of-mass packing and motion) is independent of the underlying microscale (e.g. atomistic structure and vibrations). This concept has been of central importance for the development of simple models for long-chain polymeric systems. In these systems, the chain connectivity introduces long range correlations to the material. As a consequence, the length scale on the order of the average extension of a chain can be distinguished from the atomistic Ångström scale, falling *in between* the microscopic scale of atoms and the macroscopic length scale. It is therefore typically called *mesoscale*. Interestingly, for long chains in solution, properties on the mesoscale, such as the scaling of the average chain extension with its length, have been found independent of microscopic details and interactions. Therefore, simple, minimal models based on generic chain connectivity and excluded volume repulsion are often used [17, 18]. Simple assumptions which guide such generic modeling schemes are supported by experimental validations [19, 20]. Eventually, the macroscopic description of long chain polymer solutions with minimalistic models found a rigorous theoretical justification based on arguments from renormalization group theory applied to polymer chains [21, 22].

Nevertheless, in many cases in which models have to be reasonably coarse to allow the study of relevant processes, and the described real system is at the same time reasonably complex, scale separation may not hold. In other words, in such cases, features on the macroscale may emerge from properties on the fine scale, which are readily "averaged out" in the coarse model representation. Thus, microscopic and macroscopic properties may be coupled strongly.

Chain stiffness, sub-molecular architecture and/or directionality of interactions, for example, may lead to the formation of long-ranged partial order (i.e., *liquid crystalline* order) on macroscopic length scales. Clearly, the key molecular features leading to the macroscopic ordering have to be incorporated in a generic model. Only in that way, it can account for the macroscopic phase behavior of the system. Since, as already discussed, systematic linking of such fine scale features to macroscopic properties can be challenging, the development of phenomenological models therefore relies to some extent on intuition.

One way to address complex structured systems with simple phenomenological models is to *impose* an effective energy landscape on the level of a functional of local order parameters, i.e. to define an effective Hamiltonian based on collective variables. Such concepts are known from classical density functional theory (DFT) of liquids [23, 24], assuming that the free energy of the system can be written as a functional of local density fields.
For polymers, for example, top-down modeling of relatively simple systems with Edwards-type Hamiltonians is frequently used [18]. Therein, chain connectivity is modeled by the connection of discrete segments with harmonic potentials ("Gaussian thread"), while repulsive interactions between segments are expressed as a simple functional of local segment density. These generic approaches are traditionally focussed on density as the local order parameter, i.e. they are used to capture systems with positional order, but without orientational order.
However, phenomenological functionals may be written in terms of more complex order parameters, in the spirit of phenomenological Landau-de Gennes free energy expansions [25–27]. In that way, one can account for more complex structuring and phase behavior, e.g. capturing liquid crystalline ordering or crystallization. A natural choice of order parameters which capture increasing complexity of a system is the sequence of liquid crystalline order parameters [27, 28].

The aim of this thesis is to develop generic, particle-based simulation schemes for hierarchically structured polymer systems that are linked to the microscopic scale, based on simple, effective functionals of liquid crystalline order parameters.

An advantage of such simulation schemes is given by the fact that, for simple functionals, models based on collective order parameters (field-based representation) can be explicitly connected to a particle-based representation [29–35]. This allows the sampling with standard particle-based simulation schemes, such as Molecular Dynamics simulation or Monte Carlo simulation. Starting from the most simple case of nematic liquid crystalline polymers, a major development presented in this thesis is the incorporation of a biaxial-nematic order parameter in such functional-based approaches. In that way, one can capture an additional planar packing of molecules in a generic way. Following the sequence of amorphous to nematic to biaxial order, the presented modeling schemes will be applied to a real polymeric material.

1.2 Outline

The linking element across the chapters in this thesis is the top-down modeling strategy based on phenomenological functionals. However, the systems this strategy is applied to are diverse. Therefore, the following outline gives - for each study - a very brief overview of the physical systems and questions addressed in a first step, and the methodological framework by which they are studied in a second step. An overview of the underlying, conceptual modeling schemes is provided in chapter 2.

In chapter 3, nematic liquid crystalline systems are investigated. While those systems present the most simple case of liquid crystalline order, nematic polymers exhibit a wealth of fascinating structural and elastic properties, which distinguish them from similar liquid crystalline systems containing small molecules (short mesogenes). The focus in this chapter is on the investigation of Frank elastic constants in nematic polymer systems, motivated by the fact that the functional form of their dependence on the length of the polymer chains has not yet been addressed rigorously in simulations.

Conceptually, a model is developed in which generic nematic coupling is introduced by a functional that depends on the nematic order parameter. From this functional, a particle-based simulation scheme is subsequently derived. Since this approach allows the equilibration of nematic mesophases on large scales, an answer to the question how the Frank constants depend on the length of the polymer will be given.

In chapter 4, the focus is shifted on more complex ordered systems, namely the morphology of conjugated polymer systems used in organic electronics (OE) applications. Fig. 1.2a depicts a blend of poly(3-hexylthiophene) (P3HT) and PCBM, which are both typical representatives of OE materials. P3HT conducts charges along its relatively stiff backbone. It has short side chains attached for imposing solubility (see Fig. 1.2d). The structure of P3HT in the solid state is complex, with biaxially oriented backbones in lamellar-like crystalline stacks (planar orientation of flat aromatic rings), see Fig. 1.2c. Ordered domains themselves are embedded in an inhomogeneous morphology of either

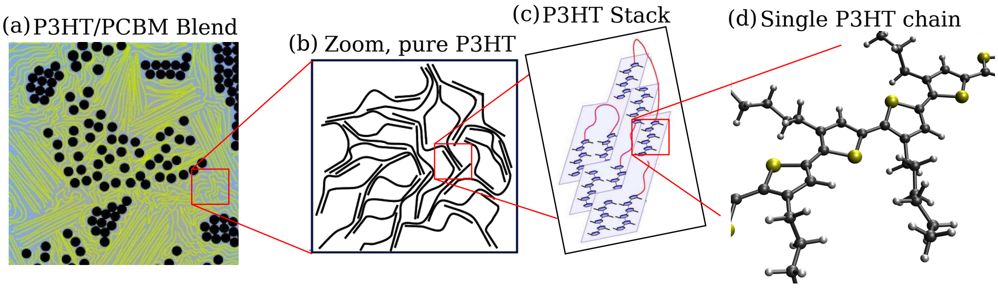

Figure 1.2: Schematic of the hierarchical structure of a P3HT/PCBM blend. (a) Illustration of phase separated morphology, with pure and intermixed domains (From Ref. [36]) (b) Zoom into the structure, representing a pure P3HT domain, with visible amorphous and partially crystalline domains (From Ref. [37]) (c) Further zoom into a crystalline stack of P3HT chains (From Ref. [38]) c) Single atomistic structure of a P3HT molecule.

amorphous or partially ordered regions (illustrated in Fig. 1.2b).
Within the modeling framework of this thesis, the semi-crystalline structure of P3HT is approached starting in the first step from a less ordered representation, describing biaxial liquid crystalline phases. The model is able to capture the sequence of amorphous via uniaxial to biaxial-nematic liquid crystalline ordering. The phenomenological interactions are combined with a sampling of chain conformations using a systematic coarse-graining approach. Therefore, the obtained morphologies can be investigated with respect to charge transfer related properties. The influence of long-range mesoscale order on the energetic landscape, for example, is subsequently studied. The chapter concludes with a brief presentation of first attempts to address the more complex system of P3HT/PCBM blends, i.e. the structure shown in Fig. 1.2a.

Chapter 5 is directly connected to the questions addressed in chapter 4. Starting from there, a refined version of the modeling approach is presented. Because of the sampling of realistic P3HT chain conformations combined with explicit information on the polymer segment (hexylthiophene) orientations, the generated morphologies discussed in ch. 4 are well suited for successively restoring local atomistic details (*backmapping*).
To reach this goal, however, fine scale calculations are not directly feasible due to a local overlap of segments and hence a resulting spatial overlap of charges. The problem is approached by a three-step scheme, successively reiterating the coarse-grained morphologies with more refined models. A “medium scale”, systematically coarse-grained model is presented, in order to adjust the local packing of the system towards the real target structure. Eventually, the study of the influence of the morphology on the energetic landscape in ch. 4 is revisited, now within a more precise, atomistically resolved level of detail.

2 Modeling approaches - an overview

The advantages and limitations of a specific soft matter modeling approach depend on the focus of the investigation. In addition to the difficulty of choosing an approach which is tailored to a specific question, it seems already challeng-

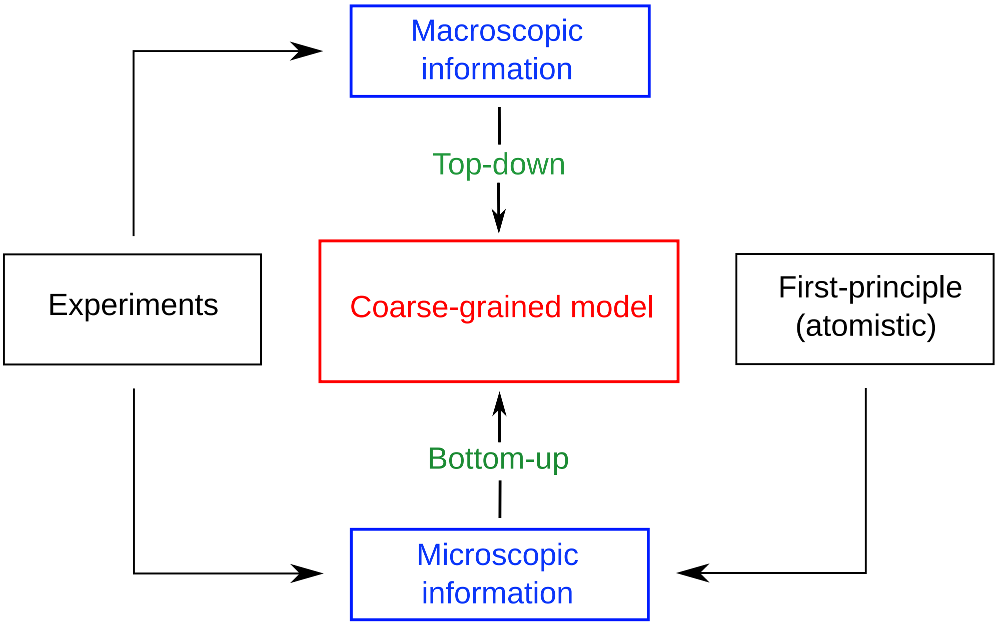

Figure 2.1: Scheme, illustrating different categories of modeling approaches. Distinctions are not sharp and modern multiscale treatments incorporate many different aspects (at once).

ing to categorize the available modeling strategies. The variety of concepts and labels thereof is diverse. In recent reviews on the topic [10, 14, 39–42], this diversity has been reflected equally.

The categorization into bottom-up and top-down approaches, as already introduced in ch. 1, is probably one of the most rigorous conceptual distinctions. The modeling approaches which are discussed in this chapter follow this classification.

Bottom-up schemes generally rely on information from a finer scale (compare Fig. 2.1). In computational modeling, on the one hand, this information is often obtained from a model at a finer resolution. In coarse-graining applications on molecular systems, the fine scale model is typically represented by an atomistic force field. On the other hand, bottom-up modeling can be build on experimental data. Structure-based bottom-up methods may use information on the local liquid structure of a fluid, for example. Ch. 2.1 reviews some major developments in the field of bottom-up coarse-graining. Among the methods which are reviewed, the structure-based methods are presented in sec. 2.1.2 in most detail, since these methods are used in this thesis.

Top-down methods do not depend on information about an underlying finer scale. They are are tailored to reproduce macroscopic properties, for example thermodynamic observables and phase behavior (see Fig. 2.1). They are not necessarily linked explicitly to a finer resolution. In this sense, they are build phenomenologically. As discussed in detail in the following chapters, top-down models, derived on a coarse description level, can frequently be linked to field-based models because of the possibility for a dual representation in terms of particles and (collective) fields. In ch. 2.2, a brief overview of top-down approaches in molecular modeling is discussed. The main focus is put on field-based modeling approaches, i.e. the use of collective order parameter fields for imposing a generic thermodynamic behavior on a molecular model. The underlying links between a particle-based and a field-based model description are reviewed in sec. 2.2.3. Such links of a particle-based model to a field-based description are used at many stages in this work.

2.1 Bottom-up methods

For many applications in soft matter modeling, an essential prerequisite for a coarse-grained (CG) model is the quantitative reproduction of reference data, either obtained from a model on finer scale or from an experiment. Further, one may want to "hand over" obtained structures from a CG simulation to a finer scale description with minimal approximation, i.e. to work with a model which has a "close" connection to the reference system.

In this chapter, approaches are reviewed which can collectively be labeled *bottom-up* coarse-graining strategies [9–15]. Bottom-up coarse-graining literally implies an underlying fine scale of material description. This had initially been intended when the term coarse-graining was first used in the physics community to describe the process of "averaging out" fine degrees of freedom [43].

On the one hand, the possibility to generate specific reference data (with high accuracy) in a controlled way is an advantage of computer simulations over experiments. Complex microscopic information may in some cases be difficult to extract from experiments, and so may be the control and quantification of the errors in the experimental reference data. On the other hand, deriving a quantitatively "correct" model from a more refined (atomistic) model is limited by the accuracy of the parameterization of the latter, i.e. by the accuracy of the atomistic force field.

For bottom-up strategies, the reference system typically contains atomistic

degrees of freedom, while the CG description is based on, for example, the centers-of-masses of groups of atoms as the CG degrees of freedom. Frequently, as in the center-of-mass example, CG degrees of freedom (or interaction sites) are explicitly connected to the atomistic coordinates. The connection between atomistic and CG degrees of freedom can be formalized by the definition of a mapping operator, as it has been presented in a series of publications about the attempt to cast the systematic bottom-up coarse-graining into a solid statistical mechanics framework [12, 13, 41].
Following a systematic description [15, 44], an atomistic configuration, given by a set of atomistic coordinates $\boldsymbol{r}^N = \{\boldsymbol{r}_1, \ldots, \boldsymbol{r}_N\}$, is linked to a CG configuration, defined by a set of interaction site coordinates $\boldsymbol{R}^n = \{\boldsymbol{R}_1, \ldots, \boldsymbol{R}_n\}$, via a mapping operator $\boldsymbol{M}$,

$$\boldsymbol{R}^n = \boldsymbol{M}\boldsymbol{r}^N. \tag{2.1}$$

If the atomistic, fine detailed system is described with a potential energy function $u(\boldsymbol{r}^N)$, and the CG system equivalently with a CG potential $U(\boldsymbol{R}^n)$, finding a model potential can be motivated with the rigorous condition of equal probabilities of states in both representations, i.e. by claiming [13]

$$e^{-U(\boldsymbol{R}^n)/k_BT} \propto \int d\boldsymbol{r}^N e^{-u(\boldsymbol{r}^N)/k_BT} \delta\left(\boldsymbol{M}\boldsymbol{r}^N - \boldsymbol{R}^n\right). \tag{2.2}$$

The relation in eq. 2.2 can be seen as the formal manifestation of the process to “average out” fine scale degrees of freedom when coarse-graining.
When imposing the link between the CG and the atomistic potential, eq. 2.2, the CG potential is interpreted as a potential of mean force (PMF). This is a multibody effective potential which describes the interaction between CG sites as if they were generated by the underlying atomistic force field (compare also Ref. [45] for a rigorous discussion of effective interactions). In this way, the coarse-grained sampling by default reproduces all thermodynamic

and structural observables with respect to the CG mapping sites, in particular all correlation functions.

While the PMF will be formally introduced and discussed in sec. 2.1.2 (it will become clear why the potential is connected to a *mean force*), some general aspects will already be discussed here. Since the effective interaction arises from the removal or integration of fine (atomistic) degrees of freedom, the PMF incorporates entropic contributions. Thus, by default, the effective potential is temperature or state point dependent. Consequently, even if the full many-body effective potential was known, it might be difficult to use it at different thermodynamic states or even across areas in the phase diagram in which a transition is expected [14, 16].

2.1.1 Force matching

The *force matching* method [41, 46] is only briefly motivated here. In that framework, the connection of interactions between atoms (atomistic force-field) and interactions between coarse-grained sites (CG force-field) is developed on the level of forces, following a variational minimization of the residual

$$\chi^2(\boldsymbol{F}^{CG}) = \frac{1}{3N}\langle\sum_{l=1}^{N}|\boldsymbol{F}_l^{CG}(\boldsymbol{M}\boldsymbol{r}^N) - \boldsymbol{F}_l^{AA}(\boldsymbol{r}^N)|^2\rangle, \tag{2.3}$$

which is a functional of the CG force field $\boldsymbol{F}^{CG}$. $\boldsymbol{F}_l^{AA}$ is the effective force on a site l in the atomistic representation, derived from the atomistic force field, while $\boldsymbol{F}_l^{CG}$ is the effective force on the same site in the CG representation, derived from the CG force field, respectively [41]. The yield of such systematic *force matching* [46] methods is a tabulated CG force field, which can be implemented directly with standard Molecular Dynamics (MD) simulation packages, such as GROMACS [47], LAMMPS [48], or ESPResSo/ESPResSo++ [49, 50]. An implementation of the *force matching* technique can be found, for example, in the coarse-graining software package VOTCA-CSG [44]. The method is closely related to the optimization of a CG potential with respect to correlation functions (structure-based coarse-graining) [51, 52].

2.1.2 Structure-based coarse-graining

In the following, structure-based coarse-graining techniques are discussed [11, 53–55]. In order to do so, some fundamental terms from statistical mechanics are introduced first. A convenient choice of the statistical ensemble in molecular simulations is the canonical ensemble, where the probability of finding a system of N indistinguishable particles in a microstate $\boldsymbol{r}^N = \{\boldsymbol{r}_1, \ldots, \boldsymbol{r}_N\}$ is proportional to the Boltzmann-weight

$$W(\boldsymbol{r}^N) = e^{-\beta H\left(\boldsymbol{r}^N\right)}, \tag{2.4}$$

with $\beta = \frac{1}{k_B T}$. The value of the function $H\left(\boldsymbol{r}^N\right)$ at the state point $\boldsymbol{r}^N$ is the total energy of the system, and H is the Hamiltonian, here written in the most general form of an N-body potential. The probability of a microstate $\boldsymbol{r}^N$ is then given by the probability function $P^{(N)}(\boldsymbol{r}^N) = \frac{W(\boldsymbol{r}^N)}{Z}$, which is normalized by the configurational partition function

$$Z = \frac{1}{N!} \int W(\boldsymbol{r}^N) d\boldsymbol{r}^N, \tag{2.5}$$

where $d\boldsymbol{r}^N = d\boldsymbol{r}_1 \ldots d\boldsymbol{r}_N$. Note that here only the configurational part of the partition function is considered, i.e., momenta are not included.

Correlation functions and potential of mean force

Following standard textbooks [24, 56, 57], one can define a hierarchy of conditional probabilities for finding a specific (smaller) set of n particles by

$$P^{(n)}(\boldsymbol{r}^n) = \int P^{(N)}(\boldsymbol{r}^N) d\boldsymbol{r}^{N-n}. \tag{2.6}$$

For later convenience, this is often written as the n-particle distribution functions

$$n^{(n)}(\boldsymbol{r}^n) = \frac{N!}{(N-n)!} P^{(n)}(\boldsymbol{r}^n). \tag{2.7}$$

The prefactor in eq. 2.7 is chosen under the assumption of indistinguishable particles, hence it corrects for the permutation of a subset of n particles among the full set of N particles. For eq. 2.7, this gives the intuitive interpretation of a probability of finding *any* subset of n particles at (or close to) the coordinates $\boldsymbol{r}^1, \ldots, \boldsymbol{r}^n$, irrespective of their permutation among those coordinates. An important quantity for later use is the two-particle distribution

$$n^{(2)}(\boldsymbol{r}_1, \boldsymbol{r}_2) = N(N-1) \int P^{(N)}(\boldsymbol{r}^N) d\boldsymbol{r}^{N-2}. \tag{2.8}$$

This distribution function can be related to a spatial correlation function $g(\boldsymbol{r}_1, \boldsymbol{r}_2)$ by

$$n^{(2)}(\boldsymbol{r}_1, \boldsymbol{r}_2) = n^{(1)}(\boldsymbol{r}_1) n^{(1)}(\boldsymbol{r}_2) g(\boldsymbol{r}_1, \boldsymbol{r}_2). \tag{2.9}$$

In an isotropic system, $g(\boldsymbol{r}_1, \boldsymbol{r}_2) = g(r = |\boldsymbol{r}_1 - \boldsymbol{r}_2|)$ only depends on the spatial distance between the particles. The function g is called the radial distribution function (RDF). In a macroscopically homogeneous and spatially isotropic system there is a more convenient writing: $g(r) = \frac{V^2}{N^2} n^{(2)}(\boldsymbol{r}_1, \boldsymbol{r}_2)$. Hence, it follows that

$$g(r) = \frac{V^2(N-1)}{NZ} \int W_N(\boldsymbol{r}^N) d\boldsymbol{r}^{N-2}. \tag{2.10}$$

The subsequent discussion is borrowed from textbooks [56, 57] in order to step through the following statistical problem: Choosing a molecule, which is labeled for convenience with index 1 and coordinates $\boldsymbol{r}_1$, one can ask for the average force acting on this molecule due to the contributions from *all* other molecules as a function of the distance of molecule 1 from a second molecule 2 with coordinates $\boldsymbol{r}_2$.
The force on molecule 1 is defined as $F_1(\boldsymbol{r}^N) = -\frac{\partial H(\boldsymbol{r}^N)}{\partial \boldsymbol{r}_1}$. Its conditional average in the canonical ensemble when molecule 1 is at position $\boldsymbol{r}_1$ and molecule 2 at position $\boldsymbol{r}_2$ is given by

$$\langle F_1(\boldsymbol{r}_1, \boldsymbol{r}_2)\rangle = \frac{\int \left(-\frac{\partial H(\boldsymbol{r}^N)}{\partial \boldsymbol{r}_1}\right) W_N(\boldsymbol{r}^N) d\boldsymbol{r}^{N-2}}{\int W_N(\boldsymbol{r}^N) d\boldsymbol{r}^{N-2}}. \tag{2.11}$$

From the expression eq. 2.11, the average force on molecule 1 as a function of the pair distance $r = |\boldsymbol{r}_1 - \boldsymbol{r}_2|$ can be written as the derivative of a function U_{MF}, which is frequently introduced in statistical mechanics as the (two-particle) potential of mean force (PMF), drawn from the relation

$$\langle F_1(r)\rangle_= - \frac{\partial U_{MF}(r)}{\partial r}. \tag{2.12}$$

This function can be connected to the pair correlation function eq. 2.10 by substituting the definitions from eqs. 2.8-2.10 into eq. 2.12, yielding

$$g(r) = e^{-\frac{U_{MF}(r)}{k_B T}}. \tag{2.13}$$

Note that in the limit of low density, the PMF in eq. 2.12 converges to the potential energy of the two particles. However, in cases of a finite system density, the configurations of the surrounding particles give rise to an entropic contribution and the PMF is therefore state dependent, i.e. it depends on temperature and density. Eq. 2.11 can be similarly written in a more general way as an average force $F_1(\boldsymbol{r}^n)$ acting on molecule 1 as a function of the configuration $\boldsymbol{r}^n$ of a (finite) set of n particles. In that way, the many-particle PMF is defined by [56]

$$F_1(\boldsymbol{r}^n) = -\frac{U_{MF}(\boldsymbol{r}^n)}{\partial \boldsymbol{r}_1}. \tag{2.14}$$

For bottom-up coarse-graining applications, in which a number of N fine (atomistic) degrees of freedom are mapped onto n CG degrees of freedom, the optimal solution for an effective CG potential can formally be also seen as an n-particle PMF. This PMF corresponds to the effective free energy of the set of n CG degrees of freedom, which is generated by integration over the atomistic degrees of freedom, as a function of their configuration $\boldsymbol{R}^n$ (compare eq. 2.2). In practical coarse-graining applications, one is restricted to approximations of this multi-dimensional potential.

Boltzmann-Inversion

The relationship between the two-particle potential of mean force, depending on the pair distance, and the radial distribution function in the previous section can be generalized. The distribution of any independent CG degrees of freedom, which may be, for example, a CG bond length b or bond and torsional angles θ and ϕ [8], can be related to the Boltzmann weights of appropriate effective potentials U_b, U_θ and U_ϕ. Thus, for the probability distributions, the following relations apply [8]:

$$p(\gamma) \propto e^{-U_\gamma(\gamma)/k_BT}, \ \gamma = b, \theta, \phi. \tag{2.15}$$

The coarse-grained potentials are subsequently estimated by inverting the probability functions eqs. 2.15 [8],

$$U_\gamma = -k_B T \ln p(\gamma),\ \gamma = b, \theta, \phi. \tag{2.16}$$

This method is frequently applied in polymer simulations, for which the probability distributions are obtained, for example, from an atomistic reference simulation [8, 54].

Iterative Boltzmann-Inversion

The Iterative Boltzmann-Inversion (IBI) is a standard algorithm for approximating a *pairwise* potential in order to reproduce the RDF of pairs. The IBI is designed for solving the problem of deriving model potentials from given structural data, i.e. correlation functions [11, 58]. The available data can be obtained from diffraction experiments, or, similarly, from a reference computer simulation. In experiments, a convenient way of accessing useful structural information is to measure the structure factor from diffraction experiments and then perform a Fourier transformation of the result in order to obtain the pair correlation function.

If structural data for $g(r)$ is given as a reference, the pair potential can be obtained from an iterative process. If a pair potential reproducing a certain RDF exists, a theorem derived by Henderson [59] states that such a potential is unique. However, in practical applications this statement has to be taken with care. It is not obvious how deviations of the RDF data propagate into the derived potential, i.e. how statistical fluctuations in a real sample of an RDF influence the resulting model potential [44, 52].

A convenient choice of an initial guess for the potential can be

$$U_{\text{pair}}(r) = -k_B T \ln[g(r)], \tag{2.17}$$

which gives a good approximation for dilute systems, in which the entropic contribution to the pair potential of mean force is small. Subsequently, the configuration of the system can be updated with some method of choice, usually in a short MD simulation, in which the potential guess is used for calculating the forces. From the resulting configuration, the instantaneous pair correlation in step *i*, $g_i(r)$, is measured and the pairwise potential is updated prior to the next iteration, via

$$U_{i+1}(r) = U_i(r) + k_B T \ln \frac{g_i(r)}{g(r)}. \tag{2.18}$$

The algorithm is converged if the instantaneous distribution $g_i(r)$ equals the target distribution $g(r)$.

Usually, some care has to be taken with respect to the equilibration of the configuration in the individual iteration cycles. Slowly evolving observables, as for example chain conformations on the level of the contour length in polymer simulations, should in principle be relaxed during all iteration steps. Nevertheless, relaxation on relatively short length scales usually is sufficient. In order to test this assumption, convergence is usually checked after a reasonably large amount of iteration cycles by performing a long test simulation with the calculated potential. If the potential has been converged sufficiently, the structure does not change during this run.

2.1.3 Other approaches

Similar to force matching, the *relative entropy* approach [60, 61] is a variational scheme. Within this method, the residual which is minimized is based on the relative probability distribution of the coarse-grained site configuration, obtained from mapping in the all-atom picture (which is called target in the original Ref. [60]), and the respective configuration generated by the coarse-grained potential after mapping (which is called model in Ref. [60]). The residual reads

$$S_{\text{rel}}(U_{CG}) = \int d\boldsymbol{r}^N p^{AA}(\boldsymbol{r}^N) \ln \left[\frac{p^{AA}(\boldsymbol{r}^N)}{p^{CG}(\boldsymbol{M}\boldsymbol{r}^N, U_{CG})} \right] , \tag{2.19}$$

where $p^{AA}(\boldsymbol{r}^N)$ is the probability of the target configuration and $p^{CG}(\boldsymbol{M}\boldsymbol{r}^N)$ the one for the model configuration, respectively. The label AA stands for all atoms. U_{CG} is the effective coarse-grained potential.

Another prominent example for deriving effective CG potentials is the Inverse Monte Carlo method [53], which yields an approximation of the PMF from an iterative cycle of short CG simulations.

The approaches which have been discussed so far are strategies for deriving a CG representation of a system in order to investigate it at a coarse level of detail. It is briefly mentioned here that recent strategies of “true” multiscale treatments have been proposed (AdResS and H-AdResS adaptive resolution simulation schemes) [42, 62–64]. In these approaches, certain areas of a systems are described in detail, while other, less interesting areas, are treated on a coarse level. These methods are similar to the concept of using a magnifying glass on the interesting part of a system.

2.2 Top-down methods

Following a different route, models can be optimized to quantitatively reproduce macroscopic properties without putting a direct link to an underlying finer

scale. This is frequently called a *top-down* modeling approach.
Conceptually, the idea of reversing the deterministic nature of physical theories in order to *a posterio* derive (molecular) model parameters top-down from macroscopic experimental reference data is not new. Early efforts in this direction used the experimentally available equation of state data in order to obtain simple models for an underlying molecular interaction potential, hence to derive a more intuitive picture of the interactions of molecules [56, 65]. One famous example is the early work of Lennard-Jones on determining simple molecular model potentials for argon [66].
A more recent example, used mainly for biomolecular simulations, is the MARTINI force field [67]. In this case, the force field involves a set of interaction parameters fitted to available experimental data.

Models which are optimized for matching thermodynamic properties of a specific system are often lacking a correct local (liquid) structure compared to the real system. The model is not referring to a fine level of description, i.e. underlying chemical details and molecular architecture. Some "hybrid" approaches try to remedy this lack of structural accuracy by refining structural aspects of the target system at the same time [68].
As it will be demonstrated in this work, the "lack" of local structural accuracy is even an advantage in many cases. Often, top-down models focus more on the phenomenological point of view and require a relatively coarse molecular representation. By incorporating more and more fine scale details into a few coarse-grained interaction sites, the effective interactions become softer. Thus, (partial) overlap of segments is possible [34, 69]. This can be seen intuitively at the example of a polymer chain: Locally, atomistic degrees of freedom interact via a harsh excluded volume repulsion. However, if many atoms are incorporated into a single coarse-grained interaction site, a pair of the latter interaction sites may be allowed to approach very small spatial separations, since such configurations may still be consistent with a large number of underlying

microscopic configurations [45]. This is not only physically meaningful, since averaging over many "hard" (atomistic) interactions softens the magnitude and distance dependence of effective interactions, but also improves significantly the sampling efficiency with standard algorithms, for example Molecular Dynamics (MD) or Monte Carlo (MC) schemes.

Besides using thermodynamic data for the systematic parameterization of effective potentials, models can be based exclusively on *generic* principles, e.g. symmetry or polarity of molecules, connectivity or stiffness, or a general phase behavior. In principle, a purely generic approach may be distinguished from more systematic top-down strategies by the fact that for generic models, no parameters are matched to real systems. However, this categorization is not rigorously used, and top-down, generic and phenomenological approaches are sometimes used as synonyms.

Generic strategies can be useful in order to study the behavior of a model system as a representative of a class of real systems, for example the dependence of system properties on parameterization. Besides having proved to be useful in the field of classical polymer theory [17, 18, 21, 70], as already discussed in the introduction, generic models are used for studying the self-assembly process of lipid bilayers in biological systems [40, 71, 72].

2.2.1 Phenomenological models

Conceptually, one may call any physical theory phenomenological: There is always an underlying, more detailed description level, and the theory loses its validity outside a certain regime of time and length scales or beyond a specific class of problems. Thermodynamics is a subject which evolved historically in a phenomenological fashion. By deduction from experiments, a consistent theory was established which describes a system, e.g. a gas or a liquid, in terms of a closed set of thermodynamic potentials (energies or free energies) and relations, linking the potentials to thermodynamic state variables ("caloric equations of state") or linking variables with each other ("thermal equations of state").

Statistical mechanics connects the macroscopic, phenomenological description and the underlying system of an extremely large number of particles, or, in other words, fine degrees of freedom. Computer simulations allow the integration of the microscopic equations of motion of a reasonably large ensemble of particles. Thereby, one can derive macroscopic quantities such as temperature, pressure, or transport coefficients, or the equations of state thereof directly. However, from the modeling point of view, if one is mostly interested in large scale system properties such as the thermodynamic phase behavior, one may use models focussed on a phenomenological, macroscopic level of description.

Field-theoretic simulation concepts for soft matter and polymer systems reflect this spirit [18, 73–76]. The idea is to describe a system on the level of fields, i.e. collective degrees of freedom, which can be for example the density of a liquid or a more complex order parameter field. The equilibrium configurations of such fields are then obtained from the generalized thermodynamic forces which propagate the field configurations.

In the following sections, a framework is discussed to characterize a system with an effective interaction functional in terms of collective variables (fields), which depends on a few phenomenological parameters, such as the compressibility of species or an immiscibility parameter in the case of multicomponent fluids.

Historically, simple expressions of the free energy in terms of order parameters were frequently postulated in mean-field theories for the investigation of phase transitions, such as the Ginzburg-Landau model [77] in superconductor theory. Further examples for a description based on phenomenological free energy functionals are the Flory-Huggins theory of polymer solutions

[17, 78, 79] and the more recently developed phase field models [80] based on the Cahn-Hilliard functional expansion of the interfacial free energy [81].
A more complete collection of phenomenological mean-field theories can be found in Ref. [82], and a large collection of original references in the context of polymer theory in Ref. [74].

2.2.2 Field-theoretical framework

In this paragraph, some frequently used basic mathematical expressions in field-theoretic frameworks are discussed. The starting point is a set of f real order parameter fields $\rho_i\left(\boldsymbol{x}\right)$, $i = 1, \ldots, f$, which describe the system of interest. Those fields depend on the position $\boldsymbol{x}$ in three-dimensional Euclidean space. The relevant degrees of freedom in such a representation are the values of all the fields at each point in space. Thus, one can write down a partition function for the system as a functional integral over all possible field configurations,

$$Z = \int \prod_i \mathfrak{D}\rho_i\left(\boldsymbol{x}\right) e^{-\beta \mathfrak{F}(\{\rho_i(\boldsymbol{x})\})}, \tag{2.20}$$

with $\beta = \frac{1}{k_B T}$ and $\mathfrak{F}$ a functional of the fields.[1] From statistical physics, the free energy of the system is given by $F = -\frac{1}{\beta}\ln Z$.
Suppose now, the order parameter fields were averaged over sub-volumes in space in order to obtain average fields which are smooth and stationary. Stationarity is given when typical fluctuations in the order parameter fields appear on much smaller length scales than the length scale on which the averaging is performed. The latter scale may be, for example, a mesh width which divides the space into a number of subvolumes.
One can consider the following example: Suppose a homogeneous mixture of two species, e.g. a mixture of two distinct types of polymers in the regime

---

[1] For details about the field-theoretic formalism, the book of Chaikin and Lubensky, Ref. [82], was a helpful source for the author.

where the intermixed phase is thermodynamically stable (i.e. no macroscopic phase separation is observed). Taking a look at the local density distribution of the different species, one notes that they are inhomogeneously distributed, since the local density is correlated due to the chain connectivity. If one was interested in the density distribution of the two different monomers at assumed length scales comparable to or larger than the average size of a polymer coil, such correlations should have decayed to zero, meaning that one observes a homogenous density distribution. Now, even if the local conformations of chains in the system were changed, the averaged density would not change. Thus, on the large scale, the equilibrium representation of the system is given by a single configuration of the field, the equilibrium density fields $\overline{\rho}_i(\boldsymbol{x})$.
For eq. 2.20, the functional integral is then equal to the value of its integrand at a single position in the field coordinate space, thus

$$Z = e^{-\beta \mathfrak{F}(\{\overline{\rho}_i(\boldsymbol{x})\})}, \tag{2.21}$$

where, in more general terms, $\overline{\rho}_i(\boldsymbol{x})$ are the equilibrium configurations of the order parameter fields. Under this assumption, the functional $\mathfrak{F}$ equals the free energy F of the system, thus $\mathfrak{F}\left(\{\rho_i\left(\boldsymbol{x}\right)\}\right) = F\left(\{\overline{\rho}_i(\boldsymbol{x})\}\right)$. Even if the order parameter fields were not strictly stationary, the integral (eq. 2.20) would in some cases be well approximated by a single term which contributes most to the exact integral. Such a candidate for $\rho_i(\boldsymbol{x})$ can be formally obtained from a minimization principle,

$$\left.\frac{\delta \mathfrak{F}\left(\rho_i\left(\boldsymbol{x}\right)\right)}{\delta \rho_i\left(\boldsymbol{x}\right)}\right|_{\rho_i(\boldsymbol{x})=\overline{\rho}_i(\boldsymbol{x})} = 0, \tag{2.22}$$

for $i = 1, \ldots, f$. This leads to the approximation $F\left(\{\overline{\rho}_i(\boldsymbol{x})\}\right) \approx \mathfrak{F}\left(\{\overline{\rho}_i(\boldsymbol{x})\}\right)$, known as the saddle-point approximation.

2.2.3 Dual representation with particles and fields

In the following derivations, a system is composed of n interacting polymers, each consisting of N monomers with coordinates $\boldsymbol{r}_i(s)$ specified by the label of the chain $i = 1, \ldots, n$ and the monomer label $s = 1, \ldots, N$ relative to each chain. The total number of monomers in the system is denoted by $\tilde{N} = nN$ and the abbreviated notations $\boldsymbol{r}^{\tilde{N}} = \{\boldsymbol{r}_1(1), \ldots, \boldsymbol{r}_n(N)\}$ and $d\boldsymbol{r}^{\tilde{N}} = d\boldsymbol{r}_1(1) \cdot d\boldsymbol{r}_1(2) \cdots d\boldsymbol{r}_n(N)$ are used. The configurational part of the canonical partition function reads

$$Z = \frac{1}{n!} \int d\boldsymbol{r}^{\tilde{N}} e^{-\beta H\left(\boldsymbol{r}^{\tilde{N}}\right)}. \tag{2.23}$$

In macromolecular modeling approaches, interactions are frequently decomposed into bonded and non-bonded contributions [14], i.e. $H = H_{\text{b}} + H_{\text{nb}}$. Bonded contributions, in field-theoretical approaches, are usually assumed simple functions of the monomer coordinates. In the (discrete) Gaussian chain model for example,

$$H_{\text{b}} = \frac{3k_BT}{2b^2} \sum_{i=1}^{n} \sum_{s=1}^{N} \left(\boldsymbol{r}_i(s) - \boldsymbol{r}_i(s+1)\right)^2. \tag{2.24}$$

Another example is the worm-like chain model, which is often used for mesoscopic modeling of semi-flexible chains (more details will follow in chapter 3). In order to transform the statistical mechanics into a statistical field theory [75], one can define a local density operator

$$\hat{\rho}(\boldsymbol{x}) = \sum_{i}^{n} \sum_{s}^{N} \delta(\boldsymbol{x} - \boldsymbol{r}_i(s)), \tag{2.25}$$

which connects the local density to the *microscopic* degrees of freedom, i.e. the monomer coordinates $\boldsymbol{r}_i(s)$. In the following, the non-bonded interaction is assumed to be pairwise additive, which means one can write

$$H_{\text{nb}} = \frac{1}{2} \sum_{i=1}^{n} \sum_{s=1}^{N} \sum_{l=1}^{n} \sum_{m=1}^{N} u\left(\boldsymbol{r}_i(s), \boldsymbol{r}_l(m)\right). \tag{2.26}$$

With eq. 2.25, the non-bonded interaction can be rewritten in terms of the local density operator:

$$\begin{aligned} H_{\text{nb}} &= \frac{1}{2} \sum_{i=1}^{n} \sum_{s=1}^{N} \sum_{l=1}^{n} \sum_{m=1}^{N} \int d\boldsymbol{x} \int d\boldsymbol{x}' \delta(\boldsymbol{x} - \boldsymbol{r}_i(s)) u\left(\boldsymbol{x}, \boldsymbol{x}'\right) \delta(\boldsymbol{x}' - \boldsymbol{r}_l(m)) \\ &= \frac{1}{2} \int d\boldsymbol{x} \int d\boldsymbol{x}' \hat{\rho}(\boldsymbol{x}) u\left(\boldsymbol{x}, \boldsymbol{x}'\right) \hat{\rho}(\boldsymbol{x}'). \end{aligned} \tag{2.27}$$

The equivalent representation of H_{nb} in eq. 2.27 can be seen as a *functional* which depends on a collective variable (in this case the local density), which is derived from the underlying microscopic coordinates.

In a second step towards a field-theoretical description, one can formally rewrite the partition function, eq. 2.23, by using delta functions [74, 75]:

$$\begin{aligned} Z &= \frac{1}{n!} \int \mathfrak{D}\rho \int d\boldsymbol{r}^{\tilde{N}} \delta\left(\rho - \hat{\rho}\right) e^{-\beta H_{\text{b}} - \frac{\beta}{2} \int d\boldsymbol{x} \int d\boldsymbol{x}' \hat{\rho}(\boldsymbol{x}) u(\boldsymbol{x}, \boldsymbol{x}') \hat{\rho}(\boldsymbol{x}')} \qquad (2.28) \\ &= \frac{1}{n!} \int \mathfrak{D}\rho \int \mathfrak{D}w e^{i \int d\boldsymbol{x} w \rho + n \ln Z_{SC}(iw) - \frac{\beta}{2} \int d\boldsymbol{x} \int d\boldsymbol{x}' \rho(\boldsymbol{x}) u(\boldsymbol{x}, \boldsymbol{x}') \rho(\boldsymbol{x}')}, \end{aligned}$$

with $Z_{SC}(iw) = \int d\boldsymbol{r}^N e^{-\frac{3}{2b^2} \sum_{s=1}^{N} (\boldsymbol{r}(s) - \boldsymbol{r}(s+1))^2 - i \sum_{s=1}^{N} w(\boldsymbol{r}(s))}$ the partition function of a single chain interacting with the imaginary field $iw(\boldsymbol{x})$. In the last step, the integral representation of the delta function was used, i.e.

$$\delta\left(\rho - \hat{\rho}\right) = \int \mathfrak{D}w e^{i \int d\boldsymbol{x} w (\rho - \hat{\rho})}, \tag{2.29}$$

where $w(\boldsymbol{x})$ is an auxiliary real scalar field [74, 75]. Thus, one has derived an expression of the partition function which solely depends on the fields ρ and w, i.e.

$$Z = \frac{1}{n!} \int \mathfrak{D}\rho \int \mathfrak{D}w e^{-\beta\mathfrak{F}(\rho,w)}. \tag{2.30}$$

With eq. 2.30, the statistical mechanics in terms of n interacting chains is formally rewritten in terms of decoupled chains interacting with fluctuating fields ρ and w. This is the starting point for the rich field of polymer field theories [73–76, 83] and numerical (approximate) solutions thereof, such as the self-consistent field approach [73, 74, 76].
Self-consistent field theories, applied to polymeric (multi-component) systems, use eq. 2.30 as a starting point for a series of saddle point approximations, see eq. 2.22, which leads to a set of self-consistent field equations that can be solved with standard numerical techniques [74, 75].

Despite a description completely in the field picture as sketched above, the first step towards the particle-field transformation, eq. 2.27, can in many cases already be useful for an efficient sampling of the particle-based formulation of the configurational integral, i.e. eq. 2.23 in combination with the expressions of interactions in eq. 2.24 and eq. 2.27. Guided by the concepts of classical density functional theory (DFT), the expression of the non-bonded interaction in eq. 2.27, reformulated as a functional of local field (collective) variables, motivates to *assume* an (approximate) functional expression in terms of collective variables for the definition of interactions (also for the derivations in this section, a specific form of the interactions was assumed, i.e. eq. 2.26, which is not a prerequisite). Eq. 2.24 together with the non-bonded energy functional

$$H_{\text{nb}}/k_B T = \frac{v}{2} \int d\boldsymbol{x} [\hat{\rho}(\boldsymbol{x})]^2 \tag{2.31}$$

is the well-known (discrete) Edwards model [18, 84] for a system of interacting chains. The non-bonded energy functional can be seen to arise from a virial expansion and v is related to the excluded volume parameter, which has to be positive in order to define a physically meaningful model. The expression is directly related to the energy functional eq. 2.27 through the specific representation of the pair potential, which in this case is a short-ranged delta-potential, i.e. $u\left(\boldsymbol{r}_i(s), \boldsymbol{r}_l(m)\right) = \delta\left(\boldsymbol{r}_i(s) - \boldsymbol{r}_l(m)\right)$. It is shown in the following chapters how such a one-to-one correspondence translates to the more complex case of, for example, orientation-dependent interactions.

2.2.4 Grid-based vs. off-lattice evaluation

The non-bonded energy functional, as a function of collective variables, has frequently been used for particle-based simulations, e.g. standard Monte Carlo sampling of the statistical mechanics defined by 2.23. In doing so, the involved delta-functions, which connect the microscopic degrees of freedom (the monomer coordinates) with the collective field variables, are problematic for a direct implementation.

A possible work-around is the discretization of space into a collocation grid and to assort the monomers to grid nodes by a specified collocation scheme. Various implementations have been used, from simple collocation to the nearest grid point to a Gaussian distribution of a particle to a set of neighboring grid nodes [29, 30, 85–87]. Such algorithms are well known from the field of electrostatics calculations [88–90].

For particle-based simulations, grid-based implementations can be very efficient, since the non-bonded interactions are obtained without the use of a pair list. This is due to the fact that the integral, eq. (2.31), turns into a simple summation over grid cells, and hence the total non-bonded energy is in the same way discrete, i.e. can be written as a summation over grid cells. It should be noted that the grid spacing introduces a length scale in the system which can

be interpreted as an interaction range. The approach can then be seen as a "regularization" of the zero-ranged delta potential.
In the past, several variants of such methods were applied successfully to morphology studies of block-copolymers and other multi-component and/or branched chain systems [29–31, 85–87]. In some systems, however, such collocation schemes may generate artifacts when applied to certain geometries [91] or more elaborated shapes of microscopic interactions, e.g. liquid-crystalline coupling, since the introduction of a grid breaks the rotational invariance of the simulation space. Nevertheless, for relatively simple uniaxial-nematic systems and a coarse chain representation, the lattice version of the above approach can still be useful for obtaining insight into generic properties of liquid-crystalline morphologies [69].

Another way of evaluating non-bonded interactions is to work with a continuous (i.e. smooth) representation of the local density field eq. 2.25 by assigning density clouds to the monomers, which then build up the density field. Therefore, we define a "smoothed" version of the local operators by a weighting procedure,

$$\hat{\Phi}_\omega(\boldsymbol{x}) = \int d\boldsymbol{x}' \omega(|\boldsymbol{x} - \boldsymbol{x}'|) \hat{\rho}(\boldsymbol{x}'), \tag{2.32}$$

with ω being a kernel or weight function. The function ω is the formal representation of the density cloud. The specific form of ω is arbitrary, but it has to be normalized. The procedure exhibits similarities with the weighted or smoothed density approach in classical DFT [23, 24, 92].

Taking the simple functional eq. 2.31 as an example, one can show that replacing the local density operator eq. 2.25 in eq. 2.31 by the weighted local density operator eq. 2.32, given that the choice of ω is made explicit, uniquely defines a pair potential [32–34, 93, 94]. This can be seen by transforming the functional back to the pairwise potential representation after replacing the operator,

$$\frac{H_{\mathrm{nb}}}{k_{\mathrm{B}}T} = \frac{v}{2}\sum_{i}^{n}\sum_{s}^{N}\sum_{l}^{n}\sum_{m}^{N}\int d\boldsymbol{x}\omega\left(|\boldsymbol{x}-\boldsymbol{r}_i(s)|\right)\omega\left(|\boldsymbol{x}-\boldsymbol{r}_l(m)|\right), \qquad (2.33)$$

with

$$\int d\boldsymbol{x}\omega(|\boldsymbol{x}-\boldsymbol{r}_i(s)|)\omega(|\boldsymbol{x}-\boldsymbol{r}_l(m)|) \equiv v(\boldsymbol{r}_i(s), \boldsymbol{r}_l(m)). \qquad (2.34)$$

The same procedure can in principle be repeated for the higher order expansion terms in the functional, e.g. terms cubic in the local density, in order to derive three- and more-body interactions [32]. As will be shown later, for a simple analytic choice for ω, the pair potential can be derived analytically by solving the integral in eq. 2.34.

As a conclusion, it is pointed out that the density cloud approach and the grid-based method are connected directly. A density cloud representation and the corresponding model can, in principle, be recovered exactly from the grid-based model. This is achieved by choosing a spherical collocation scheme in combination with the limit of infinitely fine grid spacing. Thus, the grid-based implementation can be seen as a method which approximates the evaluation of the overlap integral in eq. 2.34 numerically. While the grid-based method has the advantage of allowing sampling without a pair list, the grid-less method avoids potential artifacts, while still retaining the explicit connection to the interaction functional. This offers a transparent control of thermodynamic properties on the functional level [35]. Furthermore, standard particle-based simulation methods, such as implemented in the GROMACS Molecular Dynamics package [47], can be used readily once the integral in eq. 2.34 is solved analytically.

3 Nematic polymers - studied with soft, generic models

Parts of this chapter are based on the following article:
P. Gemünden and K. Ch. Daoulas, "Fluctuation Spectra in Polymer Nematics and Frank Elastic Constants: A Coarse-Grained Modelling Study", Soft Matter, 11, 532-544 (2015).

In this chapter, elastic properties of nematic liquid crystalline polymers (LCP) will be studied with a particle-based generic model. A nematic LCP melt is the first example of partially ordered soft matter addressed in this thesis. The study is motivated by the fact that there are only very few experimental or computational investigations of the specific elastic properties (e.g. Frank elastic constants [95, 96]) of nematic LCP [97–99], especially for polymer melts [100]. From analytical theory, however, several predictions for the elastic properties of LCP from simple model calculations exist [101–108]. Following these predictions, LCP have an unusually strong response to splay deformations, giving rise to material properties extraordinarily different from those of small-molecule liquid crystals.

In simulations, generating and analyzing large equilibrated LCP mesophases is challenging with first-principle, particle-based simulation schemes because of large system sizes, suggesting the use of models operating on a coarse-grained level. In the literature, single-site interaction models have been proposed, for example the off-lattice Gay-Berne-type models [109–111] and the efficient lattice-based Lebwohl-Lasher model [112–114]. In the Gay-Berne model, particles interact off-lattice with a harsh repulsive core of ellipsoidal shape [109]. The Lebwohl-Lasher model is the direct implementation of the Maier-Saupe coupling between nearest neighbors on a cubic lattice [112].

In this chapter, a generic off-lattice polymer model which has been introduced in Ref. [69] is developed further in order to study elastic properties of LCP. The model accounts for anisotropic single-site interactions between polymer segments and is directly derived from a functional based on local density and nematic order parameters [69]. Such a connection facilitates the tuning of macroscopic system properties, i.e. the phase behavior (see ch. 2.2 and in particular ch. 2.2.3).
Large-scale nematic mesophases have been equilibrated and subsequently analyzed to obtain density and director fluctuation spectra, which are directly connected to macroscopic elastic properties, e.g. Frank elastic constants. It will be shown that these spectra can be described by generic functional forms proposed by available analytical theories [104–108, 115]. Eventually, the dependence of the Frank elastic constants on the chain length will be discussed. From the simulations, evidence will be provided for a linear scaling of the splay constant with chain length, which is in agreement with the description from Meyer [103] and following theoretical considerations [104–106, 108, 116].

3.1 Background

A liquid crystal (LC) is a fascinating example of mesoscale ordering in soft matter. Literally, the term liquid crystal refers to the non-trivial appearance of a material which is neither conventionally liquid-like nor crystalline, but

shares features with both "traditional" phases. A liquid crystal is, compared to an isotropic liquid, partially ordered. Therefore, a liquid crystalline mesophase generally has a lower symmetry than the isotropic phase.
This was first experimentally observed in systems which have special optical properties within a certain temperature range [117, 118]. Usually, one distinguishes between thermotropic and lyotropic liquid crystals, depending on whether the temperature or the molar relative concentration is the main driving force for a liquid crystalline phase transition, i.e. the transition of a system from a disordered, isotropic mesophase to a partially ordered, LC mesophase.

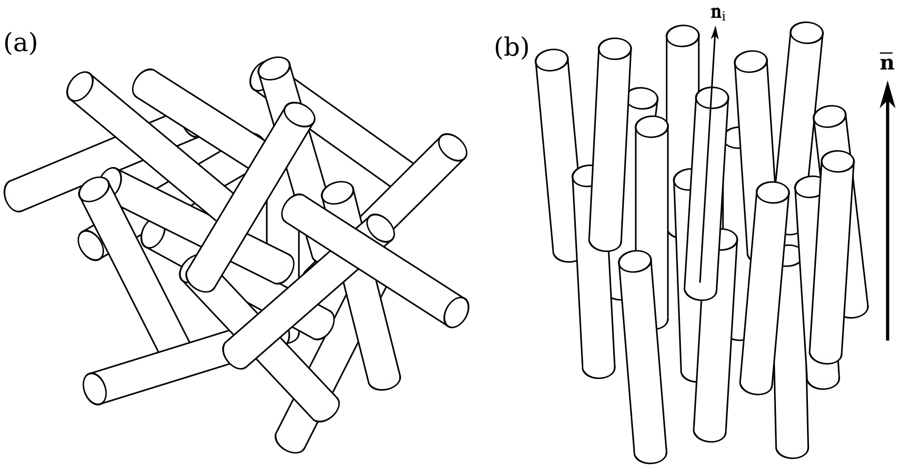

Figure 3.1: Schematic, illustrating (a) isotropic and (b) nematic alignment of molecules with their symmetry axis $\boldsymbol{n}_i$ along a common direction $\overline{\boldsymbol{n}}$, called the macroscopic nematic director.

In a nematic LC, molecules have the tendency to align along a common spatial direction, which is called the macroscopic nematic director, denoted by the vector $\overline{\boldsymbol{n}}$. Fig. 3.1 illustrates the molecular alignment in a nematic LC. Not entirely intuitive, for lyotropic systems the entropy can *increase* when changing to a spatially more ordered phase. Taking a closer look, one notes that the molecules which align along the director gain translational entropy, while in the direction perpendicular to the director the system remains in a liquid-like state. For LCP, the internal flexibility of molecules adds up to a subtle balancing between translational and configurational entropy in the system, i.e. the chain stiffness influences the phase behavior additionally.

An early phenomenological statistical mechanics description of lyotropic liquid crystals goes back to Onsager [119], who developed an approximate solution for a classical system of elongated molecules interacting via a harsh contact potential which arises from the geometrical overlap (excluded volume) of particles.

Later, Maier and Saupe [120] showed that for thermotropic liquid crystals, within a mean-field calculation, the transition to a nematic phase can be explained solely with anisotropic dispersion forces, i.e. a deviation of the molecular electrical field from that of a point source. Contributions to the intermolecular potential up to dipol-dipol interactions have been considered, with the interaction between a pair of particles with index i and j

$$v_{ij} = \left(\frac{3}{2} cos^2(\theta) - \frac{1}{2} \right), \tag{3.1}$$

in which θ is the angle between the respective dipole axes. Within the respective treatment, eq. 3.1 is the dominant contribution driving the isotropic-nematic phase transition.

The expression in eq. 3.1 is used for quantifying anisotropic coupling in simple models capturing nematic order [26, 69, 121–124]. The model introduced in this chapter is in a similar spirit.

In real systems, the consideration of either only long-ranged London (dipolar attractive) dispersion forces in the case of Maier-Saupe theory or only short-ranged repulsive forces in the case of Onsager theory is certainly an oversimplification [125]. In modeling studies, one usually accounts for a combination of both orientation and distance dependent contributions, with a potential derived from the product of the two contributions [110, 126–129].

Quantifying liquid crystalline nematic order

For a system of molecules which exhibits nematic order, the expression eq. 3.1 arises as a measure of the molecular orientation with respect to a fixed reference director $\overline{\boldsymbol{n}}$. This can be seen when expanding the orientational distribution function of the molecular axis, with respect to the director, in the orthogonal basis set of Legendre polynomials and subsequently truncating after the first non-trivial even term [28],

$$\begin{aligned} f(\boldsymbol{n}_i \cdot \overline{\boldsymbol{n}}) &= \frac{1}{2} + \frac{5}{2}\langle P_2 \rangle P_2\left(\boldsymbol{n}_i \cdot \overline{\boldsymbol{n}}\right) + \mathcal{O}\left((\boldsymbol{n}_i \cdot \overline{\boldsymbol{n}})^4\right) \\ &= \frac{1}{2} + \frac{5}{2}\left\langle \frac{3}{2}cos^2(\boldsymbol{n}_i \cdot \overline{\boldsymbol{n}}) - \frac{1}{2} \right\rangle \left(\frac{3}{2}cos^2(\boldsymbol{n}_i \cdot \overline{\boldsymbol{n}}) - \frac{1}{2}\right) + \ldots . \end{aligned} \tag{3.2}$$

Odd terms in the expansion eq. 3.2 have been omitted, since here only *apolar* nematic phases are considered, i.e. an exchange $\overline{\boldsymbol{n}} \rightarrow -\overline{\boldsymbol{n}}$ leaves the system unchanged. The vectors $\boldsymbol{n}_i$ and $\overline{\boldsymbol{n}}$ are normalized, i.e. $|\boldsymbol{n}_i| = |\overline{\boldsymbol{n}}| = 1$. Angular brackets denote an ensemble average. For the *apolar* case, nematic order can be quantified with a symmetric traceless tensor of rank two - the nematic order tensor, which is defined locally as

$$Q_{\alpha\beta}\left(\boldsymbol{r}\right) = \rho_0^{-1} \sum_{i,s}^{n,N} q_{i,\alpha\beta}\left(s\right) \delta\left(\boldsymbol{r} - \boldsymbol{r}_i\left(s\right)\right), \tag{3.3}$$

with the molecular orientation tensor defined as

$$q_{i,\alpha\beta}\left(s\right) = \frac{3}{2} n_{i,\alpha}\left(s\right) n_{i,\beta}\left(s\right) - \frac{\delta_{\alpha\beta}}{2}. \tag{3.4}$$

The quantity $n_{i,\alpha}(s)$ is the α-component of the molecular director $\boldsymbol{n}_i(s)$. The additional parameter s is introduced for later convenience for the more general case of labeling polymer segments. It is not important for the discussions in this section. Performing an average over space,

$$\langle Q_{\alpha\beta}\rangle = \frac{1}{V}\int d\boldsymbol{r} Q_{\alpha\beta}(\boldsymbol{r}) = \frac{1}{nN}\sum_{i,s}^{n,N} q_{i,\alpha\beta}(s), \tag{3.5}$$

in which $\boldsymbol{r}_i(s)$ labels the coordinates of a segment, one can extract both the macroscopic director and the order parameter from eq. 3.5. The tensor in eq. 3.5 is diagonal in the eigenframe which is aligned with the macroscopic director, i.e. the average direction of molecules. It has the diagonal form

$$Q_{\alpha\beta} = \mathrm{diag}\left(S, -\frac{S}{2}+T, -\frac{S}{2}-T\right). \tag{3.6}$$

The parameter

$$S = \left\langle \frac{3}{2}(\boldsymbol{n}_i(s)\cdot\overline{\boldsymbol{n}})^2 - \frac{1}{2}\right\rangle_{i,s} \tag{3.7}$$

is the macroscopic nematic order parameter, where $\langle\cdot\rangle_{i,s}$ denotes an average over all segments. The additional parameter T quantifies the deviation of the nematic phase from cylindrical symmetry. It is nonzero for biaxial mesophases, which will be the subject of chapter 4. Thus, with standard numerical tools it is possible to extract information about the director and the degree of order in a nematic system by performing an eigenvector and eigenvalue analysis of the tensor eq. 3.5.

Local fluctuations of nematic orientation

In a liquid crystal, the nematic director is in general not a constant in space. This is because excitations of director fluctuations at various wave lengths are excited at finite temperature, allowing a further reduction of entropy in a system. Thus the director, viewed as a spatially fluctuating field $\boldsymbol{n}(\boldsymbol{x})$, is composed of natural fluctuation modes whose amplitudes as a function of wave length bare interesting information about the response or stiffness of the material to deformations.

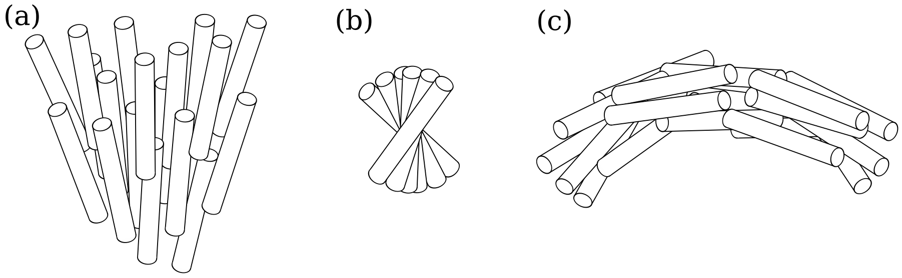

Figure 3.2: Scheme, illustrating the fundamental excitations of the director field. (a) Splay deformation, described with the Frank constant K_1. (b) Twist deformation, quantified with K_2. (c) Bend deformation, corresponding to K_3.

The three fundamental deformations in a three-dimensional bulk system are the splay, twist and bend distortions, see Fig. 3.2. A continuum theory established by Oseen [95] and Frank [96] connects the geometrical director distortions, i.e. the three Frank constants, to a free energy. If the modulation of the director field is weak and the director is a smoothly varying quantity in space, this free energy is written as

$$F_n = \frac{1}{2} \int d^3\boldsymbol{x} \left\{ K_1 (\nabla \cdot \boldsymbol{n})^2 + K_2 (\boldsymbol{n} \cdot (\nabla \times \boldsymbol{n}))^2 + K_3 (\boldsymbol{n} \times (\nabla \times \boldsymbol{n}))^2 \right\} . \tag{3.8}$$

K_1, K_2 and K_3 are the Frank elastic constants. The first, K_1, quantifies splay elastic behavior, while K_2 and K_3 correspond to twist and bend deformations, respectively. The free energy is an expansion up to second order in even terms of the gradient of the director field. For a slowly varying field, one can assume that eq. 3.8 is the dominant contribution to the distortion free energy

[25, 100, 130]. Close to point defects or confining walls, the approximation leading to eq. 3.8 is no longer appropriate [131, 132]. Aiming at a tool for measuring fluctuation spectra in order to determine the Frank elastic constants, a general relation between the director fluctuation modes and the material constants is now briefly reviewed.

Material properties and fluctuation spectra

Material constants such as the compressibility are in general related to large wave length fluctuation modes of a corresponding microscopic quantity. For the example of compressibility, this is the density. The Frank elastic constants are in the same way connected to the local nematic director. Given a system is strongly ordered (in the context of polymer nematics, this is to assume stretched chain conformations, see sec. 3.5), one can write the nematic director as

$$\boldsymbol{n}(\boldsymbol{x}) = \overline{\boldsymbol{n}} + \delta\boldsymbol{n}(\boldsymbol{x}), \tag{3.9}$$

where $|\delta\boldsymbol{n}(\boldsymbol{x})|$ is small [82]. In such cases, the director fulfills $|\boldsymbol{n}(\boldsymbol{x})| \approx 1$, and the Fourier transformation of the distortion field can be written as $\delta\boldsymbol{n}(\boldsymbol{q}) = (\delta n_{\text{in}}(\boldsymbol{q}), \delta n_{\text{out}}(\boldsymbol{q}))$ (harmonic approximation). Thus, the Frank free energy (eq. 3.8) is approximated by

$$F_n \approx \frac{1}{2}\sum_{\boldsymbol{q}} \left(K_1 q_\perp^2 + K_3 q_\parallel^2\right) |\delta n_{\text{in}}(\boldsymbol{q})|^2 + \frac{1}{2}\sum_{\boldsymbol{q}} \left(K_2 q_\perp^2 + K_3 q_\parallel^2\right) |\delta n_{\text{out}}(\boldsymbol{q})|^2. \tag{3.10}$$

The components of the projected instantaneous director (see illustration in Fig. 3.3), $\delta n_{\text{in}}(\boldsymbol{q})$ and $\delta n_{\text{out}}(\boldsymbol{q})$, lie in the plane spanned by the average director $\overline{\boldsymbol{n}}$ and the scattering vector $\boldsymbol{q}$, and normal to this plane, respectively (see Fig. 3.3) [82, 100]. The scattering vector $\boldsymbol{q}$ is decomposed into components parallel, $q_\parallel$, and perpendicular, $q_\perp$, to the director $\overline{\boldsymbol{n}}$. The approximated free energy (eq. 3.10), even though yet not applicable to the case of polymeric sys-

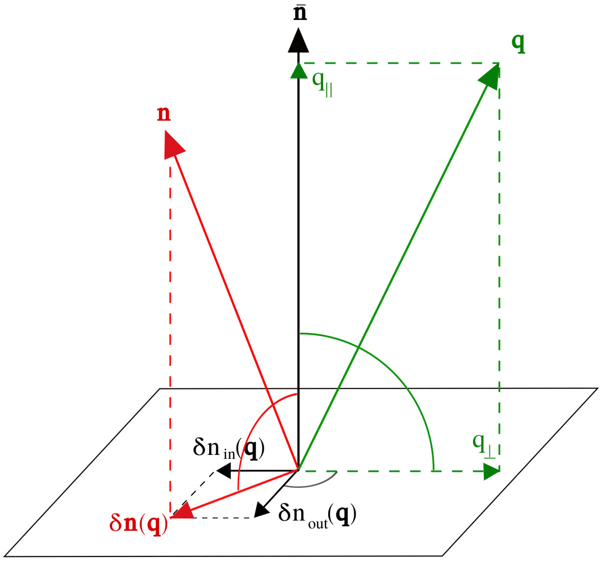

Figure 3.3: Scheme, illustrating the components $\delta n_{\text{in}}(\boldsymbol{q})$ and $\delta n_{\text{out}}(\boldsymbol{q})$ of the projection of the instantaneous nematic director, $\delta\boldsymbol{n}$, expressed as functions of the scattering vector $\boldsymbol{q}$. The component $\delta n_{\text{in}}(\boldsymbol{q})$ is defined in the plane spanned by the average director $\overline{\boldsymbol{n}}$ and $\boldsymbol{q}$. $\delta n_{\text{out}}(\boldsymbol{q})$, respectively, points along the corresponding plane normal. The scattering vector $\boldsymbol{q}$ and its components parallel ($q_{\|}$) and perpendicular ($q_{\perp}$) to the director $\overline{\boldsymbol{n}}$ are also shown.

tems, is a workhorse for experimental measurements of the Frank elastic constants. Using the equipartition theorem for the sum over degrees of freedom, eq. 3.10 relates the material constants with the fluctuation modes, i.e.

$$\begin{aligned} \langle|\delta n_{\text{in}}(\boldsymbol{q})|^2\rangle &= \frac{k_B T}{K_1 q_\perp^2 + K_3 q_\|^2}, \\ \langle|\delta n_{\text{out}}(\boldsymbol{q})|^2\rangle &= \frac{k_B T}{K_2 q_\perp^2 + K_3 q_\|^2}. \end{aligned} \tag{3.11}$$

The ensemble averages (eq. 3.11) are directly related to, for example, the scattering intensity obtained from light scattering experiments [118, 133, 134].

3.2 Motivation of studies

For liquid crystalline polymers, the elastic properties of the material are expected to be more complex than for a short mesogene LC, due to large spatial correlations along the molecular backbone and the interplay between mesoscopic order and molecular flexibility. It is known that for long molecules, the orientation and density fluctuations are coupled [101–103]. Splay deformations in the material therefore lead to fluctuations in density. This mechanism significantly alters the generic form of the fluctuation spectra, i.e. eqs. 3.11.

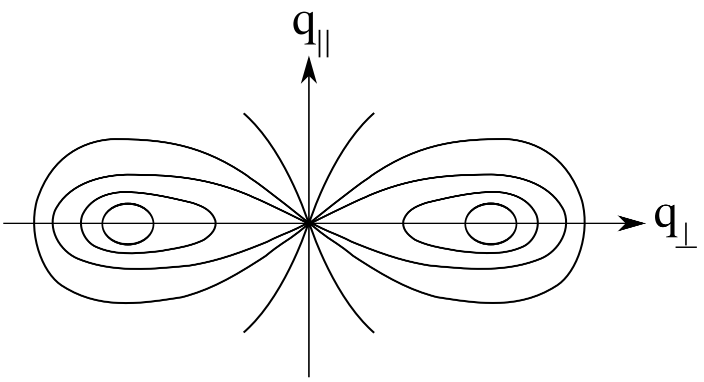

Figure 3.4: Scheme, illustrating the bowtie-shaped density scattering pattern in the $q_{||}$-$q_\perp$-plane by lines of constant magnitude. For long chains, scattering along the director, i.e. the direction of $q_{||}$, is suppressed. Along $q_\perp$, perpendicular to the director, a constant scattering is predicted for small $q_\perp$. This figure is adopted from Ref. [108].

Only a few experimental results have been reported on the behavior of the Frank constants for lyotropic [133–135] and thermotropic [97–99] LCP, which contrast a wealth of analytical work addressing the subject [101–108]. For example, a bowtie-shaped density-density scattering contour (see Fig. 3.4) has been predicted theoretically [104–108], which has been, at least for a moderately large wave length regime, confirmed experimentally [135]. However, for the dependence of the splay elastic constant on chain length the theoretical predictions differ, since one relies on the assumption of a generic mechanism creating the splay distortions [101–103].

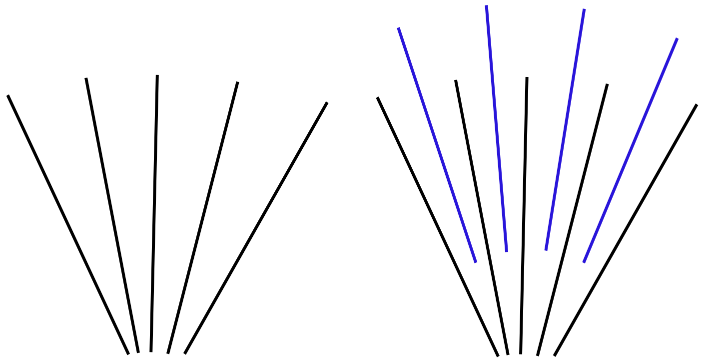

Figure 3.5: Scheme, illustrating the large voids created by a splay deformation of long molecules (compare left scheme). The energetic cost of creating a splay was derived by de Gennes [101, 102] from a simple estimation of the penalty from the large induced density variation. Mayer [103] pictured a mechanism of creating a splay by filling the voids with the chain ends of surrounding molecules.

Most prominently, the conclusions drawn from the work of de Gennes [101, 102] and Meyer [103] differ fundamentally, since they support, respectively, an either quadratic or linear dependence of the splay constant on chain length. Both predictions are derived under the assumption that the number of hairpin defects, i.e. sharp turns of chain backbones leading to backfolded conformations, is negligible in the considered systems.

The scheme in Fig. 3.5 illustrates in a simplified way the different mechanisms of creating a splay. If molecules are long, the splay deformation gives rise to a large density fluctuation along the chain contours, inducing voids in the material (see left scheme in Fig. 3.5). De Gennes estimated that the characteristic dependence on chain length stems solely from the penalty for density

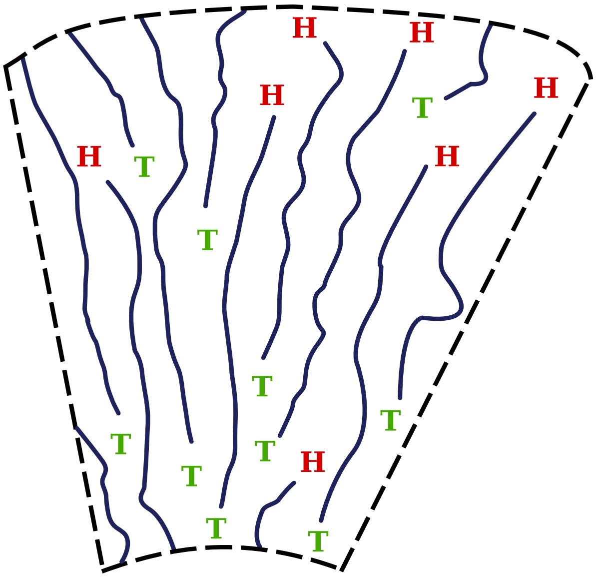

Figure 3.6: Scheme, illustrating the insertion of chain ends in a polymer nematic mesophase, creating thereby a splay deformation of the director field. Chains heads are labeled with H, and tails with T, respectively. According to Meyer [103], this is the dominant excitation mechanism creating a splay deformation in polymer nematic material. The assumption is based on chains which are reasonably stretched, i.e. the amount of hairpins is negligible. This figure is adopted from Ref. [103].

variations arising from a tilt of the molecular axis. From this assumption, he predicted a quadratic scaling with chain length [101, 102]. In contrast, Meyer proposed a mechanism to create a splay deformation with smaller density variations. The right scheme in Fig. 3.5 illustrates the chain end insertion mechanism in order to minimize the density fluctuations. In that way, a splay deformation is energetically less costly than in the scenario proposed by de Gennes. Meyer derived the linear scaling of the splay constant with chain length from an entropic penalty for the creation of an inhomogeneous spatial distribution of chain heads and tails [103] (see Fig. 3.6). It has been shown [136] that

the difference between both explanations vanishes for lyotropic LCP, since for such systems the compressibility is inversely proportional to the chain length. For thermotropic LC, i.e. a polymer melt, the difference remains.
For the twist and bend Frank elastic constants, independence of chain length has been predicted, provided the chains are reasonably flexible [103, 107, 116, 137, 138]. There are some more recent theoretical predictions on the behavior of the Frank constants which support the predictions by Meyer, presented in a series of publications from Nelson et al. [104–106, 108]. The main findings from the theory presented in these publications are reviewed in sec. 3.5, preparing for the comparison of simulation results with theoretical predictions.

An experimental test of the theoretical predictions regarding the fine details of the large wave length regime in the scattering contour [104–108] is difficult to realize with standard scattering techniques [133–135]. In simulations, small-angle scattering amplitudes are in principle accessible, however, one relies on the equilibration of very large configurations - which is computationally expensive with standard particle-based schemes. For polymer LC, long-range correlations due to relatively stiff backbones are present and the systems of interest have to be even larger, which pushes the conventional simulation techniques based on hard potentials, for example Lennard-Jones-based Molecular Dynamics simulations, to a limit.
Possibly for that reason, numerical studies on fluctuation spectra in LCP are rare to date. In simulations of small-molecule LC, single-site interaction-based models helped to improve the sampling, however they have yet only been applied with harsh repulsive interactions at close distances [109–111]. For LCP, elastic constants of lyotropic systems have been discussed with models based on connected, infinitesimally thin line segments in two-dimensional geometries [139], in order to remedy the limitation of system size. In one case, a simulation study on three-dimensional LCP, in which molecules were represented by connected hard spheres, indicated a bowtie pattern in the density

fluctuation spectra [140].

From this point of view, the use of soft, generic models [69] may help to overcome some of the discussed limitations. While retaining the explicit particle-based representation and hence the explicit information about the local nematic director, a significant overlap of segments due to soft non-bonded interactions can increase the sampling efficiency. Furthermore, the connection of the particle-based model to its field-based equivalent representation simplifies the tuning of the phase behavior of the system [69]. In this way, one may be able to study systems which are sufficiently large for investigating long wave length director fluctuations in nematic LCP. Novel simulation results supporting this statement will be presented in ch. 3.6, in which they are compared with existing predictions from analytical theories for nematic LCP (in the zero-hairpin limit).

3.3 Coarse-grained model for nematic polymers

The coarse-grained model builds on an approach presented earlier by Daoulas et al. [69]. There, a worm-like chain (WLC) model for the bonded degrees of freedom was used in combination with a grid-based scheme for evaluating non-bonded interactions, which are obtained from a functional of local density and nematic order parameters. In the following, the approach used in Ref. [69] for modeling non-bonded interactions will be developed further. The interactions will be derived analytically from the functional of order parameters. The scheme differs from the grid-based method in that it does not use a lattice collocation algorithm for the evaluation of non-bonded interactions, i.e. they are calculated in continuum. Details will be provided in the following. The definition and parameterization of bonded interactions equal those in Ref. [69] and they will only briefly be rephrased.

Without limiting the generic spirit of the molecular model, an approximate matching of parameters to experimental data has been performed. The length scale and stiffness of the polymer chain model, i.e. the bonded degrees of freedom, are roughly matched to experimental values for poly(3-hexylthiophene) (P3HT) [69]. P3HT is a theoretically and experimentally well studied example of a conjugated polymer used in the field of organic electronics [141]. It belongs to the family of polyalkylthiophenes, in which, for some representatives, a nematic liquid crystalline phase has been reported experimentally [142–149]. The specific matching was performed on the background of a broader modeling project, trying to describe the morphology of materials which are used in organic electronics applications with simple models. This will be the topic of the following chapters 4 and 5. For the main results in the present chapter, the chemical specificity is not relevant.

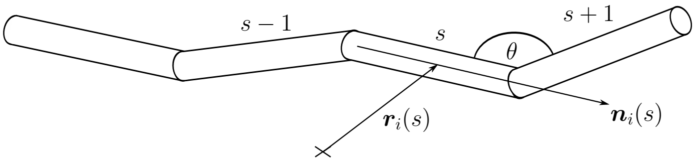

Figure 3.7: Schematic representation of the worm-like chain construction. The molecular axis $\boldsymbol{n}_i(s)$ in chain with index i is oriented along the segment s. Two consecutive vectors span the angle θ, entering the bonded potential.

3.3.1 Bonded interactions

The model system contains n discrete worm-like chains (WLC) (see Fig. 3.7) and has N coarse-grained segments associated with coordinates $\boldsymbol{r}_{\mathrm{i}}(s)$ and bond orientations indicated by $\boldsymbol{n}_{\mathrm{i}}(s)$. The index i counts the chains, while index s is counted along the chain contour to label individual segments. The Hamiltonian, with respect to the bonded degrees of freedom, reads [69]

$$\frac{H_{\mathrm{b}}}{k_B T} = -\frac{\epsilon}{b^2} \sum_{s=1}^{N-1} \boldsymbol{n}_{\mathrm{i}}(s+1) \cdot \boldsymbol{n}_{\mathrm{i}}(s). \tag{3.12}$$

Therein, the parameter ϵ controls the bending stiffness, penalizing the deviation of pairs of consecutive segments from parallel alignment, quantified by the angle

$$\Theta = \arccos\left(\frac{\boldsymbol{n}_{\mathrm{i}}(s+1)\boldsymbol{n}_{\mathrm{i}}(s)}{|\boldsymbol{n}_{\mathrm{i}}(s+1)||\boldsymbol{n}_{\mathrm{i}}(s)|}\right). \tag{3.13}$$

A fully stretched backbone conformation represents the energy minimum. The parameter $b = |\boldsymbol{n}_{\mathrm{i}}(s)|$ is the coarse-grained bond length.

For parameterizing the bonded interactions, the bond length can be taken as $b = 0.79\,\mathrm{nm}$, corresponding to a 2:1 mapping scheme of hexylthiophene units to coarse-grained segments [69]. The bond length is kept constant during the simulations, since the model operates on scales much larger than the typical magnitude of bond length fluctuations. Indirectly, the persistence length l_p of a model chain is matched via the stiffness parameter ϵ to the regime of experimentally reported values $l_\mathrm{p} \simeq 2.2 - 2.4\,\mathrm{nm}$ for P3HT conformations in solution [150, 151]. The conformations for chains in a melt, unless they are ordered, are expected to resemble those of the molecule in Θ-solvent conditions [19]. However, the experimental results from Ref. [151] were obtained in moderately good solvent conditions and therefore the model chains are considered less flexible than in the real system [69].

One can obtain analytically a value for the stiffness constant ϵ that corresponds to a certain persistence length. From the theory of the WLC model, defined by eq. 3.12, the relating equation [69, 152] reads

$$\frac{b}{l_\mathrm{p}} = \ln\left[\frac{1 - \exp(-2\epsilon)}{1 - \frac{1}{\epsilon} + (1 + \frac{1}{\epsilon})\exp(-2\epsilon)}\right]. \tag{3.14}$$

Solving eq. 3.14 numerically, $l_\mathrm{p} \simeq 2.2\,\mathrm{nm}$ leads to the choice of $\epsilon = 3.284$ [69].

3.3.2 Non-bonded interactions

The non-bonded potential will be derived from a functional of local order parameters, generically capturing the nematic liquid crystalline phase behavior (compare ch. 2.2). The ansatz is similar to field-theoretical approaches to polymeric liquid crystals [26, 121–124]. The functional is connected to a mesoscopic pairwise potential, which is subjected to a relatively coarse molecular description level, i.e. single-site interactions [69]. The non-bonded interactions are orientation dependent, coupling the molecular axes of a pair of segments explicitly. The potential is soft, i.e. the energy of fully overlapping segments remains on the order of magnitude of the thermal energy k_BT. Excluded volume constraints are thereby relaxed, increasing the sampling efficiency compared to modeling approaches for nematic polymers based on isotropic, hard repulsive interactions [140].[1]

Traditionally, for field-theoretic approaches based on an effective functional (Hamiltonian) of local order parameters, the functional is linked to contact potentials expressed through delta functions [26] (compare ch. 2.2.4). For transforming the Hamiltonian into a particle-based pairwise potential with finite interaction range, such interactions have to be regularized, i.e. the delta functions have to be smeared out in space (see ch. 2.2.4 for a more detailed discussion). In earlier studies, a collocation grid has been frequently used for transforming a functional of local densities into a pairwise potential, which can then be addressed with a standard Monte Carlo simulation scheme [29, 30, 85–87]. Such a collocation grid for evaluating non-bonded interactions has also been used in Ref. [69], applying similar concepts to anisotropic interactions.

In this thesis, a different route is taken, calculating non-bonded interactions directly from the continuum space representation of segments. Even though the evaluation of non-bonded interactions cannot be performed efficiently via a grid, i.e. without a costly neighbor searching algorithm, the explicit underlying connection to the functional is retained. Such schemes have been applied for isotropic potentials before [32–34, 93, 94].

The reason for choosing a grid-less simulation scheme is that for more complex molecular architecture (i.e., for the model developed in ch. 4), a registration of the average (macroscopic) director with the underlying grid was observed. The artifacts were observed for systems with different lattice spacing and remained present even for systems with a very fine grid spacing and more sophisticated collocation schemes. For example, for an assignment of particles to grid points within a spherical surrounding volume and a collocation of a single particle to several hundreds of grid points, artifacts remained.

---

[1] This is explained by the fact that isotropic repulsive interactions have to be sufficiently strong, in order to be able to observe an ordered phase [153].

Such grid artifacts have been found earlier in more complex geometries, e.g. for polymers close to adsorbing surfaces [91].
The local fluctuations of the nematic director, which are in the main focus of this chapter, may be especially sensitive to such a grid registration, additionally motivating the choice of an off-lattice evaluation scheme.

The top-down model for non-bonded interactions is based on the definition of a functional [26, 69, 75, 121–124],

$$\frac{H_{\text{nb}}\left[\hat{\rho}, \hat{\boldsymbol{Q}}\right]}{k_B T} = \rho_0 \left[\int d\boldsymbol{r}\, \frac{\kappa}{2} \left(\frac{\hat{\rho}(\boldsymbol{r})}{\rho_0} - 1 \right)^2 - \frac{v}{3} \int d\boldsymbol{r}\, \hat{\boldsymbol{Q}}(\boldsymbol{r}) : \hat{\boldsymbol{Q}}(\boldsymbol{r}) \right] . \quad (3.15)$$

In this expression, the local density field is introduced as

$$\hat{\rho}(\boldsymbol{r}) = \sum_{i,s} \delta(\boldsymbol{r} - \boldsymbol{r}_i(s)), \quad (3.16)$$

which can be seen as an operator assigning the segment coordinates $\boldsymbol{r}_i(s)$ to the density field $\hat{\rho}$. The parameters κ and ν control the density fluctuations and the orientation coupling strength, respectively [69]. An expression similar to $\hat{\rho}$ can be written for the local nematic order tensor field

$$\hat{Q}_{\alpha\beta}(\boldsymbol{r}) = \frac{1}{\rho_0} \sum_{i=1}^{n} \sum_{s=1}^{N} \delta\left(\boldsymbol{r} - \boldsymbol{r}_i(s)\right) q_{i,\alpha\beta}(s), \quad (3.17)$$

with

$$q_{i,\alpha\beta}(s) = \left[\frac{3}{2} n_{i,\alpha}(s) n_{i,\beta}(s) - \frac{\delta_{\alpha\beta}}{2} \right], \quad (3.18)$$

connecting the segment orientations $\boldsymbol{n}_i(s)$ with the field $\hat{\boldsymbol{Q}}(\boldsymbol{r})$ [26]. The double dot product used in eq. 3.15 is defined as a double summation over pairs of indices, i.e. $\boldsymbol{A} : \boldsymbol{B} := \sum_\alpha \sum_\beta A_{\alpha\beta} B_{\alpha\beta}$ for a pair of tensors $\boldsymbol{A}$ and $\boldsymbol{B}$. For symmetric tensors, the definition is equal to a contraction and subsequent

summation over tensor components.
Now, one can perform a step along the line of the example in ch. 2.2.4, substituting the local fields $\hat{\rho}(\boldsymbol{r})$ and $\hat{\boldsymbol{Q}}(\boldsymbol{r})$ in the functional eq. 3.15 with their averaged equivalents [32–34, 93, 94], $\hat{\Phi}_\omega(\boldsymbol{r})$ (eq. 2.32 from ch. 2.2.1) and

$$\hat{\boldsymbol{Q}}_\omega(\boldsymbol{r}) = \int d\boldsymbol{r}'\omega(|\boldsymbol{r} - \boldsymbol{r}'|)\hat{\boldsymbol{Q}}(\boldsymbol{r}'). \tag{3.19}$$

Similar to the transformation of the density dependent part of eq. 3.15, which has been presented in ch. 2.2.1, it is possible to do a transformation of the part in eq. 3.15 which involves the orientation tensor. The details about the transformation is given in appendix ch. 1 for the more general case of a functional involving an additional orientation tensor which quantifies biaxial order (this case will be covered in ch. 4). This leads to an expression for the non-bonded interactions in terms of a pairwise potential,

$$V_{\text{nb}} = u(r_{ij}(s,m)) \left[\bar{\kappa} - \frac{2\bar{\nu}}{3} \boldsymbol{q}_i(s) : \boldsymbol{q}_j(m) \right], \tag{3.20}$$

in which $r_{ij}(s,m) = |\boldsymbol{r}_i(s) - \boldsymbol{r}_j(m)|$ and the tensors $q_{i,\alpha\beta}(s)$, defined in eq. 3.18, express the segment orientations with respect to the laboratory coordinate frame. The constants $\bar{\kappa}$ and $\bar{\nu}$ are related to κ and ν in eq. 3.15 through the Boltzmann-factor, i.e. for example $\bar{\kappa} = \kappa k_B T$. The function $u(r)$ arises from an integration step performed when casting eq. 3.15 with the substitution of eq. 2.32 and eq. 3.19 into the expression eq. 3.20 (compare Refs. [32–34, 93, 94]). However, the analytical form of $u(r)$ remains dependent on the explicit choice of the weight function ω (compare Refs. [32–34, 93, 94] and appendix ch. 1).

One can show the equivalence of the orientation coupling term in eq. 3.20, written as the double dot product of the molecular tensors, and the familiar expression of the latter quantity through the second Legendre polynomial, i.e. proportional to the Maier-Saupe coupling eq. 3.1 with the angle θ spanned by

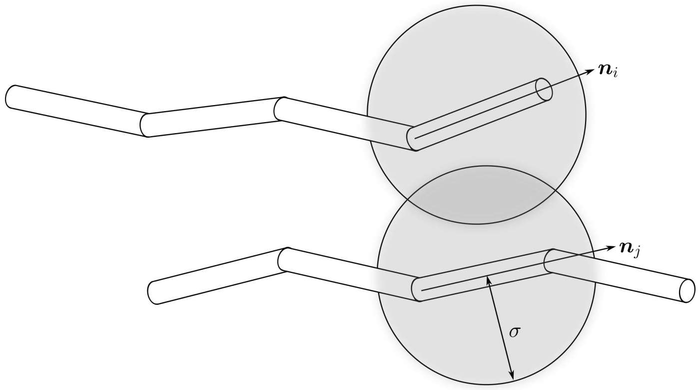

Figure 3.8: Schematic representation of the non-bonded interaction between pairs of segments. The molecular axes $\boldsymbol{n}_i$ and $\boldsymbol{n}_j$ enter the potential in eq. 3.20 through the molecular nematic tensors. The distance dependent contribution to the potential, i.e. the function $u(r)$, is illustrated as the overlap of density clouds with radius σ surrounding each segment.

a pair of segments evaluated similar to eq. 3.13.

Factorizing non-bonded interactions into distance and orientation dependent parts (compare eq. 3.20) has been frequently reported in other studies of LC with soft models [110, 126–128, 154]. In this thesis, the distance dependent soft core $u(r_{ij}(s,m))$ is chosen proportional to the geometric overlap of two spherical density distributions, compare Fig. 3.8. The weight function is set to

$$\omega(\boldsymbol{r}) = \frac{3}{4\pi\sigma^3} \tag{3.21}$$

for $r \leq \sigma$ and zero otherwise. The density clouds are placed at the segment centers (compare Fig. 3.8), i.e. at $\boldsymbol{r}_i(s)$ and $\boldsymbol{r}_j(m)$, respectively.
The explicit form of the core $u(r_{ij}(s,m))$ can be obtained by solving an overlap integral analytically. More details about this calculation can be found in the appendix ch. 1. Here, only the result is given, reading [34]

$$
\begin{aligned}
u(r_{ij}(s,m)) &= \frac{1}{\rho_o}\int d\boldsymbol{r}\,\omega(\boldsymbol{r}-\boldsymbol{r}_i(s))\omega(\boldsymbol{r}-\boldsymbol{r}_j(m)) = \\
&= \frac{3}{8\pi\rho_o\sigma^3}\left(2+\frac{r_{ij}(s,m)}{2\sigma}\right)\left(1-\frac{r_{ij}(s,m)}{2\sigma}\right)^2 .
\end{aligned}
\tag{3.22}
$$

In order to draw an approximate connection between the model and a real system of P3HT chains, a density cloud can be interpreted as the continuous, coarse-grained representation of underlying microscopic degrees of freedom [69, 155, 156]. The radius, $\sigma = 0.79\,\mathrm{nm}$, is chosen according to the length of a hexyl chain in all-*trans* configuration. Below this distance, neighboring chains start overlapping. Taking into account that the bulk density of P3HT is $\sim 4\,\mathrm{hexylthiophenes/nm^3}$, and each coarse-grained segment represents two real monomers, the reference density is chosen $\rho_0 = 2\,\mathrm{segments/nm^3}$ (compare ch. 4).

Following the discussion in Ref. [69] for the model parameterization, the free parameters of the non-bonded interactions, $\bar{\kappa}$ and $\bar{\nu}$, are chosen from a mean-field estimate of the free energy for a homogeneous system from eq. 3.15. From the Maier-Saupe phenomenological mean-field theory [120] it is known that for non-flexible molecules an isotropic-nematic transition occurs above a coupling strength $\nu_{\mathrm{MS}} \simeq 4.54$. This value can be kept as an upper limit, since ordering is expected at weaker coupling strength for flexible molecules, i.e. in the case of polymers [157]. To obtain nematic ordering, the strength of orientation coupling is empirically chosen as $\bar{\nu} = 3.33k_BT$ [69]. From a mean-field estimation of the free energy evaluated for perfect nematic order (i.e., $S = 1$), a lower limit for the compressibility-related parameter $\bar{\kappa}$ can be derived, in a way that the (estimated) compressibility remains non-negative. Details about the mean-field estimation of the free energy and the isothermal compressibility can be found in the appendix ch. 2 and in Ref. [69]. For the studies discussed in this thesis, the value $\bar{\kappa} = 7.58k_BT$ is chosen somewhat higher compared to Ref. [69], in order to ensure a positive compressibility in the case of strong nematic coupling. All simulations have been performed at the temperature $T = 500\,\mathrm{K}$.

3.4 Systems studied and simulation details

Monodisperse melts of polymer chains with $N = 16$, 32, 48 and 64 segments, which corresponds to ~ 20 persistence lengths for $N = 64$, have been equilibrated using Monte Carlo (MC) simulations in the nVT ensemble. Cubic simulation cells with periodic boundary conditions in all directions are considered. For the three largest chain lengths N, the length of the cell-edges L_{box} is chosen to be two times larger than the end-to-end distance of a fully stretched WLC (which equals the contour length $L = bN$). For the shortest chain length, $N = 16$, the dimensions of the cell are larger, $L_{\mathrm{box}} = 4L$. The number of molecules in a system is chosen in a way that the average segment density reproduces the reference bulk density of P3HT $\rho_0 = 2\,\mathrm{segments/nm}^3$, i.e., $nN/V = \rho_0$. For the longest chains with $N = 64$ segments this leads to systems with up to 2×10^6 segments. Due to the softness of the nonbonded interactions it has still been possible to equilibrate the samples with a serial calculation on a single CPU. For testing the relaxation, the saturation of macroscopic observables, e.g. the nematic order parameter and the average end-to-end distance of a chain, has been monitored during the simulations in order to reach a plateau. For additional control of sampling errors due to finite trajectories, for each of the considered chain lengths, eight independent simulations have been performed. This allows a systematic error estimation of the extracted properties (compare sec. 3.6).

All chains are initially fully stretched and aligned along the z-axis of the laboratory frame, while their centers-of-masses are randomly distributed. The systems have been relaxed with a Monte Carlo algorithm which uses non-local

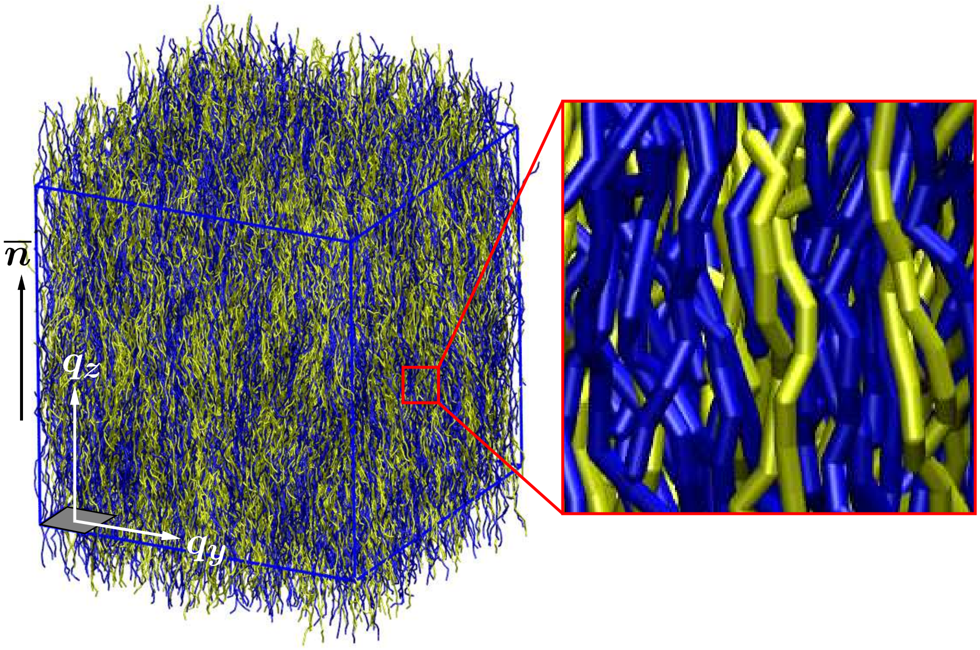

Figure 3.9: Visualization of a representative configuration of a nematic WLC melt with $N = 32$ segments per chain. The chains are aligned along the z-axis, and $\overline{\mathbf{n}}$ denotes the macroscopic director of the phase. The edge length of the simulation cell is $L_{\text{box}} = 2L$ (with the contour length L of the WLC). To demonstrate that L_{box} is substantially larger than the actual end-to-end distance of the chains along the director of the nematic phase, the configurations are presented without breaking individual chains at the periodic boundaries of the simulation box, i.e. with a wrapping based on the centers-of-masses of the chains. The vectors $\boldsymbol{q}_y$ and $\boldsymbol{q}_z$ mark the yz-plane used for the calculations of the density and director fluctuation spectra. The two-color scheme of the visualization is used for improving the visibility of chain contours. All chains are however identical in terms of chain length and interactions.

backward and forward reptation, with either of the two possible directions chosen with equal probability. Reptation moves [158, 159] are mixed with local flip moves, in which a coarse-grained bead is rotated by a random angle around the axis defined by the corresponding bond vectors. With a 70% probability, a trial move is a reptation, while 30% of the trials are local flip moves. Each attempted move is accepted using the standard Metropolis acceptance probability [160]

$$p_{\text{acc}} = \min\left(1, \exp\left(-(\Delta H_{\text{b}} + \Delta H_{\text{nb}})/k_B T\right)\right), \tag{3.23}$$

with the energy changes ΔH_{b} and ΔH_{nb} concerning the bonded and non-bonded interactions of the system after having performed the trial step. For the combination of reptation and local flip moves, an acceptance rate of $\sim 22\%$ is observed in the ordered phase. Periodic boundaries have been used in all three directions and a standard (i.e., non-linked) cell list has been used for the evaluation of non-bonded interactions. A representative snapshot of an equilibrated nematic melt of chains with $N = 32$ is presented in Fig. 3.9.

3.5 Theory revisited

A few theoretical predictions regarding density and director fluctuations in nematic liquid crystalline polymers (LCP) are now recapitulated, applied to the discrete worm-like chain model which has been used in the simulations. It should already be noted that the theory which is reviewed was formulated for a system with no hairpins, i.e. fully stretched chains [104, 105, 107, 108]. In simulations, as it will be shown in ch. 3.6.2, the molecules have not been constrained, i.e. the configurations do not correspond to the zero-hairpin limit. For a nematic LCP mesophase with n continuum WLC's, it is straightforward to introduce a local areal density of chains intersecting a plane normal to the average director of the mesophase, $\overline{\mathbf{n}}$.

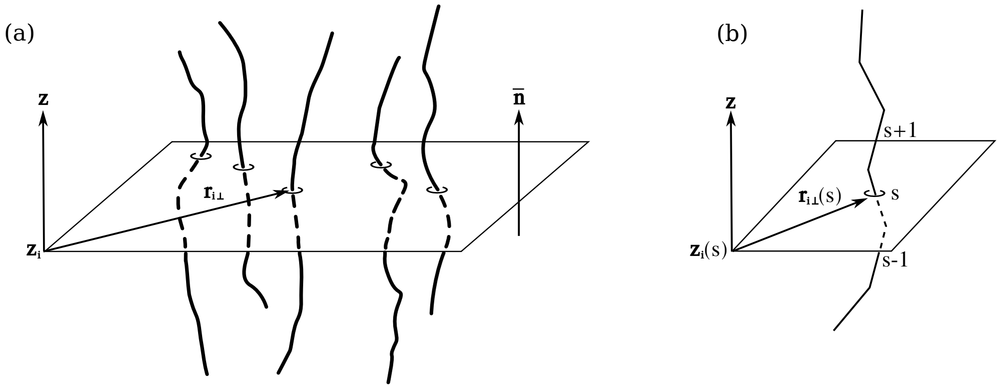

Figure 3.10: (a) Illustration of the labeling of a position along the contour of a WLC chain with index i with respect to a coordinate along the director $\overline{\boldsymbol{n}}$ and a vector $\boldsymbol{r}_{i\perp}$ in the plane perpendicular to $\overline{\boldsymbol{n}}$. (b) Labeling of the segment position for the discrete WLC chains, expressed in terms of the discrete parameter s counting along the chain segments.

Without loosing generality, it is convenient to assume that $\overline{\mathbf{n}}$ is parallel to the z-axis of the laboratory coordinate frame (see Fig. 3.10a). In this case, z_{p} sets the position of such a plane and $\boldsymbol{r}_{\perp}$ is a two dimensional vector defining a point on the plane. In this setup, chains which are oriented without backfolding can be described [104, 105, 107, 108] as curves which are single-valued functions of z. The local areal density becomes

$$\rho(\boldsymbol{r}_\perp, z_\mathrm{p}) = \sum_{i=1}^{n} \int_{z_0(i)}^{z_\mathrm{L}(i)} \delta\left(\boldsymbol{r}_\perp - \boldsymbol{r}_{i\perp}(z)\right) \delta\left(z_\mathrm{p} - z\right) dz. \tag{3.24}$$

In eq. 3.24, $z_0(i)$ and $z_\mathrm{L}(i)$ are projections of the two ends of the i-th chain on the z-axis (L is the contour length of the WLC). Within a hydrodynamic treatment of correlations, local fluctuations $\delta\rho(\boldsymbol{r}_\perp, z_\mathrm{p})$ and $\delta\boldsymbol{n}(\boldsymbol{r}_\perp, z_\mathrm{p})$ of density and director fields can be penalized through a free energy [104, 105, 108],

$$F = \int d\boldsymbol{r}_\perp \int dz_\mathrm{p} \left[\frac{B}{2} \left(\frac{\delta\rho}{\tilde{\rho}_0} \right)^2 + \frac{G}{2} \Big(\partial_{z_\mathrm{p}} \delta\rho + \tilde{\rho}_0 \nabla_\perp \delta\boldsymbol{n} \Big)^2 \right] + F_\mathrm{n}[\delta\boldsymbol{n}]. \tag{3.25}$$

The first term in eq. 3.25 represents a simple equation-of-state, with $\tilde{\rho}_0$ and B being the average areal chain density and two-dimensional bulk modulus, respectively. The latter does not depend on chain length, up to a $\mathcal{O}(L^{-1})$ term [105] due to translational entropy. For a chain to intersect a plane, the average distance of its center from z_p must be smaller than $l/2$ below or above the surface [161], with l being the average length or extension of the chain when projecting its contour on the z axis. Thus, it follows that $\tilde{\rho}_0 = nl/V$. The second term in eq. 3.25 expresses the constraint that changes in areal density and director fields are coupled. In particular [25, 103],

$$\partial_{z_\mathrm{p}} \delta\rho + \tilde{\rho}_0 \nabla_\perp \delta\boldsymbol{n} = \rho_\mathrm{H} - \rho_\mathrm{T}, \tag{3.26}$$

where ρ_H and ρ_T are the local densities of chain "head" and "tail" ends (compare illustration Fig. 3.6). In the limit of infinitely long chains, no chain ends are present and the differential form in eq. 3.25 is strictly zero. Hence, in this case $G \to \infty$. For finite chains to penalize deviations of $\rho_\mathrm{H} - \rho_\mathrm{T}$ from zero (as happens in the case of splay deformation [103]), analytical theories

[103–105, 108] typically assume

$$G = l k_{\mathrm{B}} T / 2\tilde{\rho}_0. \tag{3.27}$$

This corresponds to the concentration susceptibility of a mixture of "head" and "tail" ends, considering them as noninteracting ideal gases. Recently, it was recognized that this constraint in fact applies to polar nematic ordering and care is needed when applying the constraint in eq. 3.26 to nonpolar nematics (i.e., quadrupolar ordering) [161, 162]. For the latter, an alternative tensorial conservation law has been developed [162]. However, this constraint has not yet been incorporated into a theory describing fluctuations. F_{n} in eq. 3.25 is the "bare" Frank free energy eq. 3.8, with splay, K_1, twist, K_2, and bend, K_3, elastic constants which are approximately equal to those of a system of unpolymerized mesogenes [105].

From eq. 3.25, correlation functions of the local areal density and the director orientation were obtained [104, 105, 108] in the hydrodynamic limit and found in agreement with a more elaborated "microscopic" description, mapping polymer trajectories on wordlines of two-dimensional bosons in order to use the respective mathematical framework [104, 105, 108]. For the large wave length predictions of the theory, to which the simulation results will be compared, the subtle microscopic derivation of the theory is irrelevant.

To cast the results into the context of discrete WLC's, it is helpful to parameterize the continuum WLC through the arc length t of the curve. Since there is no backfolding, z will be a single-valued function of t, that is $z = z_i(t)$ and $\boldsymbol{r}_{i\perp}(z_i(t)) = \boldsymbol{r}_{i\perp}(t)$. Thus, eq. 3.24 becomes

$$\rho(\boldsymbol{r}_\perp, z_{\mathrm{p}}) = \sum_{i=1}^{n} \int_0^L \delta\left(\boldsymbol{r}_\perp - \boldsymbol{r}_{i\perp}(t)\right) \delta\left(z_{\mathrm{p}} - z_i(t)\right) z_i' dt. \tag{3.28}$$

Considering that $z_i' = dz_i/dt$ is the direction cosine of the tangent vector of the curve at value t of the arc length with the z-axis, a discrete analog of eq. 3.28 can be introduced as (compare Fig. 3.10)

$$\rho(\boldsymbol{r}_\perp, z_\mathrm{p}) = \sum_{i=1}^{n}\sum_{s=1}^{N} \delta\left(\boldsymbol{r}_\perp - \boldsymbol{r}_{i\perp}(s)\right)\delta\left(z_\mathrm{p} - z_i(s)\right) a, \tag{3.29}$$

with $\boldsymbol{r}_i(s) = \{\boldsymbol{r}_{i\perp}(s), z_i(s)\}$ being the coordinates of the centers of the segments of the discrete WLC and a a characteristic microscopic length scale representing an average projection of the distance between segment centers on the z-axis. Based on eq. 3.29 a structure factor for the density fluctuations can be defined as

$$\begin{aligned} &\langle \rho(\boldsymbol{q}_\perp, q_z)\rho(-\boldsymbol{q}_\perp, -q_z)\rangle = \qquad\qquad\qquad\qquad\qquad (3.30)\\ &\frac{a^2}{V}\left\langle \Big| \sum_{i,s=1}^{n,N} \exp\left[i\big(\boldsymbol{q}_\perp \cdot \boldsymbol{r}_{i\perp}(s) + q_z z_i(s)\big)\right] \Big|^2 \right\rangle = \left(\frac{\tilde{\rho}_0}{\rho_0}\right)^2 S(\boldsymbol{q}_\perp, q_z). \end{aligned}$$

Angular brackets denote an average in the canonical ensemble and $l = aN$ was substituted into $\tilde{\rho}_0 = nl/V$ to obtain $a = \tilde{\rho}_0/\rho_0$. The scattering function $S(\boldsymbol{q}_\perp, q_z)$ is normalized by V and not the number of scatterers nN, which is a more common choice. Direct substitution of theoretical results [104, 105, 108] for $\langle \rho(\boldsymbol{q}_\perp, q_z)\rho(-\boldsymbol{q}_\perp, -q_z)\rangle$ into eq. 3.30 leads to the following prediction for the discrete WLC model:

$$S(\boldsymbol{q}_\perp, q_z) = \frac{k_\mathrm{B} T \rho_0^2 \left(q_\perp^2 + \left(K_1 q_\perp^2 + K_3 q_z^2\right)/G\tilde{\rho}_0^2\right)}{B q_\perp^2 + \left(B/G\tilde{\rho}_0^2 + q_z^2\right)\left(K_1 q_\perp^2 + K_3 q_z^2\right)}. \tag{3.31}$$

The generic form of eq. 3.31 corresponds to a highly asymmetric scattering, in which the contour lines of constant $S(\boldsymbol{q}_\perp, q_z)$ create the characteristic bowtie pattern [104, 105, 107, 108, 135]. As an illustration, it is helpful to consider the limiting behavior of $S(\boldsymbol{q}_\perp, q_z)$ along the $q_z = 0$ and $q_\perp = 0$ axes:

$$S(q_\perp, 0) = \frac{k_\mathrm{B}T\rho_0^2}{B}, \qquad S(0, q_z) = \frac{k_\mathrm{B}T\rho_0^2}{B + G\tilde{\rho}_0^2 q_z^2}. \tag{3.32}$$

$S(0, q_z)$ has an Ornstein-Zernike form, with

$$\xi^2 = \frac{G\tilde{\rho}_0^2}{B} \tag{3.33}$$

being the analog of a (squared) correlation length. Indeed, the eqs. 3.32 demonstrate that for infinitely long chains, $l \to \infty$ (that is $G \to \infty$), no scattering along $q_\perp = 0$ should be observed, while constant scattering is still obtained for $q_z = 0$ [107, 135]. According to eq. 3.32, chains of finite length scatter also for $q_\perp = 0$. This scattering however decays as one moves from the origin of the axes. A more detailed discussion of the theoretically predicted contour plots of the structure factor can be found in Ref. [108]. Very few experimental investigations confirmed the bowtie-shaped scattering contour for real liquid crystalline polymers, from nematic samples of poly-γ-benzyl glutamate [135] in one case, and from aqueous suspensions of vanadium pentoxide [163] in another case. In both studies, small-angle X-ray scattering was used.

To compare the theoretical predictions with simulations, it is convenient to address director fluctuations in melts of discrete WLC's in terms of the nematic tensor [111, 115, 164, 165], $Q_{\alpha\beta}(\boldsymbol{r}) = \rho_0^{-1} \sum_{i,s}^{n,N} q_{i,\alpha\beta}(s)\delta(\boldsymbol{r} - \boldsymbol{r}_i(s))$, which is also given in eq. 3.3. The Fourier transformation of this quantity reads

$$Q_{\alpha\beta}(\boldsymbol{q}_\perp, q_z) = \frac{1}{\sqrt{V}\rho_0} \sum_{i,s=1}^{n,N} q_{i,\alpha\beta}(s) \exp\left[i\big(\boldsymbol{q}_\perp \cdot \boldsymbol{r}_{i\perp}(s) + q_z z_i(s)\big)\right]. \tag{3.34}$$

For $\overline{\mathbf{n}}$ oriented along the z-axis and small distortions of the director field, one has [115]

$$\delta n_\alpha(\boldsymbol{r}) = 2Q_{\alpha z}(\boldsymbol{r})/3\langle S\rangle, \tag{3.35}$$

with $\alpha = x, y$ and the average nematic order parameter $\langle S \rangle$. Thus, the theoretical predictions [104, 105, 108] for $\langle \delta n_\alpha(\boldsymbol{q}_\perp, q_z)^2 \rangle$ transform to:

$$\frac{4\langle |Q_{\alpha z}(\boldsymbol{q}_\perp, q_z)|^2 \rangle}{9\langle S \rangle^2 k_\mathrm{B} T} = \frac{1}{K_2 q_\perp^2 + K_3 q_z^2}\left(1 - \frac{q_\alpha^2}{q_\perp^2}\right) + \frac{1}{K_1^R q_\perp^2 + K_3 q_z^2}\left(\frac{q_\alpha^2}{q_\perp^2}\right) \quad \text{with} \quad K_1^R = K_1 + \frac{B}{\frac{B}{G\tilde{\rho}_0^2} + q_z^2}. \tag{3.36}$$

As in the case of $S(\boldsymbol{q}_\perp, q_z)$, angular brackets denote an average in the canonical ensemble.

The generic form of the spectrum of the orientation tensor in eq. 3.36 is typical [115] for nematic LC described by a Frank free energy (see eq. 3.11 for comparison), albeit, here the splay constant K_1^R is q-dependent. The limit of K_1^R for $q_z^2 \to 0$ is

$$K_{1(0)}^R = K_1 + B\xi^2 = K_1 + \frac{1}{2} k_\mathrm{B} T l \tilde{\rho}_0. \tag{3.37}$$

It can be seen that $K_{1(0)}^R \sim N$ (since $l = aN$) [104, 105, 108], in agreement with a more qualitative treatment by Meyer [103]. On the contrary, in the same limit, an alternative approach by de Gennes [101, 102] leads to a different scaling, $K_{1(0)}^R \sim N^2$. Notably, for infinite chains, all analytical theories [101, 104, 105, 108] are consistent with each other, predicting $K_1^R = K_1 + B/q_z^2$.

3.6 Results

3.6.1 Strength of nematic order and director orientation

To simplify the discussion of theoretical predictions in the previous section, it was assumed that the coordinate frame which is fixed to the laboratory (i.e., the simulation box) and the frame which is oriented with the z-axis along the macroscopic nematic director match. In simulations, this is true only for the initial starting configurations, with $\overline{\mathbf{n}}$ oriented along the z-axis of the simulation box. However, it is important to monitor $\overline{\mathbf{n}}$ during the entire Monte Carlo simulation since it can reorient [111, 166] due to fluctuations. Thus, in each melt configuration, the maximum eigenvalue, S, and the corresponding eigenvector of the tensor

$$\frac{1}{V}\int Q_{\alpha\beta}(\boldsymbol{r})d\boldsymbol{r} = \frac{1}{nN}\sum_{i,s}^{n,N} q_{i,\alpha\beta}(s) \tag{3.38}$$

were calculated. Table 3.1 summarizes the values of configurational averages of the maximum eigenvalues, $\langle S\rangle$, as a function of the chain length N.

N	16	32	48	64
$\langle S\rangle$	0.62(4)	0.65(1)	0.66(0)	0.66(7)

Table 3.1: Average nematic order parameter, $\langle S\rangle$, as a function of the number of chain segments, N.

From Table 3.1 it follows that the strength of nematic orientation increases with chain length, saturating for longer molecules. This behavior stems from orientational correlations along the chain backbone induced by bending rigidity [69] and is qualitatively similar to the shift of the isotropic-nematic transition to higher temperatures as molecular weight increases [69, 148, 157].

The eigenvector analysis demonstrates that for the two shortest melts, $N = 16$ and 32, the changes in the orientation of $\overline{\mathbf{n}}$ are indeed substantial. For example, for the $N = 16$ melt angles as large as $\theta = 7.5^{\circ}$ between $\overline{\mathbf{n}}$ and the $z-$axis of the laboratory frame were observed. At the same time, for the two longest melts $N = 48$ and 64 the reorientations of $\overline{\mathbf{n}}$ were found insignificant, i.e., the observed angles were at most $\theta \simeq 1^{\circ}$. The differences between the laboratory and the nematic director frames are taken into account [111, 166] during the analysis of the fluctuation spectra, as will be described in the relevant sections.

3.6.2 Chain stiffness and backfolding

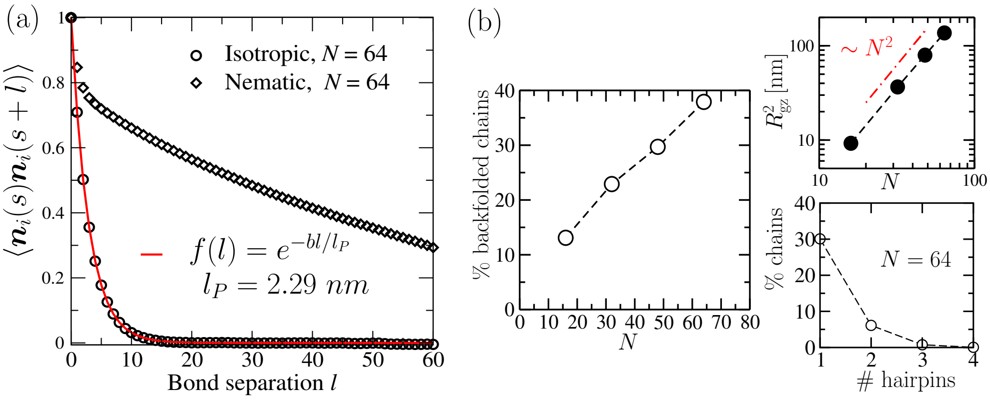

Figure 3.11: (a) Bond correlation data which is used for extracting the persistence of the bulk phase of WLC with $N = 64$ segments per chain. The fitted exponential is shown, and for comparison also the bond correlation function for chains in the ordered nematic phase. (b) Main panel: Percentage of chains in a melt having at least one hairpin, as a function of the number of chain segments, N. Lower right: Fraction of backfolded chains, as a function of the number of hairpins per chain for $N = 64$ melts. Upper right: The component of the average radius of gyration (squared), R^2_{gz}, along the director as a function of N.

Fig. 3.11a shows the decay of the bond orientation correlation measured in the amorphous and in the nematic bulk phase of chains with $N = 64$ segments. The measured persistence length $l_{\mathrm{p}} = 2.29\,\mathrm{nm}$ for the amorphous system agrees well with the initial input value, see ch. 3.3. For comparison, the same bond order correlation is shown for a nematic liquid crystalline phase, in which chains are aligned along a preferred direction. Orientational correlations of bond vectors decay significantly slower along the chain contour.

For the following discussion of fluctuation spectra and material constants, it is important to quantify the amount of backfolded chains as a function of polymer length. To comply with the theoretical description in Sec. 3.5, in every configuration, for each chain the number of intersections with a sequence of planes normal to the axis of the director, $\overline{\mathbf{n}}$, was calculated. The distance between the planes was chosen significantly smaller than the bond length. A chain was considered as backfolded if found to intersect a plane more than once.

Fig. 3.11b presents in the main panel the percentage of backfolded chains (averaged over all configurations) as a function of the number of segments in the chain. In can be seen that the amount of these molecules increases substantially with chain length so that for $N = 64$ almost 40% of polymers have at least one backfolding. The apparent linearity of the plot is due to the still moderate chain lengths. Even for the longest considered chains with $N = 64$, the fraction of chains with more than one hairpin is below 10%, which is illustrated in Fig. 3.11b in the lower right panel. Theoretical arguments based on the continuum WLC model [167] within mean-field approximation predict that the fraction of backfolded chains should eventually saturate to unity as $1 - \exp(-\Gamma)$ with

$$\Gamma = (L/l_0)\exp(-U_\mathrm{h}/k_BT). \tag{3.39}$$

The characteristic scales of length, l_0, and energy, U_h, are functions of the chain stiffness, strength of orientational coupling, order parameter, and temperature. L is the contour length. The small number of backfolding events per chain in the simulations is demonstrated in the upper right panel of Fig. 3.11b. The figure presents a logarithmic plot of the component of the average radius of gyration (squared) along the nematic director, R^2_{gz}, as a function of N. It can be seen that it still obeys a rod-like scaling $R^2_{\mathrm{gz}} \sim N^2$. In a regime with many hairpins it should be [116, 167] $R^2_{\mathrm{gz}} \sim N$.

3.6.3 Density fluctuation spectra

To calculate fluctuation spectra in simulations, the scattering vectors must comply with periodic boundary conditions [168] and it is more convenient to introduce them in the laboratory frame. There, the components of the $\boldsymbol{q}$-vector are given by

$$q^{\mathrm{L}}_{\alpha} = 2\pi i_{\alpha}/L_{\mathrm{box}}, \tag{3.40}$$

with i_{α} being integers and $\alpha = x, y, z$. For each configuration of the $N = 16$ and 32 melts, a density structure factor $S(\boldsymbol{q}^{\mathrm{L}})$ is calculated in the Fourier space of the laboratory frame via the definition in eq. 3.30 but replacing $\boldsymbol{q} = \{\boldsymbol{q}_{\perp}, q_z\}$ with $\boldsymbol{q}^{\mathrm{L}}$. The coordinates $\boldsymbol{r}_i(s)$ are by default given in the laboratory frame. To define the vectors, $-15 \leq i_{\alpha} \leq 15$ are used. Subsequently, a $\boldsymbol{q}^{\mathrm{L}}$-dependent 123-frame is introduced [111, 166] (123 is an arbitrary label for the coordinate frame which is rotating in the laboratory frame). The z-axis of this frame, in every configuration, is set along the corresponding $\overline{\mathbf{n}}$. The y-axis is placed in the plane defined by $\boldsymbol{q}^{\mathrm{L}}$ and $\overline{\mathbf{n}}$, while the x-axis is pointing in perpendicular direction. The scattering vector in the 123-frame is obtained as $\boldsymbol{q} = \hat{\boldsymbol{T}}\boldsymbol{q}^{\mathrm{L}}$, where $\hat{\boldsymbol{T}}$ is the rotation matrix transforming between the two frames. The components of $\hat{\boldsymbol{T}}$ are obtained, for each configuration, from the eigenvectors of the averaged nematic tensor eq. 3.38. From the definition of the 123-frame it follows that $\boldsymbol{q} = \{0, q_y, q_z\}$, with $\boldsymbol{q}_y \perp \overline{\mathbf{n}}$ and $\boldsymbol{q}_z \parallel \overline{\mathbf{n}}$. Transforming all available $\boldsymbol{q}^{\mathrm{L}}$ into $\{q_y, q_z\}$-pairs, the values of $S(\boldsymbol{q}^{\mathrm{L}})$ can be assigned to a two dimensional spectrum $S(q_y, q_z)$ in the director-based frame. Since θ changes during

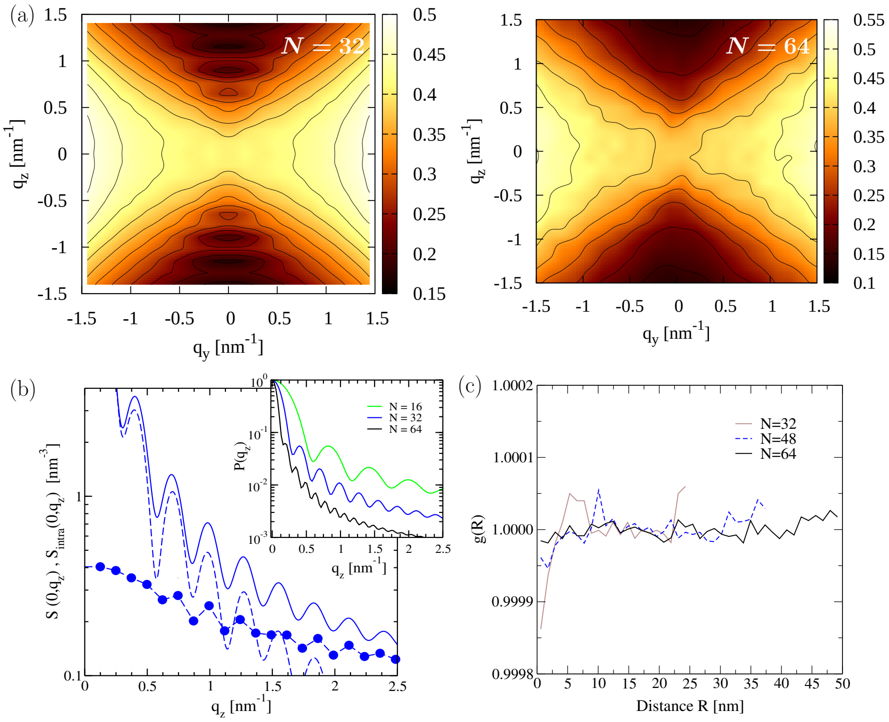

Figure 3.12: (a) Contour plot of the density fluctuation spectrum, $S(q_y, q_z)$, in the nematic director frame of a melt with $N = 32$ (left figure) and $N = 64$ (right figure) segments per chain. Contour lines correspond to equal magnitudes of scattering. (b) Main panel: Solid circles show a one-dimensional "cut" of the scattering function $S(0, q_z)$ for the $N = 32$ melt. The contribution from intramolecular scattering along the z-axis, $S_0(0, q_z)$, is shown with a solid line. An estimate of $S_0(0, q_z)$ based on a rod system is shown with a dashed line (see main text for details). Inset: Form factor, $P(0, q_z)$, for $N = 16$, 32 and 64 melts. (c) One-dimensional pair correlation of chain ends projected onto the z-axis, for systems with $N = 32$, 48 and 64.

the run, the discrete set of vectors $\boldsymbol{q}^{\mathrm{L}}$ generates a set of continuous $\boldsymbol{q}$-vectors in 123-frames. In practical applications, the continuum values of q_y and q_z

are coarse-grained into regularly spaced bins [111]. In this thesis, the width of the bins is chosen equal to the resolution $2\pi/L_{\text{box}}$ of the Fourier space in the laboratory frame and final spectra are obtained as averages of the $S(q_y, q_z)$ accumulated in each bin over all configurations.

Since for the melts with longer chains, $N = 48$ and 64, the variations in the orientation of $\overline{\mathbf{n}}$ are small, it was assumed that the director frame coincides with the laboratory frame, i.e. $\boldsymbol{q} = \boldsymbol{q}^{\mathrm{L}}$. In these melts, $\boldsymbol{q}$ is placed in the yz-plane of the laboratory frame in a way that $\boldsymbol{q} = \{0, q_y, q_z\}$, with $q_{y,z} = 2\pi i_{y,z}/L_{\text{box}}$ and $-20 \leq i_{y,z} \leq 20$. Thus, in contrast to the melts with shorter chains, the $\boldsymbol{q}$-space is discrete and final spectra are obtained as averages over the $S(q_y, q_z)$ which are accumulated for each discrete $\{q_y, q_z\}$-pair over all configurations.

A representative contour plot of $S(q_y, q_z)$ for nematic melts with $N = 32$ and $N = 64$ (calculated in the director frame for $N = 32$ as described above), is presented in Fig. 3.12a. It qualitatively agrees with the theoretically predicted bowtie shape (see previous section). Similar scattering patterns have been reported in earlier simulations of lyotropic polymer nematics [140]. Fig. 3.12a demonstrates that near the origin, the scattering decreases when moving along the $q_y = 0$ axis as predicted theoretically. However for the melt with shorter chains, $N = 32$, this decay is not monotonous in the simulations and for larger q_z, a sequence of scattering minima is observed.

The additional scattering features in Fig. 3.12a do not signify smectic ordering but stem from intramolecular scattering. For a nematic $N = 32$ melt, this is shown in Fig. 3.12b by comparing $S(0, q_z)$ with the contribution from intramolecular scattering, $S_0(0, q_z)$, along the z-axis of the director frame (for clarity only the region $q_z > 0$ is shown). The intramolecular scattering is first calculated in the laboratory frame from

$$S_0(\boldsymbol{q}^{\mathrm{L}}) = \frac{1}{V} \sum_{i=1}^{n} \left\langle \left| \sum_{s=1}^{N} \exp\left(i \boldsymbol{q}^{\mathrm{L}} \cdot \boldsymbol{r}_i(s) \right) \right|^2 \right\rangle = N \rho_0 P(\boldsymbol{q}^{\mathrm{L}}). \tag{3.41}$$

Angular brackets denote an average over the chain conformations and $P(\boldsymbol{q}^{\mathrm{L}})$ stands for the molecular form factor [169]. Subsequently, the 123-frame transformation is employed in order to obtain $S_0(0, q_z)$ in the director frame from $S_0(\boldsymbol{q}^{\mathrm{L}})$. Fig. 3.12b highlights that $S(0, q_z)$ is already affected by the second of the subsidiary maxima of $S_0(0, q_z)$. The apparent difference in the location of some of the maxima of $S(0, q_z)$ and $S_0(0, q_z)$ stems from the binning of the q_z vectors used to calculate the former.

The oscillations of $S_0(0, q_z)$ manifest the strong stretching of polymers along the nematic director and are observed in all melts modeled in this study. This is illustrated in the inset of Fig. 3.12b presenting $P(0, q_z)$ for systems with $N = 16$, 32 and 64. It is instructive to compare the intramolecular scattering with the following estimate. In a melt configuration, for each i-th chain the component of the radius of gyration (squared) along the nematic director, $R^2_{\mathrm{gz(i)}}$, is obtained. Each i-th chain is assigned the form factor of a rod,

$$P_{\mathrm{rod(i)}}(q_z) = [2\sin(q_z l_{\mathrm{r(i)}}/2)/q_z l_{\mathrm{r(i)}}]^2, \tag{3.42}$$

in which q_z is taken parallel to the rod axis.

The length of the rod, $l_{\mathrm{r(i)}}$, is chosen in a way that it has the same radius of gyration (squared) as the chain, that is, $l_{\mathrm{r(i)}} = \sqrt{12R^2_{\mathrm{gz(i)}}}$. The approximate intramolecular scattering follows from

$$S_0(0, q_z) \simeq (N\rho_0)\langle P_{\mathrm{rod}}(q_z)\rangle, \tag{3.43}$$

with angular brackets denoting the average over all chains and configurations. It is presented in the main panel of Fig. 3.12b with a dashed line and roughly follows the shape of $S_0(0, q_z)$ calculated exactly via eq. 3.41. As illustrated in the inset, the loss of structure in $P(0, q_z)$ increases with chain length. This can be explained with a larger variations in chain conformations for longer molecules.

The fact that the additional scattering features in Fig. 3.12a do not stem from

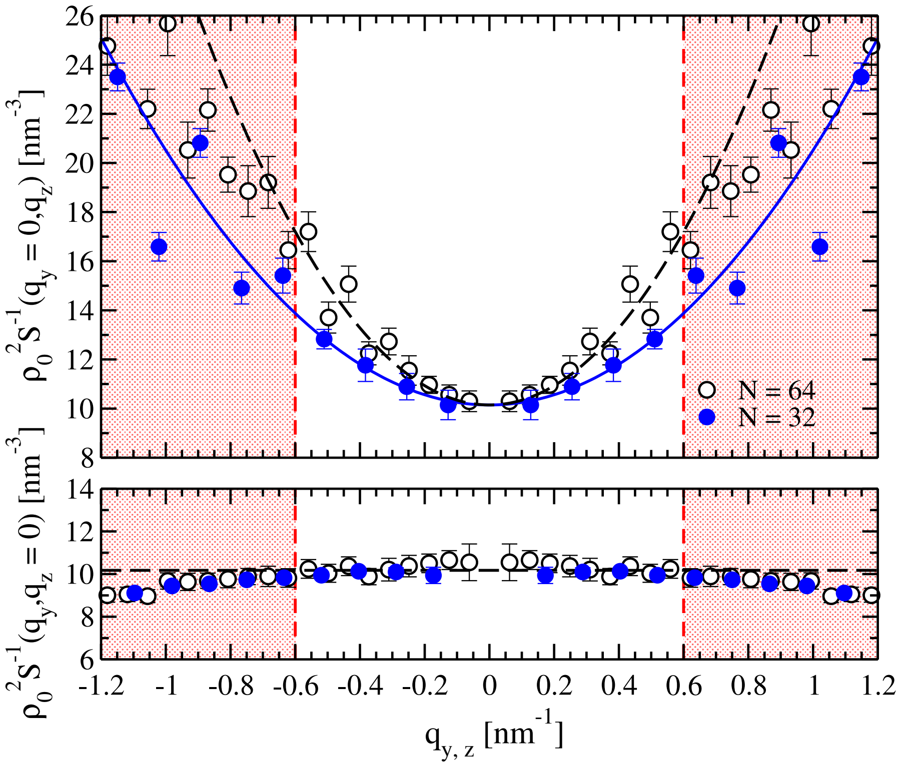

Figure 3.13: Examples of the inverse density structure factor for $N = 32$ (solid circles) and $N = 64$ (open circles) melts. The bottom panel presents $\rho_0^2 S^{-1}(q_y, 0)$ as a function of q_y and the approximation (cf. eq. 3.32) with a constant (dashed line) which is approximately the same for both N. The upper panel presents $\rho_0^2 S^{-1}(0, q_z)$ as a function of q_z. The parabolic fits for $N = 32$ and $N = 64$ are shown with solid and dashed lines, respectively. In both panels, broken red lines mark the boundaries of q-space used for the fit.

an onset of smectic order can also be seen at the one-dimensional pair correlation function measured from the chain ends projected on the z-axis pointing along the director. Fig. 3.12c depicts this quantity for the systems with $N = 32$, 48 and 64 segments per chain. The observed structuring is very weak for all chain lengths and is essentially similar to that of an ideal gas.

It is interesting to explore whether $S(q_y, 0)$ and $S(0, q_z)$ can be described by a constant and an Ornstein-Zernike form respectively, as suggested by eq. 3.32. For this purpose Fig. 3.13 presents $\rho_0^2 S^{-1}(q_y, 0)$ (lower panel) and $\rho_0^2 S^{-1}(0, q_z)$ (upper panel) as a function of q_y and q_z respectively, for $N = 32$ (blue solid symbols) and $N = 64$ (black open symbols) melts. The structure factor presented in the figure is the average of eight independently obtained values of $S(q_y, q_z)$. Accordingly, errorbars are equal to the standard deviation $\sqrt{\sigma^2(q_y, q_z)}$ of the structure factor at every scattering mode.

The bottom panel of Fig. 3.13 demonstrates that for small wave vectors, the density structure factor normal to the nematic director can be indeed approximated by a constant, which should equal $B/k_\mathrm{B}T$ (cf. eq. 3.32). The constant is marked by the horizontal black dashed line, obtained from a linear least squares fit of $\rho_0^2 S^{-1}(q_y, 0)$ in q^2-space, for $|q_y| \leq 0.6\,\mathrm{nm}^{-1}$. The extracted $B/k_\mathrm{B}T$ is presented as a function of N in Fig. 3.14 (open squares). The errorbars correspond to approximately 1% error in the estimation of B. They characterize the spread of the values obtained after splitting the independent runs for each chain length into groups with four simulations each, and calculating the B constant separately for each group. The data in Fig. 3.14 demonstrate that, for the considered chain lengths, the two-dimensional bulk modulus B does not depend on N. In principle, a weak reduction of B as N becomes larger is expected, mainly because of the smaller translational entropy of chains (compare sec. 3.5). However, such effects are not discernible in the plot.

A parabolic approximation to $\rho_0^2 S^{-1}(0, q_z)$, motivated by the Ornstein-Zernike form of eq. 3.32, is demonstrated in the upper panel of Fig. 3.13 for melts with $N = 32$ and $N = 64$ (solid blue and dashed black lines, respectively). The curves shown in the figure were obtained through a linear least squares fit of $\rho_0^2 S^{-1}(0, q_z)$ in q^2-space, with $G\tilde{\rho}_0^2/k_\mathrm{B}T$ as a free parameter while fixing $B/k_\mathrm{B}T$ to the values calculated from the analysis of $\rho_0^2 S^{-1}(q_y, 0)$. As a

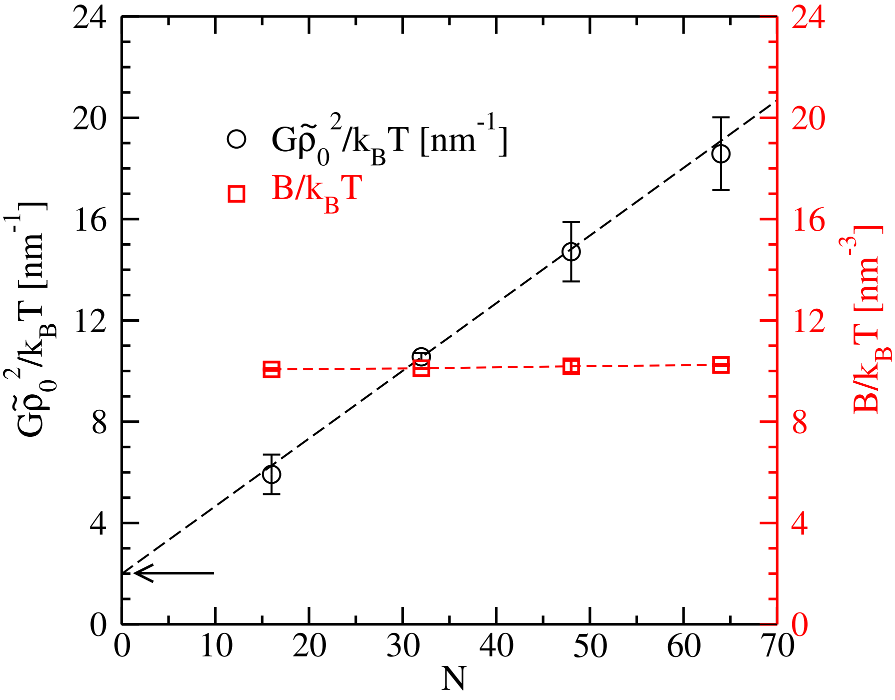

Figure 3.14: Simulation results for $G\tilde{\rho}_0^2/k_BT$ (black circles, left axis) and B/k_BT (red squares, right axis) as a function of number of chain segments, N. The arrow marks the constant offset of $G\tilde{\rho}_0^2/k_BT$.

test, the spectra allowing also for variations of $B/k_\mathrm{B}T$ have been fitted and no significant differences were observed. Moreover, the $B/k_\mathrm{B}T$, calculated in this way, match the data obtained from the analysis of $\rho_0^2 S^{-1}(q_y, 0)$ (see Fig. 3.14). For all melts the fit was performed in the region $|q_z| < 0.56\,\mathrm{nm}^{-1}$, which presents an empirical choice. Namely, as suggested by the similarity between $S_0(0, q_z)$ and the approximate intramolecular scattering calculated from the rod system, the natural choice to avoid the “jagginess” of $\rho_0^2 S^{-1}(0, q_z)$ would be to consider length scales larger than the characteristic chain dimension dominating scattering. This would correspond to $|q_z| < 2\pi/\sqrt{12R_\mathrm{gz}^2}$ (R_gz^2 follows from Fig. 3.11b). Indeed, for the shortest $N = 16$ chains, for which the effects from intramolecular scattering are the strongest, this condition is followed fitting $\rho_0^2 S^{-1}(0, q_z)$ by a parabola for $|q_z| < 2\pi/l \simeq 0.5\,\mathrm{nm}^{-1}$. At the same time, it is observed that $G\tilde{\rho}_0^2/k_\mathrm{B}T$ extracted from the parabolic approximation does not change substantially when the fit regime is expanded beyond $|q_z| = 0.5\,\mathrm{nm}^{-1}$ to incorporate periods of oscillations in $\rho_0^2 S^{-1}(0, q_z)$ (presumably because of cancellation effects). For longer chains, for which the effects from intramolecular scattering are less pronounced, $\rho_0^2 S^{-1}(0, q_z)$ is approximated by a parabola for $|q_z| \lesssim 0.6\,\mathrm{nm}^{-1}$. In this case, the fitting region includes several multiples of $2\pi/\sqrt{12R_\mathrm{gz}^2}$.

Fig. 3.14 presents the $G\tilde{\rho}_0^2/k_\mathrm{B}T$ obtained from the above procedure as a function of N (open circles). As in the case of $B/k_\mathrm{B}T$, the errorbars characterize the spread of the values for $G\tilde{\rho}_0^2/k_\mathrm{B}T$ obtained after splitting the independent runs for each chain length into groups with four simulations each. Notably, if $G\tilde{\rho}_0^2/k_\mathrm{B}T$ is fitted with an unconstrained $B/k_\mathrm{B}T$ in the corresponding fit function, the obtained values are within these errorbars. The results can be well described by a linear dependence of $G\tilde{\rho}_0^2/k_\mathrm{B}T$ on the chain length (dashed black line). This observation supports the theoretical assumption [103, 104, 108] $G \sim l$ (since $l = aN$) with the difference that in simulations, the linear dependence has a constant offset (marked by the arrow in Fig. 3.14). It is interesting that there are no clear deviations from the dependence $G\tilde{\rho}_0^2/k_\mathrm{B}T \sim N$ which was predicted in the zero-hairpin limit, even in the case of the longer melts, $N = 64$, in which almost 40% of the molecules have at least one backfolding “defect”.

3.6.4 Director fluctuation spectra and Frank constants

To obtain the spectrum of the orientation tensor for melts with $N = 16$ and 32, the Fourier transform $Q_{\alpha\beta}(\boldsymbol{q}^\mathrm{L})$ is calculated replacing in eq. 3.34 $\boldsymbol{q} = \{\boldsymbol{q}_\perp, q_z\}$ with $\boldsymbol{q}^\mathrm{L}$. The Fourier image is transformed to a $\boldsymbol{q}^\mathrm{L}$-dependent 123-frame to obtain

$$\hat{\boldsymbol{Q}}(q_y, q_z) = \hat{\boldsymbol{T}}\hat{\boldsymbol{Q}}(\boldsymbol{q}^\mathrm{L})\hat{\boldsymbol{T}}^{-1}. \tag{3.44}$$

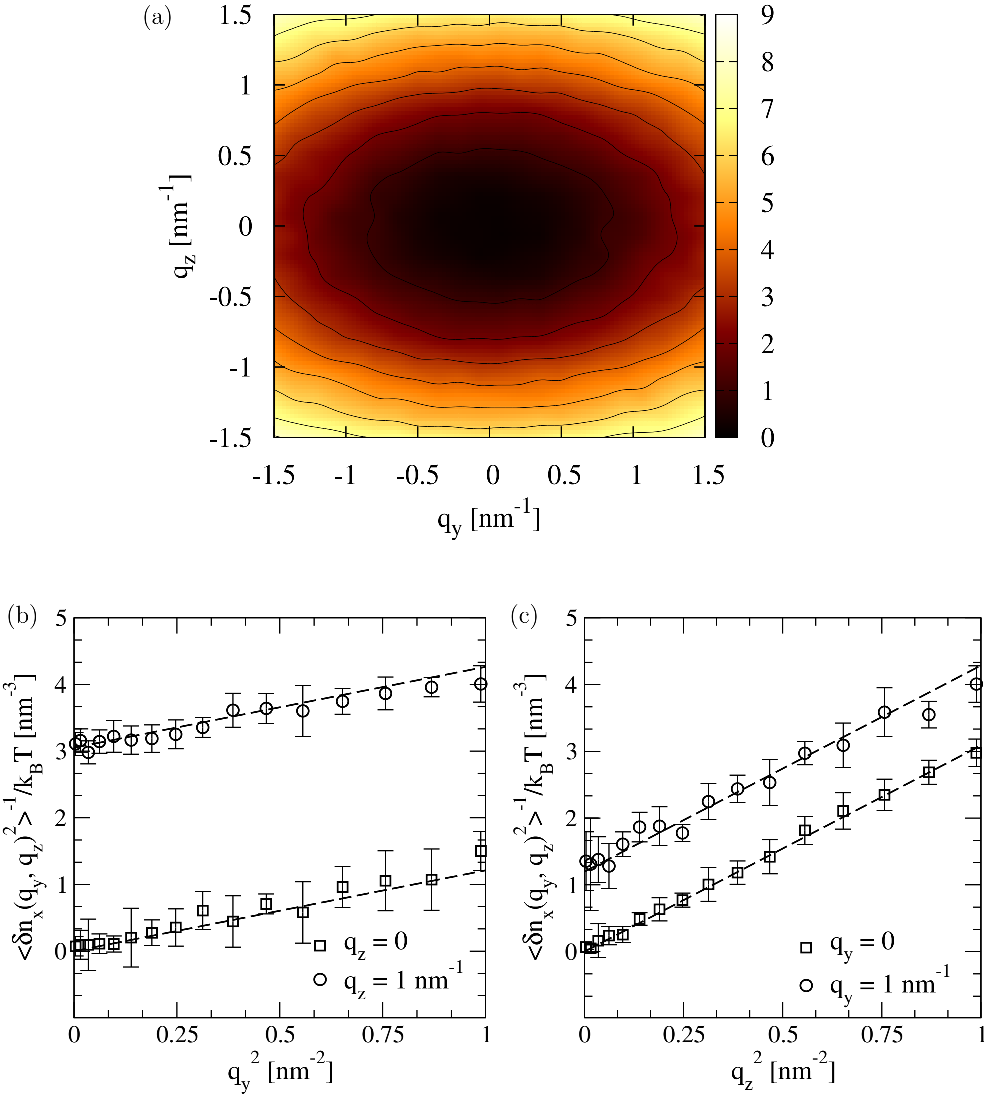

Figure 3.15: (a) Contour plot of the inverse director fluctuation spectrum, $W_{xz}(q_y, q_z)$, corresponding to twist-bend modes for a $N = 64$ melt. (b) A subset of simulation data for $W_{xz}(q_y, q_z)$ as a function of q_y^2 at two representative values, $q_z = 0$ and $1\,\mathrm{nm}^{-1}$ (squares and circles, respectively,) is presented. Dashed lines show the approximation by the analytical expression of eq. 3.45. (c) Same as (b) but considering $W_{xz}(q_y, q_z)$ as a function of q_z^2 at fixed $q_y = 0$ and $1\,\mathrm{nm}^{-1}$.

Then, $|Q_{\alpha\beta}(q_y, q_z)|^2$ is calculated and assigned to the bins of the yz-plane in the 123-frame which correspond to the rotated $\boldsymbol{q}^{\mathrm{L}}$. Final spectra are obtained as averages of the values accumulated in each bin over all configurations. As it has been clarified in sec. 3.6.3, the laboratory and the director frame can be assumed to coincide for the $N = 48$ and 64 melts. In these melts, $\boldsymbol{q}$ is placed in the yz-plane of the laboratory frame and $|Q_{\alpha\beta}(q_y, q_z)|^2$ is obtained directly via eq. 3.34 without any intermediate transformation. The final spectra are obtained as averages over $|Q_{\alpha\beta}(q_y, q_z)|^2$, accumulated for each discrete $\{q_y, q_z\}$-pair over all configurations.

Twist, K_2, and bend, K_3, constants

When the scattering vector is located in the yz-plane eq. 3.36 predicts that the fluctuations of the nematic tensor corresponding to twist-bend modes should fulfill:

$$W_{xz}(q_y, q_z) \equiv \frac{9k_{\mathrm{B}}T\langle S\rangle^2}{4\langle|Q_{xz}(q_y, q_z)|^2\rangle} = K_2 q_y^2 + K_3 q_z^2 \tag{3.45}$$

The theoretical result can describe the simulation data in a rather broad range of wave vectors, for all modeled chain lengths. This conclusion follows after fitting the right-hand side of eq. 3.45 to $W_{xz}(q_y, q_z)$ calculated from melt configurations. The fit is performed in q^2-space for $|q_{y,z}| \leq 1\,\mathrm{nm}^{-1}$ using linear least squares. The statistical error estimate for the individual modes of $W_{xz}(q_y, q_z)$ was obtained as described in sec. 3.6.3. The elliptic shape of the twist-bend fluctuation spectrum is illustrated in Fig. 3.15a, presenting a contour plot of $W_{xz}(q_y, q_z)$ for a melt with $N = 64$. An example of the accuracy of the fit is provided in Fig. 3.15b presenting a subset of simulation data for $W_{xz}(q_y, q_z)$ as a function of q_y^2 at two representative values, $q_z = 0$ and $1\,\mathrm{nm}^{-1}$ (squares and circles, respectively). For these q_z, the dashed lines in Fig. 3.15b show the approximation of the simulation data through the fit function $K_2 q_y^2 + K_3 q_z^2$, with K_2 and K_3 originating from a fit in the whole region $|q_{y,z}| \leq 1\,\mathrm{nm}^{-1}$. Fig. 3.15c presents a similar plot, considering $W_{xz}(q_y, q_z)$ as

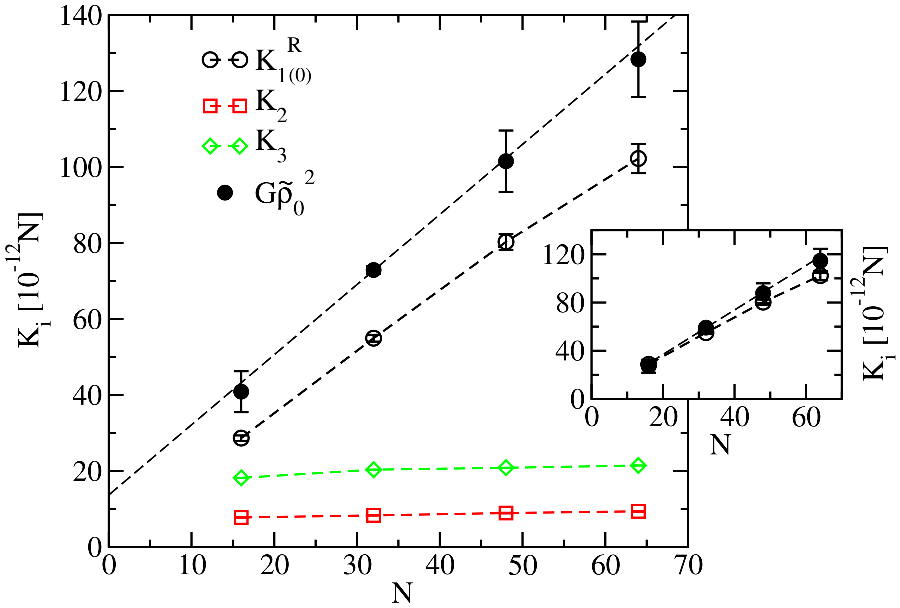

Figure 3.16: Main panel: Splay, $K_{1(0)}^R$, twist, K_2, and bend, K_3, elastic constants as a function of the number of segments in a chain. The $G\tilde{\rho}_0^2$ calculated in Fig. 3.14 is also reproduced on the plot. The absolute values for the material constants are determined assuming $T = 500\,\mathrm{K}$ as the reference temperature. Inset: Comparison of $K_{1(0)}^R$ and $G\tilde{\rho}_0^2$ after subtracting from the latter the offset indicated in Fig. 3.14.

a function of q_z^2 at $q_y = 0$ and $1\,\mathrm{nm}^{-1}$.

The twist and bend elastic constants calculated from the fit for all modeled chain lengths are presented in Fig. 3.16. Errorbars were obtained from the standard deviation of elastic constants calculated by fitting the fluctuation spectra in each of the available independent runs, separately. The robustness of the results is emphasized regarding the choice of the fitting region. Namely, choosing smaller limits, for example $|q_{y,z}| \leq 0.5\,\mathrm{nm}^{-1}$, yields very similar results for K_2 and K_3. Fig. 3.16 demonstrates that both K_2 and K_3 tend to constant values as the chain length increases, which is in agreement with theoretical arguments [103]. K_3 is roughly twice as large as K_2, while the order of magnitude of both constants is $10^{-11}\,\mathrm{N}$. Interestingly, both observations are in good agreement with experimental findings in lyotropic nematic polymers [97–99].

Splay constant K_1^R

For the splay-bend mode, the theory (see eq. 3.36) predicts

$$W_{yz}(q_y, q_z) \equiv \\ \frac{9k_\mathrm{B}T\langle S\rangle^2}{4\langle|Q_{yz}(q_y,q_z)|^2\rangle} = \underbrace{\left[K_{1(0)}^R - \frac{B\xi^4 q_z^2}{1+\xi^2 q_z^2}\right]}_{K_1^R} q_y^2 + K_3 q_z^2. \tag{3.46}$$

In the above expression, an equivalent form for the splay constant $K_1^R(q_z)$ (comparing to eq. 3.36) is employed, to facilitate fitting. It follows from eq. 3.46 that, in theory, for small wave vectors the isolines of $W_{yz}(q_y, q_z)$ should form an ellipse in the yz-plane of the director frame. As q_y and q_z increase, the contour plot of $W_{yz}(q_y, q_z)$ should transform into a figure-of-eight shape with the long axis oriented along the director.

In contrast to the twist-bend fluctuation spectra, the shapes of the splay-bend spectra $W_{yz}(q_y, q_z)$ in the simulations of melts with shorter chains ($N = 16$ and $N = 32$) do not completely match the corresponding theoretical predictions. For an illustration, Fig. 3.17a presents a contour plot of $W_{yz}(q_y, q_z)$ for a $N = 16$ melt. While the general shape of the plot follows the theoretical expectations, the isolines exhibit a sequence of “wiggles”. Contrary to the case of density structure factors (compare Fig. 3.12a) these additional features stem from intermolecular correlations and not from intramolecular scattering directly. This conclusion follows after considering the contribution of intramolecular scattering, obtained by calculating the Fourier transformation of the nematic tensor for each i-th molecule in the laboratory frame first,

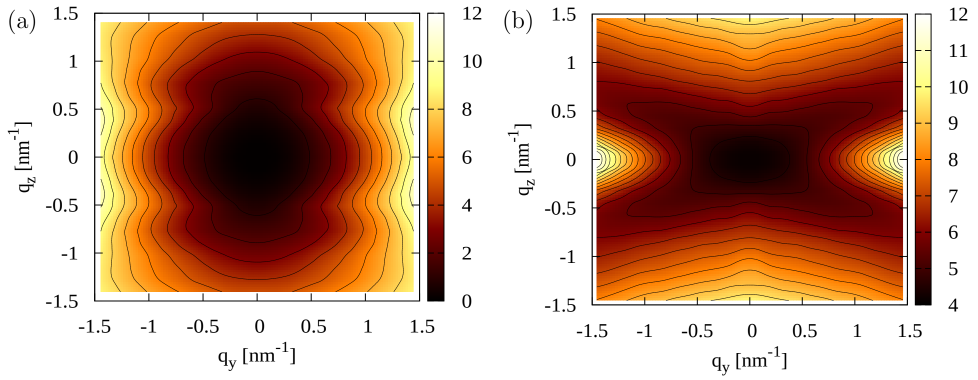

Figure 3.17: (a) Contour plot of the inverse director fluctuation spectrum, $W_{yz}(q_y, q_z)$, of the splay-bend modes in a $N = 16$ melt, illustrating the "wiggles" in the pattern of contour lines. (b) Contour plot of the inverse single-chain director fluctuation spectrum, $w_{yz}(q_y, q_z)$, for the same melt, presenting a cross-like pattern of minima.

according to

$$Q_{i,\alpha\beta}(\boldsymbol{q}^{\mathrm{L}}) = \frac{1}{\sqrt{V}\rho_0} \sum_{s=1}^{N} q_{i,\alpha\beta}(s) \exp\left(i\boldsymbol{q}^{\mathrm{L}} \cdot \boldsymbol{r}_i(s)\right). \tag{3.47}$$

For each chain, the Fourier image of the molecular nematic tensor is transformed to a $\boldsymbol{q}^{\mathrm{L}}$-dependent 123-frame to obtain

$$\hat{\boldsymbol{Q}}_i(q_y, q_z) = \hat{\boldsymbol{T}}\hat{\boldsymbol{Q}}_i(\boldsymbol{q}^{\mathrm{L}})\hat{\boldsymbol{T}}^{-1}, \tag{3.48}$$

and the total part of intramolecular scattering is given by

$$w_{yz}^{-1}(q_y, q_z) \equiv 4n \sum_{i=1}^{n} Q_{i,yz}(q_y, q_z)/9\langle S\rangle^2 k_B T. \tag{3.49}$$

Fig. 3.17b presents the contour plot of $w_{yz}(q_y, q_z)$ for $N = 16$ demonstrating that it has a different pattern comparing to $W_{yz}(q_y, q_z)$. For short chains, the cross-like shape of minima in $w_{yz}(q_y, q_z)$, not observed in the total scattering, stems from strong correlations in the orientation of segments along the same molecule due to stiffness. The instantaneous tilt angle θ_{s} of a segment axis with respect to the director $\overline{\mathbf{n}}$ has an average value larger than zero, i.e. $\langle\theta_{\mathrm{s}}\rangle > 0$. In Fig. 3.17b, the angles between the branches of the cross and the q_y-axis depend on the magnitude of $\langle\theta_{\mathrm{s}}\rangle$. Indirectly, however, the intermolecular correlations leading to the distortions in Fig. 3.17a are still coupled to the chain connectivity. This follows from the observation that they are located at wave vectors roughly corresponding to the contour length of the polymer chains. For longer polymers, the distortions of the isolines not only shift to smaller wave vectors but become also less pronounced.

Fig. 3.18a presents the contour plot of $W_{yz}(q_y, q_z)$ for the longest $N = 64$ melt, which is in very good agreement with the shape predicted by eqn. 3.46. This can be quantified by fitting the $W_{yz}(q_y, q_z)$ obtained in the simulations for $|q_{y,z}| \leq 1\,\mathrm{nm}^{-1}$ by the functional form suggested by eqn. 3.46. Fig. 3.18b considers two representative values $q_z = 0$ and $1\,\mathrm{nm}^{-1}$ to demonstrate that the fitted function (dashed lines) describes the original data (squares and circles, respectively) closely at different values of q_z. Fig. 3.18c provides a similar comparison, now considering $W_{yz}(q_y, q_z)$ as a function of q_z^2 at two representative values, $q_y = 0$ and $1\,\mathrm{nm}^{-1}$. Notably, the value of the bend constant K_3 obtained from this fit matches the value extracted from the twist-bend fluctuations.

For all chain lengths, the small wave length behavior of the splay constant, $K_{1(0)}^R$, is presented in Fig. 3.16 (open circles). It was extracted from linear fits to $W_{yz}(q_y, q_z)$ as a function of q_y^2, while setting $q_z = 0$. For melts without significant hairpin effects, the plot suggests a linear dependence of $K_{1(0)}^R$ on N as first predicted by Meyer. For polymer nematics with a large number of hairpins per chain, it has been predicted theoretically that $K_{1(0)}^R$ should reach a

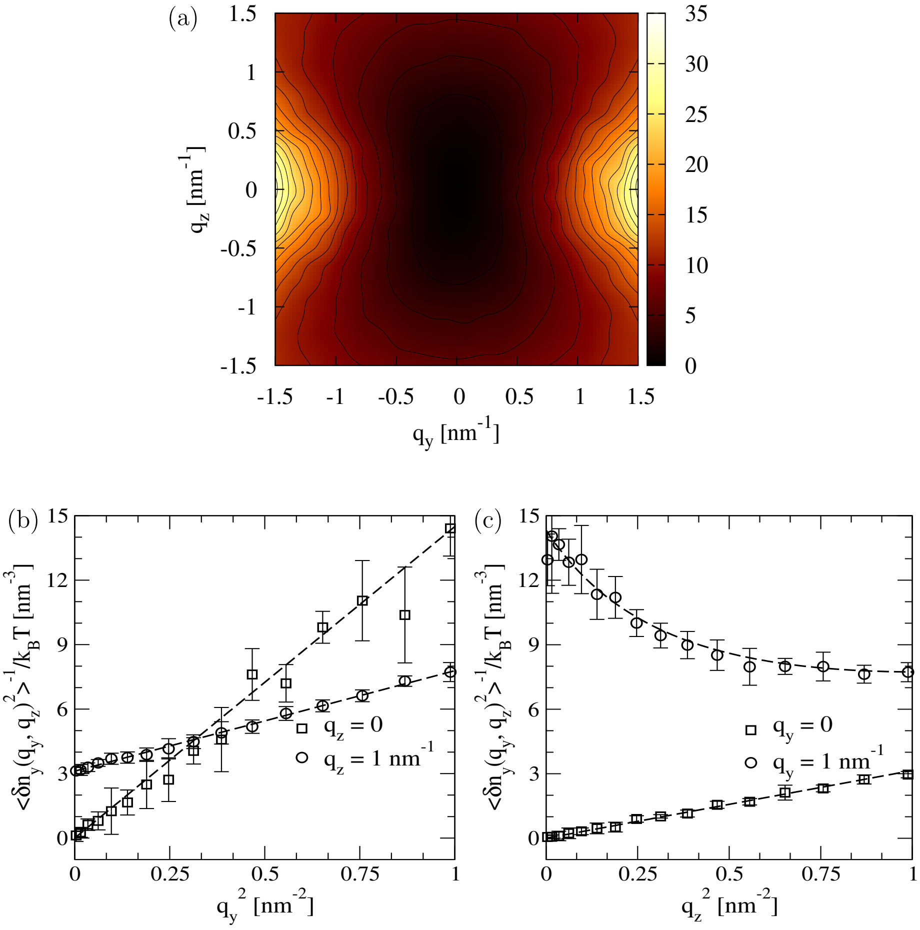

Figure 3.18: (a) Contour plot of the inverse director fluctuation spectrum, $W_{yz}(q_y, q_z)$, corresponding to splay-bend modes for $N = 64$ melt where no "wiggles" are observed. (b) A subset of simulation data for $W_{yz}(q_y, q_z)$ as a function of q_y^2 at two representative values, $q_z = 0$ and $1\,\mathrm{nm}^{-1}$ (squares and circles, respectively) is presented. Dashed lines show the approximation by the analytical expression of eq. 3.46. (c) Same as (b) but considering $W_{yz}(q_y, q_z)$ as a function of q_z^2 at fixed $q_y = 0$ and $1\,\mathrm{nm}^{-1}$.

finite value as a function of N, which is related to a statistical segment length (and, hence, the persistence length) for chains with many hairpins [116]. Thus, for longer chains with moderate backfolding (such as $N = 64$), the onset of saturation, i.e., sublinear dependence of $K^R_{1(0)}$ on N, might be expected. In fact for $N = 64$, the simulations suggest the appearance of such effects, manifested by the slight "bending" of $K^R_{1(0)}$ with increasing chain length. However, such effects lie within the estimated errorbars (compare Fig. 3.16).

An important question refers to the extent to which the above results are affected by finite system size effects. For $N = 16$ the splay constant obtained from test simulations in smaller cells, $L_{\text{box}} = 4L$, matched the $K^R_{1(0)}$ in Fig. 3.16 (obtained at $L_{\text{box}} = 8L$). However, in simulations of the longest melts, in which $L_{\text{box}} = 2L$ is employed, fluctuations could be more suppressed, resulting into Frank constants that are larger comparing to those of an "infinite" system. Therefore, in larger samples of these melts splay constants might reduce leading, e.g., to more pronounced saturation effects.

In Fig. 3.16 the quantity $G\tilde{\rho}_0^2$ previously calculated from density fluctuations (compare Fig. 3.14) is also reproduced as a function of N. According to the theoretical prediction $K^R_{1(0)} = K_1 + G\tilde{\rho}_0^2$ one expects that: a) $K^R_{1(0)}$ has the same slope comparing to $G\tilde{\rho}_0^2$ as a function of N and b) $K^R_{1(0)} \geq G\tilde{\rho}_0^2$ is larger than $G\tilde{\rho}_0^2$, since K^R_1 is nonnegative. In Fig. 3.16, for short chains, $G\tilde{\rho}_0^2$ has a slope similar to $K^R_{1(0)}$, which agrees with the first expectation. At the same time, in simulations $G\tilde{\rho}_0^2$ is larger than $K^R_{1(0)}$. One can argue that this difference from the theoretical result is due to the constant offset in the linear dependence of $G\tilde{\rho}_0^2$ on N observed in Fig. 3.14. The inset of Fig. 3.16 compares $K^R_{1(0)}$ and $G\tilde{\rho}_0^2$, subtracting from the latter the offset $1.99k_BT$ obtained in Fig. 3.14. In this case the two curves are very close to each other, for short chains.

3.7 Conclusions

In this chapter, within a Monte Carlo simulation study, the applicability of a soft, generic model has been demonstrated for studying director and density fluctuation spectra in nematic liquid crystalline polymer (LCP) melts. In order to do so, a model presented earlier [69] has been adopted and developed further. The non-bonded interactions between polymer segments are therein evaluated on the basis of a soft potential, which incorporates distance and orientation dependent contributions. The distance dependent part is analytically derived from an overlap integral of spherical density clouds.

Due to the softness of the potential and hence the allowance of significant segment overlap, the equilibration of large scale morphologies of nematic LCP with up to $N = 64$ repeat units was possible. With these morphologies at hand, and in particular with the explicit segment orientations retained in the particle-based model, it was possible to analyze director and density fluctuations in a large regime of wave lengths. The simulation box size was a multiple of the size of an extended chain.

As one of the main results of the study, the simulations strongly support the linear scaling prediction for the splay Frank elastic constant with chain length, as it was first proposed by Meyer [103], in disagreement with the earlier result of de Gennes [101, 102].

It is stressed that the analytical work [103, 104, 108] addressed the limit of zero hairpin folding only, thus chains are fully stretched. In fact, it can be seen from the results in ch. 3.6.2 that hairpins can always be found in the considered systems. It would be interesting to see if the slight deviation of the splay constant scaling from its linear trend, as indicated from the analysis presented in Fig. 3.16, becomes more pronounced for longer chains, with more backfolding events per chain on average.

The soft model approach has shown suitable for studies on the scales addressed here, since the simple model potential in combination with local and global

Monte Carlo moves allows an efficient sampling of the phase space. However, in order to study the behavior of the Frank elastic constants for the regime of saturated chain backfolding [116, 137], one has to proceed to even larger systems with longer chains. In that way, it may be possible to investigate the different scaling regimes for the elastic constants in a unified way, e.g. linear behavior of the splay constant in the regime with few hairpins and the onset of saturation of the latter for systems with many hairpins. This is not feasible with the approach used in this thesis. Thus, there is a demand for addressing the problem with more sophisticated simulation approaches. The Monte Carlo algorithm could be optimized by using more advanced sampling techniques, e.g. biased reptation or more global update moves. Following another direction, one may think of an implementations for highly parallel Molecular Dynamics (MD) simulations. A parallel implementation may be straightforward with the off-lattice, particle-based chain model introduced in this study, however the implementation of the orientation dependent interactions in a standard force-based MD simulation might require special techniques.

4 Modeling biaxial mesophases of poly(3-hexylthiophene)

Parts of this chapter are based on the following article:
P. Gemünden, C. Poelking, K. Kremer, D. Andrienko, and K. Ch. Daoulas, "Nematic Ordering, Conjugation, and Density of States of Soluble Polymeric Semiconductors", Macromolecules 46, 5762–5774 (2013) (cover article).
The results discussed in this chapter, in particular in ch. 4.3.2 and ch. 4.5.2, are the outcome of a collaboration with Carl Poelking and Denis Andrienko from the Organic Electronics Group of the Theory Department at the Max-Planck-Institute for Polymer Research in Mainz. The author of this thesis focussed on the investigations regarding the morphology of the material, while the investigations regarding charge transport were the main focus of the contributions by Carl Poelking.

In chapter 3, a soft, anisotropic, generic polymer model was used for studying nematic LC mesophases of semi-flexible (worm-like) chains. It was found that such models, which are based on simple top-down constructions of phenomenological non-bonded interactions, can be used for addressing generic, fundamental physical questions regarding the macroscopic material properties of liquid crystalline polymers. In the present chapter, this approach will be further elaborated, in order to describe, first, complex mesophase structuring, and, second, specific molecular geometries. A model will be developed which is capable of describing biaxial-nematic morphologies, i.e. mesophases with a symmetry that is reduced compared to uniaxial (cylindrical-symmetric) systems. Conceptually, the main modification of the modeling framework, compared to the previous chapter 3, is to account for an additional tensorial coupling term in the effective Hamiltonian eq. 3.20. The approach is applied, as a test case, to the molecule poly(3-hexylthiophene) (P3HT), a polymer typically used in organic electronics research. Subsequently, generic structure-property relations for the model morphologies are studied, e.g. the influence of long-range mesoscale order on the energy landscape of the material.

4.1 Background

In organic electronics, soluble polymeric semiconductors build a class of materials with promising properties for applications in mechanically flexible devices. Typical examples are organic light emitting diodes (OLED), organic field-effect transistors (OFET), and organic solar cells (OPV) [170–173]. The characteristic feature of the molecular architecture of semiconducting polymers is a semirigid conjugated backbone. Due to the conjugation, an injected charge carrier is able to travel along the molecular contour (see the book of Geoghegan and Hadziioannou [174] for an overview of the chemistry of conjugated polymers). Due to the strong interaction between conjugated backbones, bulk processing of these polymers is usually impractible [175]. However, solubility and therefore the potential for a low-cost processing can be achieved by functionalizing short aliphatic side chains. Poly(3-hexylthiophene) (P3HT) is an example of a soluble semiconducting polymer which is experimentally and theoretically well studied [141]. In practical applications, it showed a promising performance in active layers of organic solar cells, in which it is blended together with the fullerene derivative phenyl-C61-butyric acid methyl ester (PCBM) [176] (see Fig. 1.2).

The energetically favorable backbone conformation of P3HT is an all-*trans*-

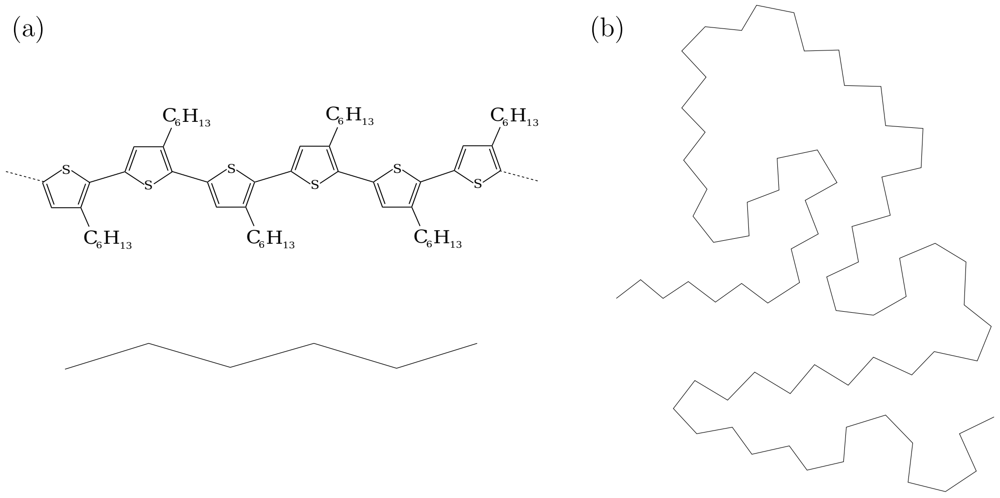

Figure 4.1: (a) Upper scheme: Illustration of a part of a poly(3-hexylthiophene) in a low energy state. In the all-*trans* configuration, neighboring thiophene rings are aligned co-planar. The lower scheme illustrates the typical zig-zag configuration according to the connecting C-C bonds. (b) At finite temperature, *cis*-configurations are increasingly present. For very long chains in solution, the chain conformation may be described as a random coil [174]. Locally, however, the polymer is relatively stiff. Fig. (b) is adapted from Ref. [174].

configuration, leading to a typical zig-zag-structure, see Fig. 4.1a. Thermal fluctuations lead to an increased population of *cis*-configurations. Accordingly, the backbone orientation correlation decays quickly in solution, and the backbones resemble semi-flexible chains with a certain persistence length, see schematic in Fig. 4.1b. The molecular conformation partitions the chain into planar sub units (*conjugated segments*) due to backbone twisting (torsional defects). The distribution of conjugated segments within the molecule influences the charge transfer properties along the backbone, due to increased localization of the excess carrier that results from a stronger fragmentation of the chain.

The morphology of polymeric semiconductors is extremely difficult to predict and to control in both experiments and first-principle molecular simulations. Due to π-stacking interactions, the material exhibits a lamellar-like, crystalline packing in the solid state [177] (compare Fig. 1.2c). Additionally, different crystal structures are observed depending on the processing conditions [175, 178, 179]. An increased charge carrier mobility is observed in the crystalline phase due to the large electronic overlap in the lamellar configuration [175, 180]. Charge transfer in (semi-)crystalline morphologies of polymeric semiconductors can be described as a series of hopping events between conjugated segments [181]. The time scales for intra- and inter-molecular transfer differ significantly, and the intermolecular hopping, which proceeds in the non-adiabatic regime of charge transfer, is the mobility-limiting step (compare Ref. [181] for a more detailed discussion of charge transport in polymeric semiconductors). An approximate expression of the latter transfer rate is given by Marcus theory [182].

On even larger scales, the solid state morphology of P3HT and other conjugated polymers is governed by inhomogeneously distributed areas of either amorphous or partially crystalline domains [180]. The long-range correlations due to the chain connectivity and the conformational frustration of side chains impede the control of backbone order during the processing. Depending on processing conditions, the structure may be arrested in a kinetically stable state. Due to packing problems of the side chains, the crystallinity and therefore the conjugation of backbones and the electronic overlap between localization units may be reduced. Charge transport in the material is therefore affected by these large-scale morphological features [141, 183]. Recently, a possible improvement of molecular ordering and, hence, of the charge transport properties was reported for materials annealed via a liquid crystalline (LC) mesophase [145–147, 183]. Such an intermediate state of mesophase ordering was reported above the melting temperature for various polymeric semiconductors [142–149, 184].

4.2 Motivation

This part of the thesis focusses on the morphology of polymeric semiconductors and specifically on the question how the latter is connected to charge transfer related properties. Ultimately, the knowledge of structure-process-property relationships is desirable for an efficient design of components and devices. In order to approach this with simulations, large systems need to be addressed, because spatial correlations due to chain connectivity extend over length scales exceeding $\geq 10\,\mathrm{nm}$. Significantly coarse-grained models can help to overcome some of these problems. Nevertheless, for connecting the large-scale morphology with charge transfer-related material properties, one has to link between the scales. On the one hand, the essential molecular features that affect the molecular ordering and mesoscale structuring in this class of materials have to be incorporated. On the other hand, a sufficiently coarse-grained representation has to be used in order to reach device-relevant scales.

In the past, several coarse-grained modeling approaches for polymeric semiconductors have been proposed. The most detailed of those were the three-site models, in which a set of effective potentials was derived, representing one hexylthiophene unit by three coarse-grained sites. The side chains are to some extend explicitly retained in the coarse-grained description [185–188]. However, the level of detail comes with relatively high computational cost, and the three-site approach is usually limited to a small number (up to several hundreds) of molecules. An attempt to combine some of the microscopic features typical for conjugated polymers (e.g., chain stiffness) with a coarser particle-based level of description has been proposed [69], allowing to address larger systems. Zooming out to larger scales, field-based methods have been used recently to describe charge transport processes in polymeric semiconductor blends [189]. However, none of the drastically coarse-grained approaches takes into account the planar shape of monomers and π-stacking interactions.

In this chapter, the problem of modeling the hierarchically structured, partially crystalline morphology of polymeric semiconductors is approached, in a first step, via a less ordered state, namely the liquid crystalline phase. Along the example of P3HT, a *top-down* model is developed, which is capable of generating biaxial liquid-crystalline mesophases of P3HT (see ch. 4.1). In this way, the molecular packing accounts not only for an on average parallel alignment of the chain backbones, but reflects the planar packing of backbone segments due to π-stacking interactions in a generic way. The approach is combined with a systematic bottom-up modeling of chain backbone configurations, derived from an atomistic single chain reference simulation. From the analysis of large, equilibrated mesophases, results will be presented for the impact of mesoscale ordering on molecular conformations and, eventually, the energetic landscape relevant for charge transport.

4.3 Coarse-grained model for biaxial-nematic polymers

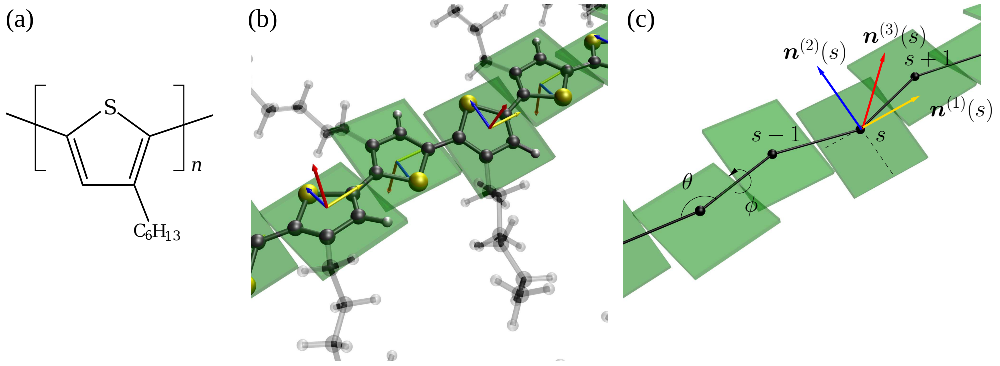

Figure 4.2: (a) Chemical structure of poly(3-hexylthiophene) (P3HT). (b) Atomistic and (c) coarse-grained representations of the P3HT chain. The coarse-grained interaction site is located at the intersection of two imaginary lines along the C-C-bonds which connect neighboring thiophene rings.

The coarse-grained model is developed by first defining a mapping scheme [15] and subsequently splitting the interactions, as it is frequently done in (classical) polymer simulations [8, 190, 191], into a bonded and a non-bonded part.

4.3.1 Coarse-grained mapping

An explicit, systematic mapping of atomistic to coarse-grained degrees of freedom is chosen (compare ch. 2.1), in a way that a whole hexylthiophene unit is mapped onto a single coarse-grained interaction site. A coarse-grained site represents the whole group of atoms that belong to the monomer [14, 54], *including* the atoms associated with a hexyl chain. A typical choice for the locations of the coarse-grained mapping points are the centers-of-masses of the atoms belonging to a monomer. However, for specific molecular architectures, such a mapping may lead to correlated coarse-grained degrees of freedom [192]. For P3HT, consecutive *trans*-angles lead to a backbone configuration in which a thought connection of thiophene ring centers along the chain backbone renders a zig-zag line, leading to the typical backbone configurations illustrated in Fig. 4.1. Therefore, mapping points are chosen in a way that the connection between ring centers coincide with the C-C-bonds between adjacent thiophene rings. In other words, the coarse-grained mapping points are located at the intersection of two imaginary lines along these C-C bonds. In fact, with this choice, the correlation of coarse-grained angular, θ, and torsional, ϕ, degrees of freedom is minimized, which is monitored by measuring the cross-correlation obtained from the trajectory of an atomistic reference simulation using the VOTCA package [44]. It is verified that an offset of $\pm 20\%$ in the system temperature has no significant effect on the distributions of the coarse-grained degrees of freedom. In the following, the distribution for the bonded degrees of freedom will be solely adjusted through the Boltzmann factor $k_B T$.

4.3.2 Bonded interactions

The derivation of the coarse-grained bonded potentials was carried out in collaboration with Carl Poelking and Denis Andrienko. For this purpose, a Molecular Dynamics reference simulation has been performed for a single, fully atomistic P3HT chain with 20 monomers at temperature $T = 370\,\mathrm{K}$ with a Langevin-dynamics integrator as implemented in the GROMACS package [47]. A Langevin thermostat with coupling constant $\tau = 1\,\mathrm{ps}$ has been used. All interactions across more than two monomers along the backbone were excluded in this run, which is consistent with the choice of exclusion for the coarse-grained non-bonded potential at a later stage. The force field used for

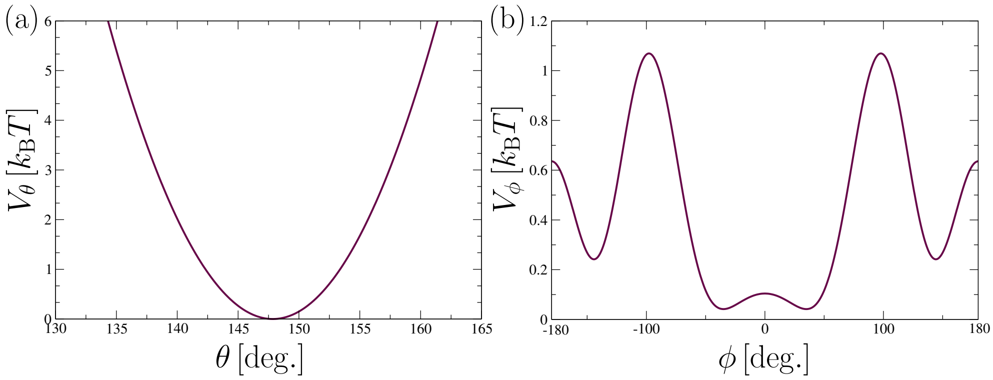

Figure 4.3: (a) Bonded potential and (b) Ryckaert-Bellemans torsion potential [193], obtained from Boltzmann Inversion of an atomistic single chain reference statistics.

the sampling is a re-parameterized version [175] of the OPLS-AA force field [194, 195], since the original OPLS-AA force field may be problematic for the modeling of inter-ring torsion potentials in conjugated systems [196]. Details on the choice of force field can be found elsewhere [175].

From the atomistic reference, the distributions of the bond length, angle and torsional angle were obtained. For angular and torsional interaction potentials, harmonic angular and Ryckaert-Bellemans torsion potentials [193] are defined by

$$V_\theta = \frac{\kappa_\theta}{2}\left(\theta - \theta_0\right)^2, \qquad V_\phi = \sum_{j=0}^{5}(-1)^j c_j \cos^j \phi. \tag{4.1}$$

Subsequently, the parameters κ_θ, θ_0, and c_j have been derived from a Boltzmann inversion of the angular distributions using the VOTCA-CSG coarse-graining package [44] and a subsequent fit of the analytical expressions in eq. 4.1 to the data.

In Table 4.1, fitted values for the potential parameters are shown. Fig. 4.3 shows the angular and torsion potential from eq. 4.1 for this specific parameterization. The bond length, which has also been monitored in the atomistic

θ_0	κ_θ
147.46	462.653

c_0	c_1	c_2	c_3	c_4	c_5
2.75248	-1.37645	-5.29397	3.19667	3.12177	-2.41059

Table 4.1: Coarse-grained bonded potential parameters (eqs. 4.1) obtained from Boltzmann inversion of the angular distributions. The angle θ_0 is given in degrees and κ_θ given in $\mathrm{kJ/(mol\ rad^2)}$. The c_i-expansion parameters are all given in $\mathrm{kJ/mol}$.

simulation, fluctuates around a mean value $b = 0.40\,\mathrm{nm}$, with a standard relative deviation of less than $0.1\,\%$. In the coarse-grained simulations, the bond length is kept fixed.

In order to validate the parameterization, in Fig. 4.4, the bond orientation correlation and the end-to-end distance distribution is shown, comparing the set of data obtained from an atomistic reference simulation and from a coarse-grained simulation. For the bond orientation correlation, Fig. 4.4a, the red squares show the data obtained from the all-atom reference simulation. The solid black line is similarly obtained from a coarse-grained single chain simulation at the same reference temperature $T = 370\,\mathrm{K}$. The data obtained from the coarse-grained sampling reproduces the data from the reference chain well. More interestingly, the green circles show the similar data set obtained from a coarse-grained bulk simulation (however non-bonded interactions will be discussed later) at a temperature $T = 500\,\mathrm{K}$. The comparison with the other two curves shows that the stiffness of a chain in bulk is similar to that of the isolated chain even for the relatively short chains considered, as it is expected in the limit of very long chains reflecting quasi-Θ-solvent conditions [19]. It is also demonstrated that the bonded potentials are not very sensitive to the temperature of the simulation. Similar conclusions can be drawn for the end-to-end distance distribution, shown in Fig. 4.4b.

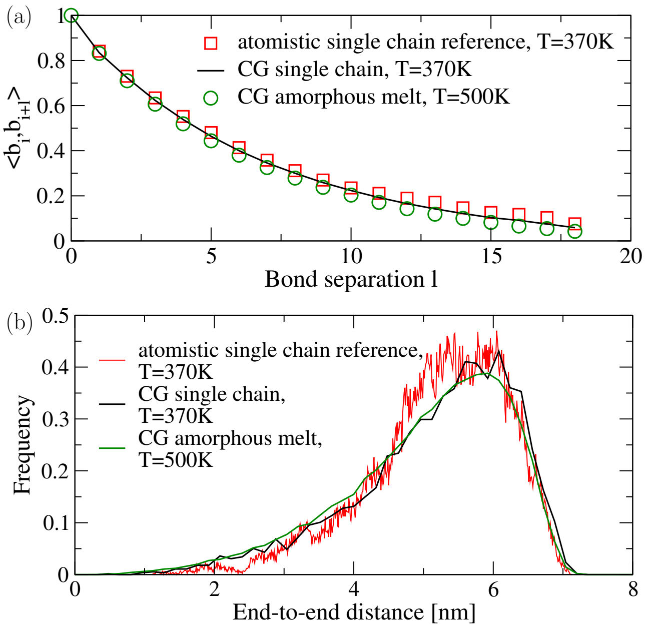

Figure 4.4: (a) Bond orientation correlation, calculated from the atomistic single chain reference trajectory, compared with the same quantity calculated from a CG single chain and amorphous melt. The vector b_i points along the bond connecting two thiophenes. The data for the melt is shown for the reference temperature $T = 500\,\mathrm{K}$, where the potential was simply rescaled (see main text for details). (b) End-to-end distance averaged over chains, obtained from the atomistic reference chain and a CG single chain at $T = 370\,\mathrm{K}$.

4.3.3 Non-bonded interactions

In this section, the novel framework for developing the non-bonded interactions will be explained in detail. In contrast to the systematic derivation of bonded interactions, described in the previous section, the non-bonded interactions are developed using a top-down approach.

Anisotropic interaction

The model for the non-bonded, pairwise interactions is developed for a relatively coarse molecular representation (compare Fig. 4.2). For the P3HT chain, each hexylthiophene is mapped onto a single coarse-grained interaction site. It is important to convey with the mapping some of the most relevant underlying microscopic features to the coarse description level. The coarse-grained model should include the effect of conformational frustration of side chains and π-stacking interactions of aromatic rings (backbones) [177, 197]. The molecular anisotropy in real polymeric semiconductor materials has a strong impact on the structure at large scales, as observed in, for example, lamellar (crystalline), discotic or nematic mesophases [177, 184, 198].
At the coarse description level addressed in the present framework, a systematic bottom-up modeling of non-bonded interactions is not feasible because of the limited transferability of effective interactions [55, 190, 199] (compare also ch. 2.1). For this reason, non-bonded interactions are introduced phenomenologically in the following, combining soft repulsive interactions with anisotropic coupling of coarse-grained sites.

The development of non-bonded interactions is in the same spirit as in ch. 3. Here, as a new feature, biaxial symmetry is introduced via a biaxial-nematic order parameter [28, 200, 201] on the level of an effective functional, in order to capture the directionality of effective interactions and the mesophase symmetry of the real material (compare Fig. 1.2 and Fig. 4.2)

The directionality of monomers is mimicked by considering the coarse-grained segments as objects with plate-like symmetry ($D_{2\mathrm{h}}$), as it is often done in theoretical approaches to biaxial-nematic LC phases [27, 201, 202].
To the s-th site in a molecule with index i, an orthonormal set of vectors is assigned, $\{\boldsymbol{n}_i^{(1)}(s), \boldsymbol{n}_i^{(2)}(s), \boldsymbol{n}_i^{(3)}(s)\}$, where $i = 1, \ldots, n$ and $s = 1, \ldots, N$

(compare Fig. 4.2). Here, n is the number of molecules in the system and N is the degree of polymerization. The orientation of these vectors is fixed by the conformation of the chain and is shown in Fig. 4.2c. The molecular orientations are chosen according to the following geometric constructions:

$$\begin{aligned}&\boldsymbol{n}_i^{(1)}(s) \parallel \boldsymbol{r}_i(s+1) - \boldsymbol{r}_i(s-1),\\&\boldsymbol{n}_i^{(2)}(s) \parallel (\boldsymbol{r}_i(s+1) + \boldsymbol{r}_i(s-1))/2 - \boldsymbol{r}_i(s),\end{aligned} \tag{4.2}$$

in which $\boldsymbol{r}_i(s)$ is the position of the coarse-grained interaction site s in a molecule i (indicated as beads in Fig. 4.2c, compare also Fig. 3.7). The orientation of $\boldsymbol{n}_i^{(3)}(s)$ is given by the orthonormality of the set. For the ends of the chain, the orientation vectors can be defined by adding additional “ghost” bonds. The torsional and angular degrees of freedom of these auxiliary bonds are also subjected to the bonded potentials of eq. 4.1.

In order to approximately capture the macroscopic thermodynamic behavior of the real system, e.g. a limited compressibility and biaxial-nematic ordering, the following functional is postulated [27, 202]:

$$\begin{aligned}H_{\mathrm{nb}}\left[\hat{\rho}, \hat{\boldsymbol{Q}}^{(1)}, \hat{\boldsymbol{B}}\right] &= \int d\boldsymbol{r}\, \frac{\bar{\kappa}\rho_0}{2}\left(\frac{\hat{\rho}(\boldsymbol{r})}{\rho_0} - 1\right)^2\\&- \frac{\bar{\nu}\rho_0}{3}\int d\boldsymbol{r}\, \hat{\boldsymbol{Q}}^{(1)}(\boldsymbol{r}) : \hat{\boldsymbol{Q}}^{(1)}(\boldsymbol{r})\\&- \frac{\bar{\mu}\rho_0}{3}\int d\boldsymbol{r}\, \{\hat{\boldsymbol{Q}}^{(1)}(\boldsymbol{r}) : \hat{\boldsymbol{B}}(\boldsymbol{r}) + \hat{\boldsymbol{B}}(\boldsymbol{r}) : \hat{\boldsymbol{Q}}^{(1)}(\boldsymbol{r})\}\\&- \frac{\bar{\lambda}\rho_0}{4}\int d\boldsymbol{r}\, \hat{\boldsymbol{B}}(\boldsymbol{r}) : \hat{\boldsymbol{B}}(\boldsymbol{r}).\end{aligned} \tag{4.3}$$

Even though only the biaxial order tensor $\hat{\boldsymbol{B}}(\boldsymbol{r})$ is new in eq. 4.3, while the segment density $\hat{\rho}$ and the nematic order tensor $\hat{\boldsymbol{Q}}(\boldsymbol{r})$ have already been introduced in ch. 3, the full set of local order parameter fields is given here for clarity of the further discussions:

$$\begin{aligned}\hat{\rho}(\boldsymbol{r}) &= \sum_{i=1}^{n}\sum_{s=1}^{N}\delta(\boldsymbol{r}-\boldsymbol{r}_i(s))\\ \hat{Q}^{(1)}_{\alpha\beta}(\boldsymbol{r}) &= \sum_{i=1}^{n}\sum_{s=1}^{N}\frac{\delta(\boldsymbol{r}-\boldsymbol{r}_i(s))}{\rho_0}q^{(1)}_{i,\alpha\beta}(s)\\ \hat{B}_{\alpha\beta}(\boldsymbol{r}) &= \sum_{i=1}^{n}\sum_{s=1}^{N}\frac{\delta(\boldsymbol{r}-\boldsymbol{r}_i(s))}{\rho_0}b_{i,\alpha\beta}(s).\end{aligned} \tag{4.4}$$

Note the identification $\hat{\boldsymbol{Q}}^{(1)}(\boldsymbol{r}) = \hat{\boldsymbol{Q}}(\boldsymbol{r})$, with a superscript (1) being introduced for later convenience. The molecular tensors $\boldsymbol{q}^{(k)}$ (where $k = 1, 2, 3$) and $\boldsymbol{b}$ are defined as:

$$\begin{aligned}q^{(k)}_{i,\alpha\beta}(s) &= \frac{3}{2}n^{(k)}_{i,\alpha}(s)n^{(k)}_{i,\beta}(s) - \frac{\delta_{\alpha\beta}}{2}\\ b_{i,\alpha\beta}(s) &= n^{(2)}_{i,\alpha}(s)n^{(2)}_{i,\beta}(s) - n^{(3)}_{i,\alpha}(s)n^{(3)}_{i,\beta}(s)\end{aligned} \tag{4.5}$$

with $\alpha, \beta = x, y, z$.

The first term in eq. 4.3, depending on the local density $\hat{\rho}$, defines a simple equation of state, penalizing the density fluctuations in the system [203, 204]. The orientation-dependent part is an analog to the phenomenological Landau free energy, associated with tensorial fields $\hat{\boldsymbol{Q}}^{(1)}(\boldsymbol{r})$ and $\hat{\boldsymbol{B}}(\boldsymbol{r})$, in which terms only up to quadratic order have been retained [27, 202].

The definition of the interactions through a functional of local order parameters (collective variables), as defined by eqs. 4.4, allows the conversion of the particle-based description into a field-theoretical one, and vice versa. As already discussed in chs. 2.2 and 3, models can then be efficiently treated within the self-consistent field theory approach or methods that account for fluctuations [30, 205–207]. For the choice $\bar{\mu} = 0$ and $\bar{\lambda} = 0$ one recovers from eq. 4.3 the functional used in ch. 3 for the description of nematic liquid crystalline polymers, i.e. eq. 3.15.

For the general case, eq. 4.3, a transformation similar to that used in ch. 3.3.2 is now applied [29, 32, 34], in order to arrive at a pairwise potential. Therefore, the locally defined quantities $\hat{\rho}$, $\hat{\boldsymbol{Q}}^{(1)}$ and $\hat{\boldsymbol{B}}$ in eq. 4.3 are substituted with the averaged quantities $\hat{\Phi}_\omega(\boldsymbol{r})$ (eq. 2.32 from ch. 2.2.1), $\hat{\boldsymbol{Q}}_\omega(\boldsymbol{r})$ (eq. 3.19 from ch. 3.3.2) and

$$\hat{\boldsymbol{B}}_\omega(\boldsymbol{r}) = \int d\boldsymbol{r}'\omega(|\boldsymbol{r} - \boldsymbol{r}'|)\hat{\boldsymbol{B}}(\boldsymbol{r}'), \tag{4.6}$$

in order to obtain the Hamiltonian as a sum of pairwise interactions,

$$H_{\text{nb}} = \frac{1}{2}\sum_{i=1}^{n}\sum_{s=1}^{N}\sum_{j=1}^{n}\sum_{t=1}^{N}\left[\frac{1}{\rho_0}\int d\boldsymbol{r}\omega(|\boldsymbol{r} - \boldsymbol{r}_i(s)|)\omega(|\boldsymbol{r} - \boldsymbol{r}_j(t)|)\right]$$
$$\times\left[\bar{\kappa} - \frac{2\bar{\nu}}{3}\boldsymbol{q}_i^{(1)}(s) : \boldsymbol{q}_j^{(1)}(t) - \frac{2\bar{\mu}}{3}\left(\boldsymbol{q}_i^{(1)}(s) : \boldsymbol{b}_j(t) + \boldsymbol{b}_i(s) : \boldsymbol{q}_j^{(1)}(t)\right) - \frac{\bar{\lambda}}{2}\boldsymbol{b}_i(s) : \boldsymbol{b}_j(t)\right]. \tag{4.7}$$

In this expression, the choice of the weight function ω is yet not explicit. The orientation dependent part of eq. 4.7 can be casted into the form of the biaxial interaction potential proposed by Straley [201], if the definitions of the molecular axes are substituted explicitly. The resulting form emphasizes the fact that the potential is a direct generalization of the Meier-Saupe potential for molecules with biaxial symmetry [200, 201].

Defining the weight function ω with eq. 3.21, the non-bonded potential between sites s and t in the i-th and j-th chain, respectively, has the following form [27, 201, 202, 208]:

$$
\begin{aligned}
V_{\mathrm{nb}} = u(r_{ij}(s,t)) \Bigg[\bar{\kappa} - \frac{2\bar{\nu}}{3} \boldsymbol{q}_i^{(1)}(s) : \boldsymbol{q}_j^{(1)}(t) - \\
- \frac{2\bar{\mu}}{3} \left(\boldsymbol{q}_i^{(1)}(s) : \boldsymbol{b}_j(t) + \boldsymbol{b}_i(s) : \boldsymbol{q}_j^{(1)}(t) \right) - \frac{\bar{\lambda}}{2} \boldsymbol{b}_i(s) : \boldsymbol{b}_j(t) \Bigg],
\end{aligned}
\tag{4.8}
$$

with $r_{ij}(s,t) = |\boldsymbol{r}_i(s) - \boldsymbol{r}_j(t)|$. The isotropic part of the interaction is set by $u(r_{ij}(s,t))$ (eq. 3.22, compare also Ref. [34]) and $\bar{\kappa}$ controls the compressibility of the system. In order to fix the sphere diameter, $d = 2\sigma$, which determines the interaction range, it is noted that conjugated backbones start to repel each other when their side chains overlap. It is therefore set $\sigma = 0.6\,\mathrm{nm}$, which is close to the length of a hexyl chain in the all-trans configuration, $\sim 0.76\,\mathrm{nm}$ (note that $\sigma = 0.6\,\mathrm{nm}$ is smaller than the value used for the uniaxial-nematic model in ch. 3). An explicit dependence of the potential $u(r_{ij}(s,t))$ on a reference density ρ_0 is retained, although it could have been incorporated into the coefficients of eq. 4.8. In fact, this emphasizes the link to the functional-based field-theoretical descriptions of polymeric liquid crystals [121, 122, 124, 209]. For the simulations, the reference density is chosen to be the bulk number density of P3HT repeat units, $\sim 4\,\mathrm{hexylthiophenes/nm^3}$, which is estimated from the P3HT molar volume of $151\,\mathrm{cm^3/mol}$ [177] similar to the choice in ch. 3.3.2.

With the definition of molecular tensors eqs. 4.5, the $\bar{\nu}$-dependent term in eq. 4.8, corresponding to the double dot product (see ch. 3.3.2) of $\boldsymbol{q}_i^{(1)}(s)$ and $\boldsymbol{q}_j^{(1)}(t)$, promotes a rod-like nematic alignment, where on average $\boldsymbol{n}_i^{(1)}(s) \parallel \boldsymbol{n}_j^{(1)}(t)$ (see Fig. 4.5). The term defined by the product of $\boldsymbol{b}_i(s)$ and $\boldsymbol{b}_j(t)$ facilitates biaxial ordering, where on average $\boldsymbol{n}_i^{(2)}(s) \parallel \boldsymbol{n}_j^{(2)}(t)$ and $\boldsymbol{n}_i^{(3)}(s) \parallel \boldsymbol{n}_j^{(3)}(t)$. Finally, the $\bar{\mu}$-dependent term favors on average the orthogonal orientation of hexylthiophene units, i.e., $\boldsymbol{n}_i^{(1)}(s) \perp \boldsymbol{n}_j^{(1)}(t)$ and $\boldsymbol{n}_i^{(2)}(s) \perp \boldsymbol{n}_j^{(2)}(t)$. In this study, such orientation of mesogenes will be considered unphysical and

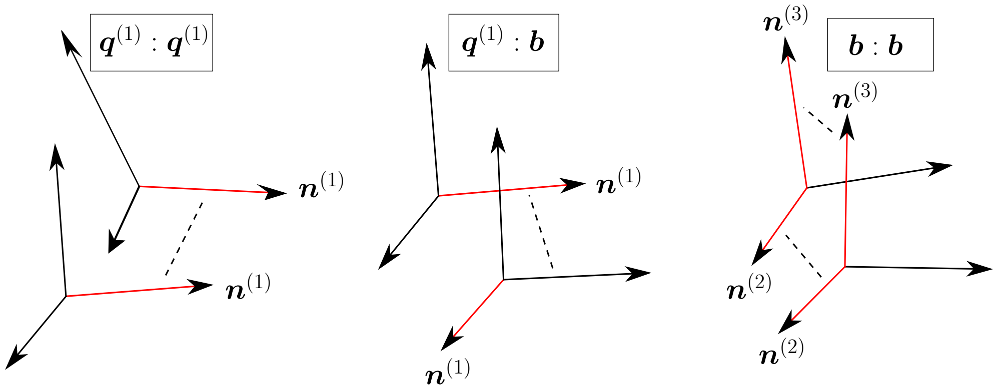

Figure 4.5: Scheme, illustrating the interpretation of the coupling terms in eq. 4.8. See main text for a detailed explanation.

is set in the following to zero, $\bar{\mu} = 0$. If sites s and t are located on the same chain, and $|s - t| \leq 3$, their non-bonded interactions are fully set to zero, otherwise they interact with the potential defined in eq. 4.8.

As to conclude this section, it is noted that the presence of the distance dependent soft core $u(r_{ij}(s,t))$ renders the interaction potential eq. 4.8 different from the one originally introduced by Straley [201]. In his work, the non-bonded potential was obtained from the excluded volume of two rectangular blocks at selected relative orientations. The distance dependence was averaged out at the first step of a mean field treatment. The interaction parameters in the potential can be connected (approximately) to the length, breadth and width of the rectangular blocks [201].

The directional interactions of eq. 4.8 can be considered as a simple case of defining a coarse-grained potential by keeping a few terms in a general expansion into a product basis of Wigner matrices [28, 210, 211]. Generally, the coefficients in such an expansion are functions of intermolecular distances. The model introduced in this study approximates the dependence by a single function $u(r_{ij}(s,t))$.

Setting the interaction strength

Obtaining physically adequate thermodynamic behavior of the system imposes constraints on $\bar{\kappa}$, $\bar{\nu}$, $\bar{\mu}$, and $\bar{\lambda}$. As it has been already mentioned above, $\bar{\mu} = 0$ is always set, and two limiting cases in $\bar{\nu}$, $\bar{\lambda}$-parameter space are considered. Namely, when $\bar{\nu} = 0$ and $\bar{\lambda}$ is larger than a critical value (details will be given in the following), biaxial-nematic mesophases are obtained. When exploring the properties of such mesophases related to charge transport (e.g., density of states) it is important to ensure that the same parameterization leads to biaxial nematic ordering for all considered molecular weights and temperatures. For this purpose, the magnitude of $\bar{\lambda}$ required to induce biaxial ordering, which decreases with chain length (see ch. 4.5.1 for details), has to be considered. Therefore, the LC behavior of the shortest polymer with $N = 8$ is initially explored for the highest temperature of interest, $T_0 = 500\,\mathrm{K}$, and the value for $\bar{\lambda}$ is chosen on the order of a few $k_{\mathrm{B}}T_0$, for which biaxial-nematic ordering is observed. This choice of $\bar{\lambda}$ is sufficient to induce biaxial-nematic ordering for the remaining combinations of chain lengths and temperatures considered in the simulations. The opposite case, setting $\bar{\lambda} = 0$, is also addressed, in which for sufficiently large $\bar{\nu}$, mesophases with "rod-like" nematic alignment are obtained.

The restrictions on $\bar{\kappa}$ can be obtained from the simple mean field estimation of the isothermal compressibility, κ_T (see appendix ch. 1), in the case of perfect biaxial ordering,

$$\frac{1}{\kappa_T} = \frac{k_{\mathrm{B}}T\rho_0}{N} + \left(\bar{\kappa} - \bar{\nu} - \bar{\lambda}\right)\rho_0. \tag{4.9}$$

Within the range of coupling parameters considered in the simulations, $\bar{\kappa} = 6k_{\mathrm{B}}T_0$ is always employed, in order to ensure a positive compressibility [69].

At the same time, for this choice,

$$\bar{\kappa}u(0) = 6\bar{\kappa}/8\pi\rho_0\sigma^3 \approx 1.65k_\mathrm{B}T_0, \tag{4.10}$$

that is, the interactions remain soft, i.e. on the scale of $k_\mathrm{B}T$, if segments substantially overlap. This is a result of the substantial degree of coarse-graining employed in the current model, while preserving the number density of hexylthiophene units of the real material. Indeed, the coarse-grained hexylthiophenes interact already at distances $2\sigma = 1.2\,\mathrm{nm}$, which is almost two times larger than the average distance of their centers estimated from the mean density as $\rho_0^{-1/3} \approx 0.63\,\mathrm{nm}$. In this scope, using a larger $\bar{\kappa}$ would result into a model with unrealistically large excluded volumes. A more general discussion of the effects of compressibility on packing of largely coarse-grained units can be found in Ref. [32] (compare also with the discussions in ch. 3.3).

4.4 Systems studied and simulation details

In the following, P3HT molecules with chain lengths $N = 8$, 16 and 32 will be considered, placed in a cubic simulation cell with fixed volume V and temperature T. The number of chains n in the simulation box is defined in a way that the average density of particles corresponds to the reference density of P3HT, i.e. $nN/V \approx 4\,\mathrm{hexylthiophenes/nm}^3$. The configuration space of these systems is sampled using a Monte Carlo approach. The scheme is based on the standard reptation algorithm [212–215], adopted in order to take into account the orientational degrees of freedom of the end-groups of the P3HT chain (see Fig. 4.6).

To propose a new configuration, a chain is randomly selected and one of the two end-groups, together with the attached “ghost” bond, is cut-off and reattached to the opposite end of the molecule (the direction of the reptation is chosen with equal probability for the forward and backward case). The

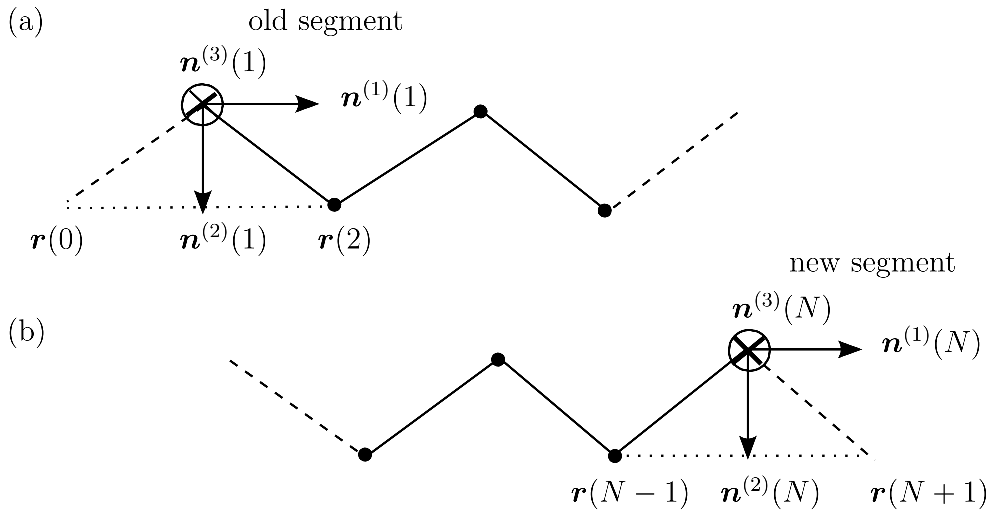

Figure 4.6: Configuration of a P3HT chain (a) prior and (b) after a reptation move. The physical and the “ghost” bonds are drawn with solid and dashed lines, respectively. The orthonormal set of vectors defining the orientation of the hexylthiophene group at the old and the new position is also shown.

reattachment is performed through the “ghost” bond at the corresponding end of the chain (compare sec. 4.3.3), transforming into a physical bond. Subsequently, to specify the orientation of the hexylthiophene at the changed position, new torsional and angular degrees of freedom are chosen for the “ghost” bond which is attached to it. These are drawn according to the Boltzmann weight of the bonded potentials, defined in eqs. 4.1. Simultaneously, at the old position of the group, the physical, connecting bond becomes a ”ghost” bond. The above steps are clarified in Fig. 4.6, showing a P3HT chain before and after a reptation move. Following the standard Metropolis criterion [160], the move is accepted with probability

$$p_{\mathrm{acc}} = \min(1, \exp(-\Delta H_{\mathrm{nb}}/k_{\mathrm{B}}T)), \tag{4.11}$$

with ΔH_{nb} corresponding to the difference in non-bonded energies between the proposed and the old configuration. It is calculated by considering the isotropic and directional interactions (see eq. 4.8) between the displaced group and the surrounding particles at the new and old positions. The interactions are calculated using a linked neighbor-list algorithm [88]. The softness of the interactions enhances significantly the efficiency of the reptation move, e.g., in the biaxial phase the move has an acceptance rate of 20%.

Periodic boundary conditions are employed in all directions. To reduce finite system-size effects, the length of the box edges L is taken to be at least twice as large as the contour length of the polymer. For example, setting $L \approx 26\,\mathrm{nm}$ constitutes a typical choice for the shorter P3HT chains with $N = 8$ and 16. In this case, the modeled systems contain about 7×10^4 coarse-grained hexylthiophene groups. At the same time, the simulations of the longer molecules with $N = 32$ are more demanding: typical systems considered in this case have dimensions $L \approx 51\,\mathrm{nm}$ and consist of approximately 5×10^5 hexylthiophenes.

4.5 Results

4.5.1 Conformational and thermodynamic properties

Amorphous melts

It is instructive to study the model first without the orientation-dependent interactions, i.e. modeling P3HT melts including only the isotropic repulsive part of the potential in eq. 4.8 and $\bar{\kappa} = 6k_{\mathrm{B}}T_0$, while $\bar{\nu} = \bar{\mu} = \bar{\lambda} = 0$. Conformational properties of the P3HT chains can be quantified via the standard single chain structure factor, $S_0(q)$, which can be related to the chain stiffness from a Holtzer plot [216–218]. An example is shown in Fig. 4.7a, demonstrating the $qS_0(q)$ calculated in a melt of P3HT chains with $N = 32$, simulated at $T = 500\,\mathrm{K}$. The wave vector q^*, marking the transition to the plateau, can be used to define a persistence length $l_p = 3.5/q^*$ [216–219] (this definition of l_p, in particular the factor 3.5, is empirically chosen, see Ref. [219]). In order to obtain q^* from the intersection of two straight lines by fitting in a logarithmic plot (see inset in Fig. 4.7a), the decreasing part of $qS_0(q)$ before the plateau is chosen, i.e. the values in the interval $1.21\,\mathrm{nm}^{-1} \leq q \leq 1.58\,\mathrm{nm}^{-1}$, and from the plateau regime itself, i.e., $2.41\,\mathrm{nm}^{-1} \leq q \leq 3.46\,\mathrm{nm}^{-1}$. From Fig. 4.7a, $q^* = 1.77\,\mathrm{nm}^{-1}$ is found, leading to $l_p = 1.98\,\mathrm{nm}$. As it has been discussed in Ref. [218], the choice of the fitting region and of the function approximating the $qS_0(q)$ near the plateau is rather ambiguous and such details will affect the precise values of the extracted l_p. Thus, when comparing simulation results with scattering experiments, it is essential that both employ the same definition of l_p and conventions for its extraction. However, it is noted that the $l_p = 1.98\,\mathrm{nm}$ calculated from the Holtzer plateau is in very good agreement with $l_p = 1.5\,\mathrm{nm} - 2\,\mathrm{nm}$ observed in scattering experiments [150] for P3HT solutions near Θ-solvent conditions at high temperatures ($T \sim 200\,^{\circ}\mathrm{C}$).

Focussing on the bulk properties of the amorphous melt, the compressibility

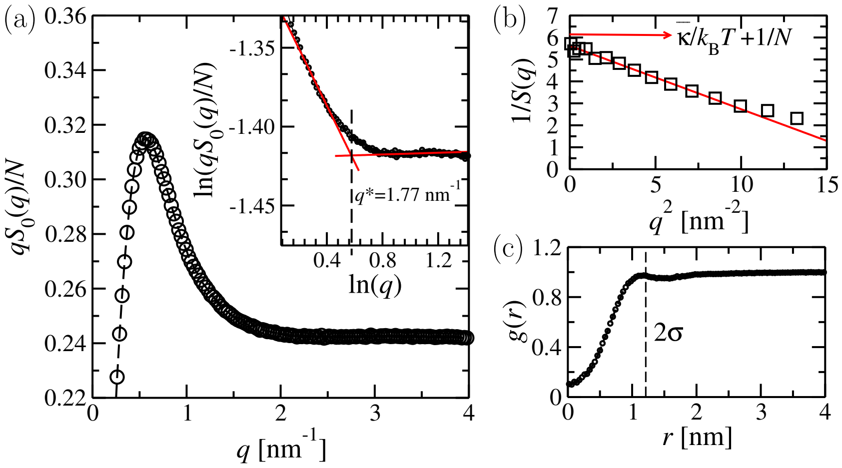

Figure 4.7: (a) Holtzer plot for a melt of P3HT chains with $N = 32$, in which $S_0(q)$ stands for the single chain structure factor and q is the magnitude of the wave vector. The inset shows the region of the transition to the Holtzer plateau in a logarithmic plot and straight red lines correspond to a linear fit of data. (b) Inverse structure factor of density fluctuations, $1/S(q)$, plotted for small wave vectors, calculated from simulations of P3HT melts with $N = 32$. For comparison, the limit $1/S(q \to 0) = (\bar{\kappa}/k_{\mathrm{B}}T) + 1/N$, obtained using the mean field estimation for the isothermal compressibility, is marked by the red arrow. (c) Pair correlation function, $g(r)$, calculated in the same system. The dashed line indicates the distance $1.2\,\mathrm{nm}$, below which segments start interacting. For all calculations, $T = T_0 = 500\,\mathrm{K}$ and $\bar{\kappa} = 6k_{\mathrm{B}}T_0$ were used.

can be estimated from the structure factor, defined as:

$$S(q) = \frac{1}{nN} \left\langle \left| \sum_{i,s}^{n,N} \exp\left(i\boldsymbol{q} \cdot \boldsymbol{r}_i(s)\right) \right|^2 \right\rangle. \tag{4.12}$$

The brackets denote an average over the directions of the wave vector $\boldsymbol{q}$ and the configurations of the system. The isothermal compressibility is obtained

[24] as

$$\rho_0 k_{\mathrm{B}} T k_T = S(q \to 0). \tag{4.13}$$

In Fig. 4.7b, the behavior of $1/S(q)$ as a function of q^2 is demonstrated for small wave vectors. It can be seen that $1/S(q)$ has a linear dependence on q^2. This dependence is highlighted by fitting the data with $q^2 \lesssim 10\,\mathrm{nm}^{-2}$ to a straight line. Interestingly, the compressibility is rather close to the approximate mean field prediction (compare eq. 4.9),

$$1/\rho_0 k_{\mathrm{B}} T k_T = (\bar{\kappa}/k_{\mathrm{B}} T) + 1/N, \tag{4.14}$$

although the experimental densities realized in the simulations are low comparing to the "infinitely high" density limit assumed in the former. This is illustrated in Fig. 4.7c by the radial distribution function $g(r)$, exhibiting a weak but distinct structuring, which contrasts $g(r) = 1$ of the mean field limit [220]. Atomistic simulations of P3HT melts at high temperatures estimate the region of "hard" excluded volume between hexylthiophene groups to be $r \approx 0.5\,\mathrm{nm}$ [185]. Although the excluded volume constraint is relaxed in the simulations, it can be seen that after the first coordination shell, set by the size of the isotropic core 2σ, the $g(r)$ drops substantially to $g(r = 0.5\,\mathrm{nm}) \approx 0.3$. The latter point is important for the re-introduction of atomistic details into the configurations obtained with the soft model, which will be the topic of ch. 5.

Isotropic/biaxial nematic transition

Uniaxial or biaxial nematic ordering of P3HT chains in the system can be identified with uniaxial and biaxial order parameters [28], S and B, which have been used according to the definition presented in Ref. [221]. The parameter S is the standard nematic order parameter, eq. 3.7, defined for the nematic order tensor $\boldsymbol{Q}^{max}$ (the superscript is explained in the following). All details about the definition of the biaxial order parameter B, which is straightforward but long however, are rephrased in the appendix ch. 3. Here, only a brief summary is given. Following the Refs. [221, 222], the orientation tensors $\mathbf{Q}^{(k)}$ (where $k = 1, 2, 3$), defined as

$$Q^{(k)}_{\alpha\beta} = \frac{1}{nN} \sum_{i,s}^{n,N} q^{(k)}_{i,\alpha\beta}(s) \tag{4.15}$$

are calculated, in which the molecular tensors $\mathbf{q}_i^{(k)}(s)$ have been introduced in eq. 4.5. Subsequently, the nine eigenvalues (three for each tensor) are determined and the maximum *absolute* eigenvalue $\lambda_{\max}$ is identified. The order parameter S, in this language, can be obtained from

$$S = |\boldsymbol{v}^T_{\max} \mathbf{Q}^{\max} \boldsymbol{v}_{\max}|. \tag{4.16}$$

In the above, $\mathbf{Q}^{\max}$ and $\boldsymbol{v}_{\max}$ (with $|\boldsymbol{v}_{\max}| = 1$) stand for the orientation tensor and the eigenvector corresponding to $\lambda_{\max}$. Isotropic phases are characterized by a vanishing S (within corrections for a finite number of particles[223]), while $S > 0$ indicates nematic orientation parallel to $\boldsymbol{v}_{\max}$. Two types of uniaxial nematic ordering are observed in the simulations: a) rod-like, with on average $\boldsymbol{n}_i^{(1)}(s) \parallel \boldsymbol{v}_{\max}$, and b) plate-like, with on average $\boldsymbol{n}_i^{(3)}(s) \parallel \boldsymbol{v}_{\max}$. A representative snapshot of a plate-like nematic mesophase is shown in Fig. 4.8a. With the definition of S used in this approach, the nematic order parameter is always positive (this is different from the definition for a single molecular director used in ch. 3). For plate-like particles, a straightforward way to distinguish between the two uniaxial mesophases is to monitor the sign of the maximum absolute eigenvalue of $\mathbf{Q}^{(1)}$, which will be positive in the first and negative in the second case.

To facilitate the decision if the system shows additional order perpendicular to $\boldsymbol{v}_{\max}$, out of the six eigenvalues of the remaining two orientation tensors, the one with the maximum *positive* value $\lambda_{2,\max}$ is chosen. The orientation

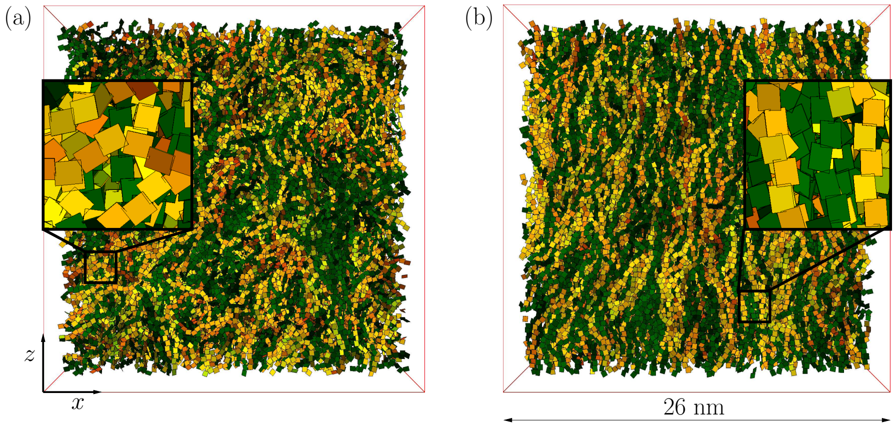

Figure 4.8: Both panels show a snapshot of an equilibrated system containing 2169 molecules with polymerization degree $N = 32$, obtained from simulations started from a pre-stacked configuration. To facilitate visualization, a configuration of a relatively small system with $L \simeq 26\,\mathrm{nm}$ is presented. Colors are arbitrarily chosen to improve the visibility of chain contours. (a) System in a plate-like nematic phase with the coupling strength set to $\bar{\lambda} = 4k_{\mathrm{B}}T_0$ (Order parameters $S = 0.57$, $B = 0.12$). (b) Biaxial-nematic system, obtained at a stronger coupling $\bar{\lambda} = 5.5k_{\mathrm{B}}T_0$ (Order parameters $S = 0.79$, $B = 0.59$). The thiophenes have their $\boldsymbol{n}_i^{(1)}(s)$, $\boldsymbol{n}_i^{(2)}(s)$, and $\boldsymbol{n}_i^{(3)}(s)$ vectors aligned on average along the z, x, and y-directions, respectively. In both cases, $\bar{\nu} = \bar{\mu} = 0$ and $T = T_0 = 500K$.

tensor and the eigenvector associated with this eigenvalue are denoted as $\mathbf{Q}^{\mathrm{2nd}}$ and $\boldsymbol{v}_{2,\mathrm{max}}$, respectively. After projecting [221] $\boldsymbol{v}_{2,\mathrm{max}}$ to the plane perpendicular to $\boldsymbol{v}_{\mathrm{max}}$, one completes the resulting set of directors $\boldsymbol{v}_{\mathrm{max}}$, $\boldsymbol{v}_{2,\mathrm{max}}^{\mathrm{pr}}$ to a right-handed orthonormal system with $\boldsymbol{v}_{3,\mathrm{max}}^{\mathrm{pr}}$ (see appendix ch. 3 for technical details). With the help of the remaining orientation tensor, $\mathbf{Q}^{\mathrm{3rd}}$, the order parameter B is calculated as:

$$\begin{aligned} B = \frac{1}{3} | & \boldsymbol{v}_{2,\max}^{\mathrm{pr,T}} \mathbf{Q}^{\mathrm{2nd}} \boldsymbol{v}_{2,\max}^{\mathrm{pr}} + \boldsymbol{v}_{3,\max}^{\mathrm{pr,T}} \mathbf{Q}^{\mathrm{3rd}} \boldsymbol{v}_{3,\max}^{\mathrm{pr}} \\ & - \boldsymbol{v}_{2,\max}^{\mathrm{pr,T}} \mathbf{Q}^{\mathrm{3rd}} \boldsymbol{v}_{2,\max}^{\mathrm{pr}} - \boldsymbol{v}_{3,\max}^{\mathrm{pr,T}} \mathbf{Q}^{\mathrm{2nd}} \boldsymbol{v}_{3,\max}^{\mathrm{pr}} | \end{aligned} \tag{4.17}$$

B is a measure of biaxial order: it grows only when two independent axes of mesogenes are ordered along the corresponding directors. It vanishes in purely uniaxial phases. A representative snapshot of a biaxial nematic mesophase is shown in Fig. 4.8b.

Fig. 4.9 shows an example plot from which a rough estimate of the location of phase transitions can be obtained, for the example of a $N = 16$ melt for increasing coupling $\bar{\lambda}$. Following this approach systematically, the phase behavior for $T = T_0$ as a function of chain length and orientation coupling $\bar{\lambda}$ is estimated, while keeping, as explained in sec. 4.3.3, $\bar{\nu} = \bar{\mu} = 0$. The results are summarized in Fig. 4.10a, showing the approximate (details follow below) location of the different phases as a function of $\bar{\lambda}$ and inverse polymerization degree, $1/N$. It can be seen, that for all N considered here, the onset of biaxial ordering as a function of $\bar{\lambda}$ occurs in two steps (compare also Fig. 4.9). For moderate coupling strengths, as shown in the example of Fig. 4.9, one observes a change from an isotropic to a plate-like nematic mesophase, characterized by $S \approx 0.5 - 0.8$. Although in the plate-like nematic mesophase the biaxial order parameter B increases slightly, comparing to isotropic systems, it remains small, i.e. $B \leq 0.1$. By increasing $\bar{\lambda}$ further, mesophases with biaxial structuring are obtained, characterized by $B \approx 0.3 - 0.6$. Notably, for the systems considered in the simulations, B is always lower than S and usually shows larger fluctuations. For each N, the phase boundaries have been located by observing spontaneous ordering of the system from a random initial configuration. In this scope, the error bars represent the regimes close to the transition, for which strong fluctuations of S and B did not allow for a definite

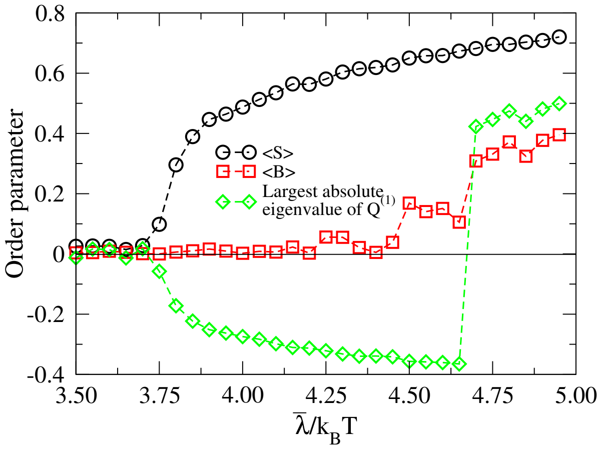

Figure 4.9: Uniaxial and biaxial nematic order parameters, S and B, as a function of the coupling strength λ for a system with chain length $N = 16$. Two visible phase changes can be observed: First, from isotropic to nematic plate-like, indicated by an increase of S, followed by a change to a biaxial-nematic phase, as seen from an increase of B. The transition is not sharp, and the width of the regime for which the order parameters rise steeply is reflected in the error bars plotted in Fig. 4.10. Additionally, the largest absolute eigenvalue of $\boldsymbol{Q}^{(1)}$ is shown, which can be used for distinguishing uniaxial plate-like (negative eigenvalue) and rod-like ordering (positive eigenvalue).

conclusion regarding the state of the system (see Fig. 4.9). For the longest chains, $N = 32$, for which the most significant finite size effects are expected, the phase boundaries were estimated for two different box sizes, $L = 64\,b$ and $L = 128\,b$, yielding the same results within the accuracy of the current study. The same behavior has also been obtained from simulations started from initially pre-ordered systems.

Fig. 4.10a highlights that for longer chains, the biaxial nematic ordering takes place at weaker orientation couplings, as it has already been mentioned in sec. 4.3.3. Similar effects of molecular weight on the onset of LC ordering are observed in the case of uniaxial rod-like mesophases. As an illustration,

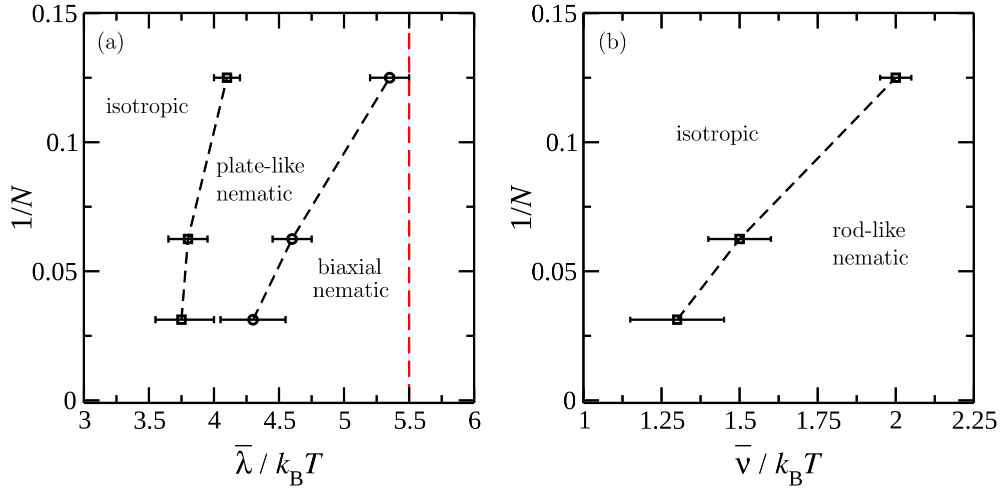

Figure 4.10: (a) Phase behavior as a function of inverse degree of polymerization, $1/N$, and orientation-coupling strength $\bar{\lambda}$ (in units of $k_\mathrm{B}T$), for $\bar{\nu} = \bar{\mu} = 0$. The dashed red line marks the value $\bar{\lambda} = 5.5 k_\mathrm{B}T_0$, used for obtaining morphologies with biaxial structuring. (b) Phase behavior as a function of inverse degree of polymerization, $1/N$, and orientation coupling strength $\bar{\nu}$ (in units of $k_\mathrm{B}T$) for $\bar{\lambda} = \bar{\mu} = 0$. In both cases, the highest temperature $T = T_0 = 500\,\mathrm{K}$ was considered.

Fig. 4.10b demonstrates the phase behavior obtained at $T = T_0$, as a function of chain length and orientation coupling $\bar{\nu}$, while keeping $\bar{\mu} = \bar{\lambda} = 0$. This result agrees with earlier simulations of rod-like nematic phases of P3HT based on a simpler model [69] and with experimental observations [148]. The latter report that increasing the molecular weight of the polymer shifts the isotropic/nematic transition to higher temperatures, i.e. for longer chains, weaker thermodynamic orientational forces ($\sim \bar{\nu}/k_\mathrm{B}T$) are required to obtain nematic LC ordering.

Elastic properties in nematic phase

In ch. 3, the spatial fluctuations of the nematic director have been considered within a continuum description with the Frank free energy, eq. 3.8. Following this approach, one can readily use the analysis schemes for the more elaborated P3HT model in this chapter. Hence, a set of non-biaxial nematic mesophases (rod-like ordering along the chain backbones) has been generated for a set of different coupling strengths, i.e. $\bar{\nu} = 1.8k_{\mathrm{B}}T_0$, $2k_{\mathrm{B}}T_0$, and $2.5k_{\mathrm{B}}T_0$. $\bar{\mu} = \bar{\lambda} = 0$ has been employed in all cases, and melts of P3HT chains with $N = 32$ were considered at $T = T_0$. Two different box-sizes $L = 64\,b$ and $128\,b$ (corresponding to roughly two and four times the end-to-end distance of a fully stretched P3HT molecule, respectively) were considered to ensure that there were no significant finite system size effects. The MC simulations were started from a perfect biaxial nematic mesophase with all P3HT chains in a *trans* configuration and all thiophene units having their $\boldsymbol{n}_i^{(1)}(s)$ and $\boldsymbol{n}_i^{(3)}(s)$ vectors aligned along the z- and the y-axis of the box, respectively. After relaxation, a rod-like nematic mesophase was obtained. A large number of equilibrated configurations have been analyzed, calculating the Fourier transformation of the local nematic tensor defined through the tensor associated with the primary molecular axis $\boldsymbol{n}^{(1)}$,

$$\hat{Q}^{(1)}_{\alpha\beta}(\boldsymbol{q}) = \frac{1}{\rho_0} \sum_{i=1}^{n} \sum_{s=1}^{N} q^{(1)}_{i,\alpha\beta}(s) \exp\left(i\boldsymbol{q} \cdot \boldsymbol{r}_i(s)\right). \tag{4.18}$$

The three Frank elastic constants with respect to splay, twist and bend, i.e. K_1, K_2 and K_3 have subsequently been extracted from fitting the fluctuation spectra eqs. 3.36 with constant K_1, i.e. the form of the spectra similar to that of small mesogene scattering, to the simulation data in the low wave length regime. Wave vectors $q_\alpha = 2\pi m_\alpha / L$ with $-4 \leq m_\alpha \leq 4$ have been taken into account for the analysis. For a detailed discussion it is referred to ch. 3, in particular chs. 3.1, 3.5 and 3.6.4.

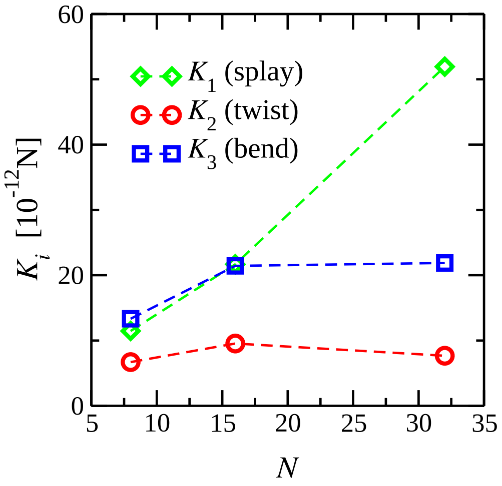

Figure 4.11: Dependence of the three Frank elastic constants on the degree of polymerization, N, in a uniaxial rod-like nematic mesophase. The coupling strength was set to $\bar{\nu} = 2.5 k_{\mathrm{B}} T_0$ and the temperature to $T = T_0 = 500\,\mathrm{K}$.

For $\bar{\nu} = 2.5 k_{\mathrm{B}} T_0$, the values $K_2 = 0.8 \times 10^{-11}\,\mathrm{N}$ and $K_3 = 2.2 \times 10^{-11}\,\mathrm{N}$ have been obtained. For the splay constant, $K_1 = 5.2 \times 10^{-11}\,\mathrm{N}$ is measured from the simulations. The best fit is obtained by assuming that K_1 is independent of q_z in the small wave vector regime. It is noted that the elastic constants remain on the order of $10^{-11}\,\mathrm{N}$ also for the other strengths of nematic coupling, i.e. for $\bar{\nu} = 1.8 k_{\mathrm{B}} T_0$ and $2 k_{\mathrm{B}} T_0$. It is noteworthy that for the largest chain length considered, the magnitudes of the twist and bend constants, K_2 and K_3, are very close to the values obtained in ch. 3 with the model based on a simpler chain representation.

In low molecular weight liquid crystals, the twist and bend elastic constants are typically on the order of $10^{-12}\,\mathrm{N}$ [100]. Experimental measurements in thermotropic main-chain polymer nematics have reported K_2 and K_3 that are either comparable [97, 98] or two orders of magnitude [99] larger. For the soft model, the K_2 and K_3 are on the order of $10^{-11}\,\mathrm{N}$, which fits well into the window of values reported experimentally. The relative magnitude of the two constants observed in the simulations, that is $K_3 > K_2$, agrees with experimental trends [98].

Experiments demonstrate that the splay constant should be one [97, 98] or two [99] orders of magnitude larger than the twist and bend constants. For the rather short chains considered in the simulations, the K_1 is substantially larger than K_2 and K_3, although it is still of the order of 10^{-11} N. It is expected, that in simulations with chains of higher molecular weight the splay constant will significantly increase. To support this statement, the three elastic constants were calculated for systems with $N = 8$, $N = 16$ and $N = 32$ ($\bar{\nu} = 2.5 k_{\mathrm{B}} T_0$) using the same method. The K_1, K_2, and K_3 as a function of polymerization degree are presented in Fig. 4.11, demonstrating that indeed K_1 increases monotonically with N. Modeling longer chains is necessary to determine the form of the functional dependence, which has been investigated with a more simple generic chain model, see ch. 3. For the comparably short chains in this chapter, an initial increase of the twist and bend constants, from the shortest chain length $N = 8$ to longer chains, is observed. Both the twist and the bend constant however saturate and remain small.

It is briefly mentioned that an extension of the director fluctuation analysis to biaxial-nematic mesophases, with an enlarged set of elastic constants [224], is in principle possible. This is however outside the scope of this study.

4.5.2 Morphology and properties related to charge transport

Molecular conformations and cooperative chain alignment will now be linked to properties relevant to charge transport in the material. The results presented in this section stem from a collaboration with Carl Poelking and Denis Andrienko. More details of the charge transfer related calculations can be found in the publication this chapter is based on, see Ref. [1].

As already outlined in the introduction to this chapter, charge transport in partially ordered organic semiconductors can be described as a sum of intra and inter-chain contributions [174]. Charges are typically localized on molecules, while within the molecule, they might delocalize due to π-conjugation. For polymers, i.e., large molecules which introduce long-rang correlations in the material due to chain connectivity, charge delocalization is restricted to conjugated sub-segments. The morphology, in these terms, is a heterogenous distribution of such conjugated segments, and charge transfer can be essentially described as a series of hopping events between localized states. The mobility of charges depends sensitively on the “ruggedness” of site distributions, i.e. the energetic landscape [225–227].

For polymer chains, structural defects such as backbone twists break the conjugation between adjacent monomers and chains exhibit partitioning into conjugated segments [228]. The segment lengths are thus statistically distributed, broadening the distribution of site energies that contribute to the overall density-of-states (DOS). The broadening is intimately linked to the micro- *and* mesoscale morphology of a partially ordered system [229]. In computer simulations, accounting for both short and long-range correlations is challenging.

Evaluation of the *external* contribution to the site energies, which accounts for electrostatic and induction interactions between segments [230], requires the substitution of the atomistic detail back into the soft CG morphologies. For the CG morphologies described in this thesis, such a re-insertion of atomistic details has been addressed and will be presented in ch. 5. Before proceeding with refining the morphologies, here, to a first approximation, intermolecular contribution to the DOS are neglected. Hence, the variation of energy levels due to a change in conjugation length dominates in this case the width of the density of states. With the soft CG morphologies at hand, the internal contribution to the DOS, spatial correlations of site energies, and the temperature dependence can be evaluated.

For this purpose, $\bar{\nu} = \bar{\mu} = 0$ and $\bar{\lambda} = 5.5 k_{\mathrm{B}} T_0$ are chosen, i.e., a set of parameters well inside the biaxial phase is selected (see Fig. 4.10a) for all considered chain lengths. In a limited number of cases, for the two longest chains $N = 16$ and $N = 32$, a weaker coupling strength $\bar{\lambda} = 5 k_{\mathrm{B}} T_0$ has been considered, in order to increase sensitivity to temperature changes. A representative snapshot of an equilibrated system used for calculating properties related to charge-transport is shown in Fig. 4.8b.

Distribution of conjugation lengths

Distributions of conjugation lengths in the isotropic and biaxial nematic phases are first evaluated as a function of length and temperature. To partition a chain into conjugated segments, an identification based on the dihedral angle between two successive monomers is employed: If this angle deviates from the planar *cis* and *trans* conformations by more than $\pm 45°$, the conjugation is assumed to be broken across the monomer-monomer bond [231]. The conjugation length is then the number of monomers l that are part of this conjugated segment. Fig. 4.12c is a qualitative illustration of such a chain partitioning. By analyzing a large number of Monte Carlo snapshots of systems with different ordering and molecular weights, the number density $\rho_s(l, N)$ is obtained, that is, the number of conjugated segments of length l per unit volume. These number densities are shown in Fig. 4.12a for both isotropic and biaxial melts.

The functional dependence of ρ_s on l for different molecular weights can be understood with a simple analytical estimation. Therefore, a probability p of preserving the conjugation across a monomer-monomer bond is introduced, in a way that $p = 0$ implies N conjugated segments in each chain, while $p = 1$ corresponds to one conjugated segment of length N (i.e., the entire chain is conjugated). The probability to find a conjugated segment of length l *inside* a chain of length N is proportional to the probability of finding $l - 1$ conjugated bonds, p^{l-1}, and two broken conjugations, $(1 - p)^2$, weighted by the number

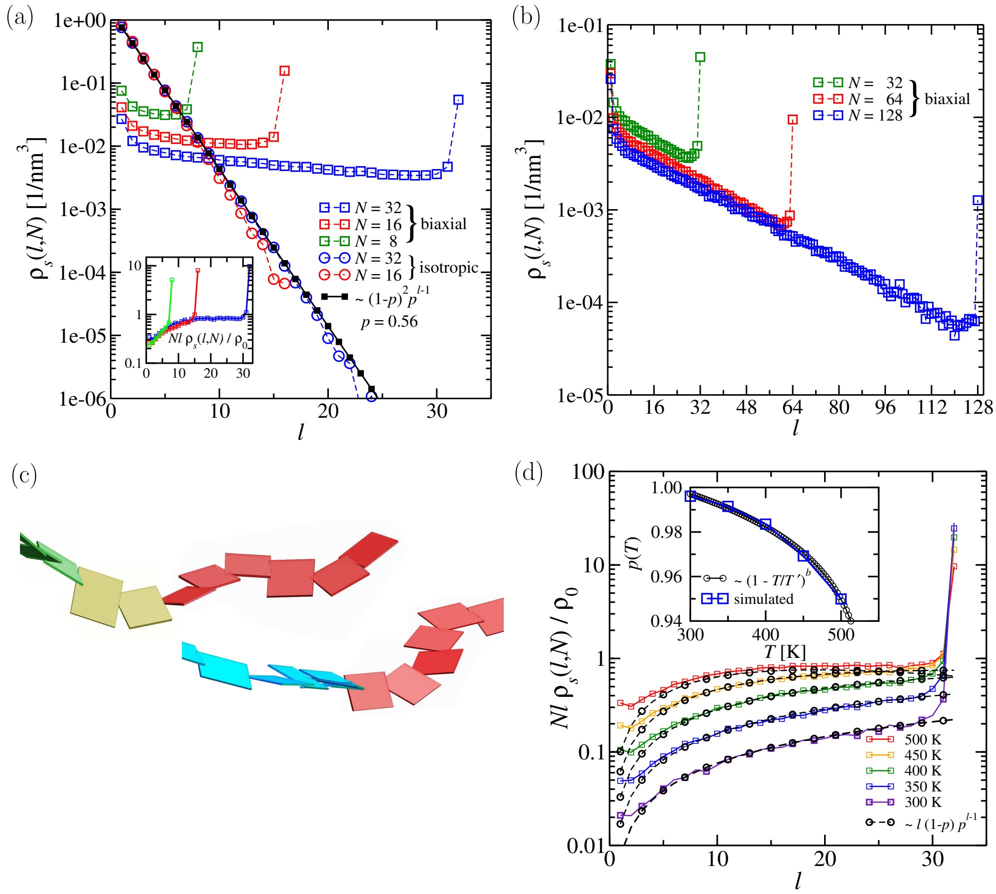

Figure 4.12: (a) Volume number density $\rho_s(l, N)$ of conjugated segments of length l and fit to eq. 4.19 in the limit $l \ll N$. Inset: Volume density ratio of monomers belonging to a conjugated segment of length l divided by the density of chains in the system, ρ_0/N. $\bar{\lambda} = 5.5 k_\mathrm{B} T_0$ and $T = T_0 = 500\,\mathrm{K}$. (b) Distribution of l, calculated for long chains interacting with a constant background field, dominated by short conjugated segments for large N. (c) Qualitative illustration of the partitioning of chains into conjugated segments. Different colors label different l. (d) Temperature dependence of the partial density of monomers in the range from 300 K to 500 K, with $N = 32$ and $\bar{\lambda} = 5 k_\mathrm{B} T_0$. The defect density has been fit to eq. 4.19 in the limit of $p \to 1$ via the bond conjugation probability p. Inset: Dependence of p on the temperature. For $N = 16$, p, as well as its temperature dependence, is identical to the case of $N = 32$.

of possible placements of a segment of length l along a chain of length N, $(N - l - 1)$. Similarly, the probability of finding a conjugated segment of length l at the chain ends is proportional to $2(1-p)p^{l-1}$. Hence, the number density of segments of length l, $\rho_s(l)$, reads

$$\frac{\rho_s(l)}{\rho_0} \simeq \left[\left(1 - \frac{l+1}{N}\right)(1-p)^2 + \frac{2}{N}(1-p) \right] p^{l-1}, \tag{4.19}$$

where ρ_0 is the average number density of the thiophene monomers in the system. The derivation of eq. 4.19 ignores intra-chain torsional correlations. Hence, it is distinguished between "internal" and "tail" segments whereas the constraint that the lengths of all conjugated segments in a chain should add up to N is ignored. Such a constraint may be taken into account [232], but for a qualitative description, eq. 4.19 suffices.

Considering the conjugation criterion of ±45° and assuming that in the isotropic mesophase all torsional degrees of freedom are independently and canonically sampled, one can estimate p as

$$p = 1 - 2Z^{-1} \int_{\pi/4}^{3\pi/4} \exp(-V_\phi/kT)\, d\phi, \tag{4.20}$$

with

$$Z = \int_0^{2\pi} \exp(-V_\phi/kT)\, d\phi. \tag{4.21}$$

The resulting $p = 0.58$ gives rise to a substantial population of short "internal" segments and end-effects become insignificant, i.e., the limit of the infinitely long chain is applicable. In this case ($l \ll N$, $(1-p) \gg 2/N$), eq. 4.19 yields

$$\rho_s/\rho_0 \sim (1-p)^2 p^{l-1}, \tag{4.22}$$

i.e., $\ln \rho_s$ scales as $l - 1$ and is independent of N as observed in Fig. 4.12a. The probability $p = 0.56$, extracted from the fit in Fig. 4.12a, is very close to the initial estimate.

In a biaxial-nematic mesophase, polymer backbones are planar and $p \sim 1$. The conjugated segments are long and, for relatively short polymers, end-effects lead to a chain-length dependent ρ_s, as shown in Fig. 4.12a. Eq. 4.19 in the limit of $(1-p) \ll 2/N$ predicts

$$\rho_s/\rho_0 \sim (1/N)(1-p)p^{l-1}. \tag{4.23}$$

Plotting the ratio $Nl\rho_s/\rho_0$ versus l, it is verified that the condition $(1-p) \ll 2/N$ is fulfilled for the generated morphologies. The inset of Fig. 4.12a shows the collapse of all distributions on a single master curve. For longer chains, however, one may find that $2/N \ll (1-p)$, and ρ_s may be dominated by contributions from "internal" conjugated segments, as in the isotropic mesophase. For the system at $400\,\mathrm{K}$, in which $p = 0.98$ (see the inset of Fig. 4.12d), this should be observed for chains with $N \gg 100$, which is well beyond the chain lengths studied in this thesis. However, to a first approximation, one can study the conjugation length distributions from a sampling of longer chains which are biaxially coupled to a constant background field, i.e. from a simple mean-field consideration. Fig. 4.12b shows the conjugation length distributions obtained for such calculations. Indeed, as expected for long chains [232], the distributions are dominated by relatively short conjugated segments.

The bond conjugation probability p can, to some extent, serve as an order parameter for chain conjugation: As shown in Fig. 4.12d, starting at low temperatures and strong biaxial order, p decreases upon increasing temperature. The T-dependence of p is shown in the inset of Fig. 4.12d, together with a fit to a power-law dependence

$$p(T) = p_0 + a\left(1 - T/T'\right)^b, \tag{4.24}$$

with $b \simeq 0.06$, $a \simeq 0.5$, and $T' = 540\,\mathrm{K}$.

Position of a segment in a chain

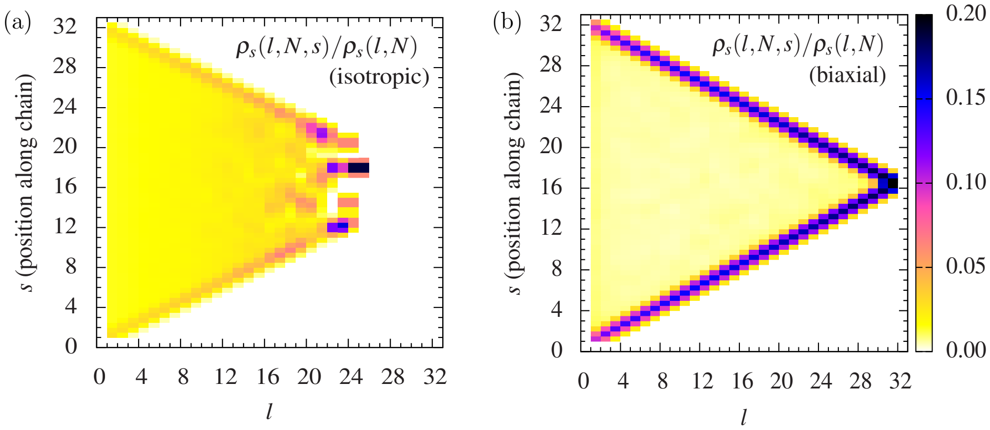

Figure 4.13: Partial density $\rho_s(l, N, s)$ of segments with conjugation length l at position s in the chain, normalized by the integrated segment density $\rho_s(l, N)$, for the (a) isotropic and (b) biaxial morphologies. The plots highlight how conjugation defects tend to localize near the terminal monomers in the case of biaxial nematic order, as opposed to a homogeneous along-the-chain defect distribution for isotropic systems. The data were obtained for $N = 32$ at $\bar{\lambda} = 5.5 k_{\mathrm{B}} T_0$ and $T = T_0 = 500\,\mathrm{K}$.

As discussed above for the biaxial mesophases, the distribution of conjugation lengths (for $l \neq N$) is well described by a model accounting only for the segments at the chain ends. One can therefore conclude that for the lengths of chains considered here, there will be an increased concentration of torsional defects towards the *terminal monomers*. The situation is very different in isotropic melts, where, due to the large number of "internal" conjugated segments, the defects are distributed more homogeneously along the backbone. This is illustrated in Fig. 4.13, with the density ratio $\rho_s(l, N, s)/\rho_s(l, N)$, i.e., the probability for the center of a conjugated segment of length l to be at a position s along the chain, shown for isotropic and biaxial morphologies, respectively. For short polymers, the reason for defects to concentrate towards the chain ends in the case of biaxial order is intuitively clear: First, creating an isolated (in terms of conjugation) monomer in the middle of a conjugated polymer chain requires two torsional defects instead of just one for terminating thiophenes (compare eq. 4.19). Second, for polythiophenes, a change in the dihedral angle results in a change in chain direction due to the zig-zag molecular architecture of P3HT. This change in direction has a high energetic cost due to the tilting of chain segments away from the mesoscopic director and, hence, increased overlap with neighboring chains.

Density of states

In this section, the discussion is focussed on linking the morphology in terms of polymer backbone statistics to the site energy distribution of charge carriers localized on conjugated segments. The density of conjugated segments can be translated into the energetic density of states (DOS) for holes according to the relation between the conjugation length l and the gas-phase ionization potential (IP, Fig. 4.14a). In order to reflect charge transport conditions, a two-site DOS $P(\Delta E)$ based on pairs of segments is considered. These pairs of conjugated segments are drawn from a monomer-based neighbor-list with cut-off $R_c = 1.0\,\mathrm{nm}$. The energy ΔE entering into the two-site DOS is the site-energy difference between the two participating segments. The associated probability density $P(\Delta E)$ is by definition symmetric about $\Delta E = 0$, see Fig. 4.14b. The advantages of the two-site DOS are twofold: First, it not only takes into account the conventional single-site DOS, but also correlations of the energy landscape (see the next subsection and Refs. [228, 233, 234]). Second, charge transfer rates within Marcus theory only depend on site-energy *differences* ΔE, thus making $P(\Delta E)$ the preferred measure to assess transport conditions.

Before discussing molecular weight, the spectrum structure is analyzed. Note that only the internal contribution to the site energies are considered,

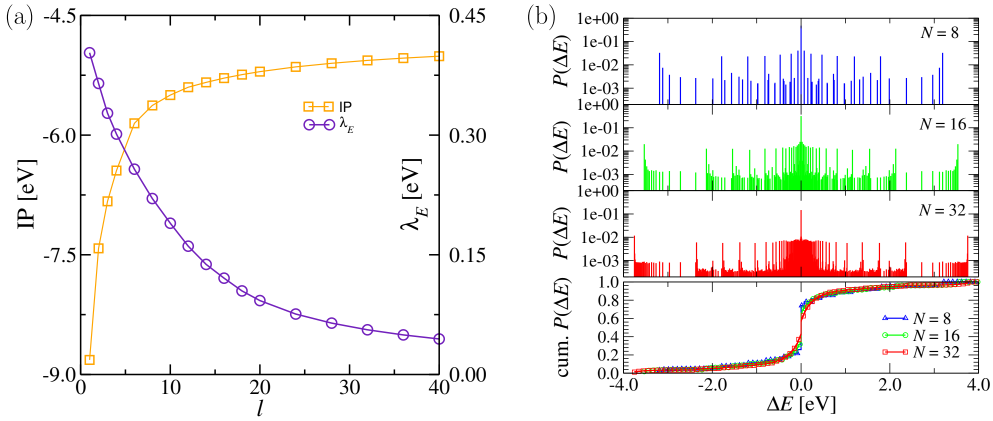

Figure 4.14: (a) Gas-phase ionization potentials and charge-transfer reorganization energies for different conjugation lengths l, obtained using electron density functional theory (DFT). The DFT calculations were performed by Carl Poelking. For details, see the original Ref. [1], which this chapter is based on, and Ref. [228] for calculation details. (b) Top three panels: discrete pair-energy distributions for biaxial systems with chain lengths $N = 8$, $N = 16$ and $N = 32$, calculated from a particle-based neighbor-list with cut-off $1.0\,\mathrm{nm}$. Bottom panel: cumulative pair-energy distribution. Increasing molecular weight leads to a stronger fragmentation of energy levels, yet the shape of the cumulative distribution is unaffected by the chain-length increase. The data were obtained for $\bar{\lambda} = 5.5 k_\mathrm{B} T_0$ and $T = T_0 = 500\,\mathrm{K}$.

hence the pair-energy distribution features delta-peaks at characteristic energy level separations. For all molecular weights, the spike at $\Delta E = 0$ with $P > 0.1$ is by far the most pronounced (note the semi-logarithmic scale in Fig. 4.14b), as is a result of the strong biaxial nematic order in these systems, with a large fraction of the chains in their fully conjugated configuration.

Next, there is a number of peaks of intensity $P \sim 0.01$ distributed over a very wide energy range $0\,\mathrm{eV} < |\Delta E| < 4\,\mathrm{eV}$: These are related to hopping pairs formed between a fully conjugated chain ($l = N$) and a conjugated subunit ($l < N$). The peaks that can be allocated to pairs of this nature are all located around the same density level, $P \sim 0.01$. Hence, located on a fully-conjugated chain, a hole encounters mostly neighboring segments with $l = N$, and then, with a reduced but constant probability, a set of partially conjugated hopping destinations with delocalization length l anywhere from 1 to $N - 1$. This can be related back to the density of segments $\rho_s(l, N)$, which exhibits a broad plateau when reweighted according to the volume, as in $l\rho_s(l, N)$.

Finally, a third type of pairs, with a probability density of $P \sim 0.001$ and pair energies again spread over the whole spectrum, is associated with neighbors formed between two conjugated sub-units of length $l < N$. These pairs are, however, sparse, and their effect on transport is expected to be small.

If the chain length is increased from $N = 8$ to $N = 32$, more and more energy levels are introduced to the system. Yet, the *cumulative* two-site DOS, $\int_{-\infty}^{\Delta E} P(E)dE$, illustrates that the overall distribution remains almost unchanged: The largest differences occur towards the center ($\Delta E = 0$) of the distribution (where the introduction of more energy levels for higher molecular weights broadens the DOS), and at the periphery (where the distribution extends to larger $|\Delta E|$ due to longer available conjugation lengths). Within the range of molecular weights studied here, the dependence of transport on chain length is indeed small, as previously suggested by experiments [235].

Spatial correlations

Site energies in amorphous organic semiconductors are often spatially correlated, because of the long-range nature of electrostatic interactions [229]. For polymers, the internal contributions to the density-of-states may well be spatially correlated, due to long-range orientational ordering. Additionally, one may think of an anticorrelation due to the finite length of the polymer chain, since conjugated segment lengths cannot be distributed arbitrarily along the backbone.

Fig. 4.15a shows a contour plot of the local average conjugation length,

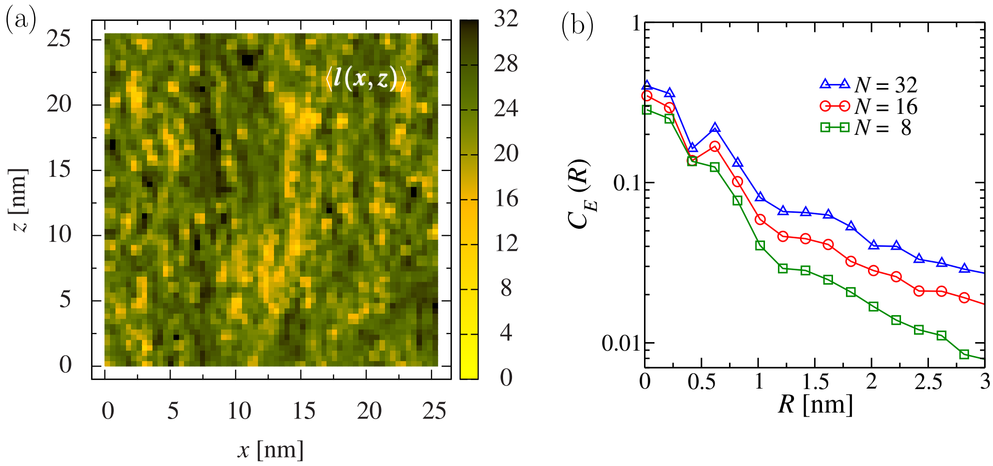

Figure 4.15: (a) Contour plot of the local average conjugation length, $\langle l(x,z)\rangle$, where averaging occurs over a $5\,\mathrm{nm}$ slice in the y-direction and $0.16\,\mathrm{nm}^2$ bins in the x-z plane. The thiophenes have their $\boldsymbol{n}_i^{(1)}(s)$, $\boldsymbol{n}_i^{(2)}(s)$, and $\boldsymbol{n}_i^{(3)}(s)$ vectors aligned on average along the z, x, and y-directions, respectively (i.e., the backbones are oriented with their longest axis along z, compare Fig. 4.8b). (b) Spatial internal site-energy correlation function for biaxial ordering. The data were obtained at $\bar{\lambda} = 5.5 k_\mathrm{B} T_0$ and $T = T_0 = 500\,\mathrm{K}$ (Order parameters $S = 0.79$, $B = 0.59$).

which is obtained from a $5\,\mathrm{nm}$ thick slice, averaged over the y-direction, and a fine binning in the x-z-plane. Long-range inhomogeneities are clearly visible. In order to quantify these effects, the spatial correlation function $C_E(R)$ of internal site energies is calculated,

$$C_E(R) = \frac{\langle (E_i - \langle E\rangle)(E_j - \langle E\rangle)\rangle_{r_{ij}=R}}{\sigma_E^2}, \tag{4.25}$$

with $\langle E\rangle$ being the average and σ_E^2 the variance of the site-energy distribution. Averaging occurs over all pairs (i,j) of conjugated segments of smallest distance of approach r_{ij} with $R \le r_{ij} \le R + \mathrm{d}R$. This correlation function is shown for biaxial phases in Fig. 4.15b. Note that the dip at $0.4\,\mathrm{nm}$, corresponding to the bond length between successive monomers of the same chain, points to a negative intra-chain correlation of site energies, as is expected due to the finite length of the chain. Interestingly, only by taking the internal contribution to the site energies into account, the energetic landscape is weakly and positively correlated over a range of $1.2\,\mathrm{nm}$, with a tail as far down as $3\,\mathrm{nm}$. The correlation becomes more pronounced as N increases and can be traced back to the coexistence of ordered and disordered regions in the morphology as illustrated by Fig. 4.15a (dark and light "patches", with the color code indicating the local average conjugation length). In ch. 5, the correlation of the energetic landscape will be discussed for atomistically resolved morphologies, i.e. after having refined the local structure of the samples.

4.6 Outlook: Modeling multi-component systems

In this short outlook, first steps towards the extension of the model, in order to describe P3HT:PCBM blends, are discussed. The approach is discussed for the most simple polymer model exhibiting nematic orientation without biaxial coupling, namely the model which was introduced in ch. 3. The blend of a polymer, which tends to align nematically, and a fullerene-type molecule, which is approximated as a spherical object, can be described by the following functional:

$$\begin{aligned} H_{\mathrm{nb}} =& \frac{\kappa\rho_0^*}{2}\int\left((1-\alpha)\frac{\hat{\rho}_{\mathrm{P3HT}}(\boldsymbol{r})}{\rho_0^*}+(1+\alpha)\frac{\hat{\rho}_{\mathrm{PCBM}}(\boldsymbol{r})}{\rho_0^*}-1\right)^2 d\boldsymbol{r} \\ &+\frac{\chi\rho_0^*}{2}\int\frac{\hat{\rho}_{\mathrm{P3HT}}(\boldsymbol{r})}{\rho_0^*}\frac{\hat{\rho}_{\mathrm{PCBM}}(\boldsymbol{r})}{\rho_0^*}d\boldsymbol{r}-\frac{\nu\rho_{\mathrm{P3HT}}}{3}\int\hat{\boldsymbol{Q}}(\boldsymbol{r}):\hat{\boldsymbol{Q}}(\boldsymbol{r})d\boldsymbol{r}. \end{aligned} \tag{4.26}$$

Considering the last term in this expression, the notation from earlier chapters was adopted. However, as a new feature, two different species were introduced, namely P3HT monomers and PCBM molecules, with local densities $\hat{\rho}_{\mathrm{P3HT}}$ and $\hat{\rho}_{\mathrm{PCBM}}$, respectively. The parameter χ controls the interaction between different species, with a positive value introducing a repulsion between the latter. The parameter κ is, as in the approaches in earlier chapters, a phenomenological constant that sets the repulsion strength in the pure phases. Nevertheless, the parameter ρ_0^* in eq. 4.26 is a reference number density, which can be approximated by the arithmetic mean of the number densities of the pure phases, $\rho_0^* = \frac{1}{2}(\rho_0^{\mathrm{P3HT}} + \rho_0^{\mathrm{PCBM}})$. α, in this notation, accounts for the difference in the molar volume of the two species. Irrespective of this notation, the part of eq. 4.26 that depends on the local segment densities is the analog to a standard Flory-Huggins description of a two-component mixture [17, 78, 79]. The functional, eq. 4.26, is transformed into pairwise potentials, different for each possible combination of P3HT and PCBM particles, similar to the approach in ch. 3. Here, different density distributions (clouds) for different species introduce additional free parameters to the model. In this way, the model can account for a more pronounced structuring of PCBM particles when the density cloud is chosen with a significantly smaller radius than in the previous approaches. In the simulations, both the value of the χ-parameter, as well as the specific choice of density cloud, affects the phase behavior significantly. The interplay of collective molecular ordering of polymer segments, the local packing in the pure phases in the model, and the resulting effect on the phase separation may be seen as a generic analog for the cooperative behavior of crystallization effects and phase separation of the real blend.

The radii of the density clouds were fixed to $\sigma_{\mathrm{P3HT}} = 0.79\,\mathrm{nm}$ and $\sigma_{\mathrm{PCBM}} = 0.55\,\mathrm{nm}$. The value for the PCBM radius is determined empirically, guided by the radius at which particles start overlapping in a system with the experimentally reported density of the pure PCBM phase. Similar to the evaluation of pairwise potentials through the density cloud approach in the previous chapters (compare eq. 3.22), the transformation of the coupling term in eq. 4.26 with respect to P3HT-PCBM interaction reduces to the solution of an overlap integral,

$$\frac{1}{\rho_0^*}\int d\boldsymbol{r}\,\omega_{\mathrm{P3HT}}(|\boldsymbol{r}-\boldsymbol{r}_i^{\mathrm{P3HT}}(s)|)\,\omega_{\mathrm{PCBM}}(|\boldsymbol{r}-\boldsymbol{r}_j^{\mathrm{PCBM}}|), \tag{4.27}$$

with density clouds of different radii for coarse-grained P3HT segments and PCBM particles,

$$\begin{aligned}\omega_{\mathrm{P3HT}}(r) &= 3/4\pi\sigma_{\mathrm{P3HT}}^3 \text{ for } r < 2\sigma_{\mathrm{P3HT}},\\ \omega_{\mathrm{PCBM}}(r) &= 3/4\pi\sigma_{\mathrm{PCBM}}^3 \text{ for } r < 2\sigma_{\mathrm{PCBM}},\end{aligned} \tag{4.28}$$

and both equal to zero outside the specified range. In this expressions, r denotes the distance from the respective coarse-grained interaction site (the center of the density cloud). While the overall form of the integral (eq. 4.27) is

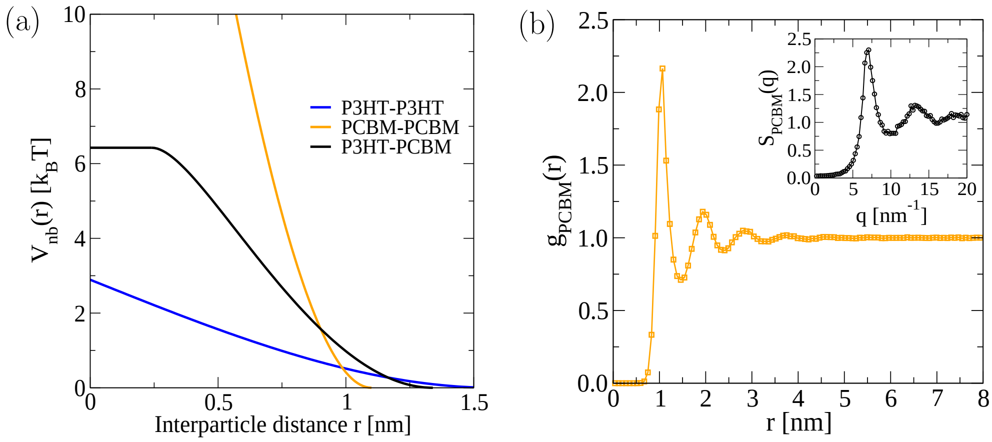

Figure 4.16: (a) Isotropic, repulsive part of the pair potentials describing P3HT-P3HT (blue curve), P3HT-PCBM (black curve) and PCBM-PCBM (orange curve) interactions. The values of the potentials at close distances, i.e. for significant overlap of coarse-grained segments, illustrates the different magnitude of the repulsion for the different combinations of species in the simulation ($\sim 30\,\mathrm{k_B T}$ for full PCBM-PCBM overlap, which is not shown on this scale). In this example, $\chi = 0$ is chosen. Values for χ different from zero modify the strength of the P3HT-PCBM overlap potential additionally. (b) Pair correlation, calculated in the pure PCBM phase. The inset shows the structure factor obtained from the same system.

similar to the corresponding expression for a pure P3HT system (eq. 3.22), performing the explicit integration for different cloud radii is more involved. However, one can make use of a mathematical simplification by performing the calculation in Fourier space. Therefore, the Fourier transformation (in spherical coordinates) for both cloud functions $\omega_{\mathrm{P3HT}}(r)$ and $\omega_{\mathrm{PCBM}}(r)$ is performed. Using the convolution theorem [236], which states that the product of the Fourier transformations of two functions equals the Fourier transformation of the convolution of the latter, the integration reduces to a multiplication in q-space [110]. The solution, which is directly proportional to the pair potential shown in Fig. 4.16a (black curve), using the abbreviated notations $A = \mathrm{P3HT}$ and $B = \mathrm{PCBM}$ and r for the distance between the coarse-grained interaction sites, reads:

$$\begin{aligned}
&\text{For} \quad (\sigma_A + \sigma_B) > r > (\sigma_A - \sigma_B) : \\
&\qquad -\frac{3}{64\pi\sigma_A^3\sigma_B^3 r}(\sigma_A + \sigma_B - r)^2 \left(3(\sigma_A - \sigma_B)^2 - 2(\sigma_A + \sigma_B)r - r^2\right), \\
&\text{For} \quad 0 \leq r \leq (\sigma_A - \sigma_B) : \\
&\qquad \frac{3}{4\pi\sigma_A^3}, \\
&\text{Else} \quad 0.
\end{aligned} \tag{4.29}$$

The different interaction radii have the following effect on the relative strength of the coarse-grained potentials: While the PCBM-PCBM repulsion is strong, with essentially no overlap below a distance of approximately $1\,\mathrm{nm}$, both the P3HT-PCBM and the P3HT-P3HT interactions remain soft, i.e. on the order of a few $k_B T$ for fully overlapping monomers. This is illustrated in Fig. 4.16a for all three possible combinations of coarse-grained interaction sites. The potential strength of $\sim 30\,\mathrm{k_B T}$ for a fully overlapping PCBM-PCBM pair is not shown. The relatively hard repulsive core for the PCBM-PCBM interaction leads to a pronounced structuring for PCBM-rich domains. This is illustrated with the pair correlation function measured in the pure PCBM phase in Fig. 4.16b. The interaction between PCBM particles leads indeed to a strong repulsion of neighbors below a distance of approximately $1\,\mathrm{nm}$. The inset in Fig. 4.16b shows the structure factor, obtained for the same system, accordingly. It follows that the overall phase behavior of the system is sensitive to the specific choice of the PCBM cloud radius, which may render this parameter a good candidate for a future tuning of the generic phase behavior with respect to a real system.

In Fig. 4.17, a mixture is shown at an intermediate composition with 60

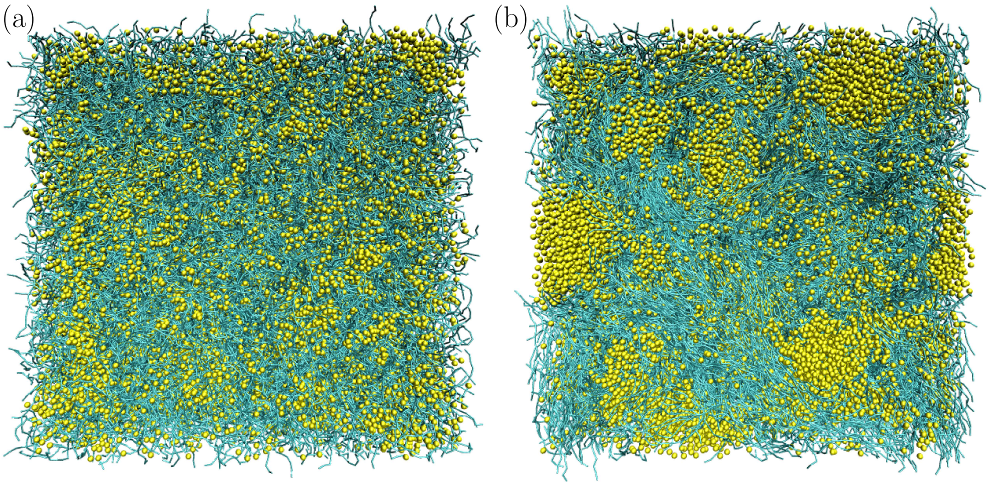

Figure 4.17: (a) Sample snapshot of a morphology obtained for a blend with 60 weight-% P3HT and polymerization degree $N = 17$ hexylthiophenes (i.e., 8 coarse-grained segments). No orientation coupling is present, i.e. $\nu = 0$. (b) Sample morphology of the same system, with activated orientation dependent interactions. In both cases, the Flory-Huggins parameter was chosen $\chi = 0$.

weight-% P3HT for a chain length of 8 coarse-grained segments, which equals a polymerization degree of $N = 17$ hexylthiophenes according to the mapping of a P3HT chain. First, Fig. 4.17a illustrates a representative morphology for $\nu = 0$, i.e. without anisotropic interactions between polymer segments. The mesostructure has no notable domains of pure phases and is homogeneously intermixed. In Fig. 4.17b, the same system is shown with activated orientation coupling, i.e. for $\nu = 6.81$. Obviously, the system has started mesoscopic phase separation, with visible domains enriched by either of the pure species. The polymer has visible nematic domains, while other areas of the morphology are amorphous. The onset of phase separation in the system can be monitored by a set of quantifiers. In Fig. 4.18a, the radial distribution function with respect to mutually different pairs of segments/particles is shown. The function exhibits a characteristic hump at distances $r \approx 6 - 7\,\mathrm{nm}$ for a com-

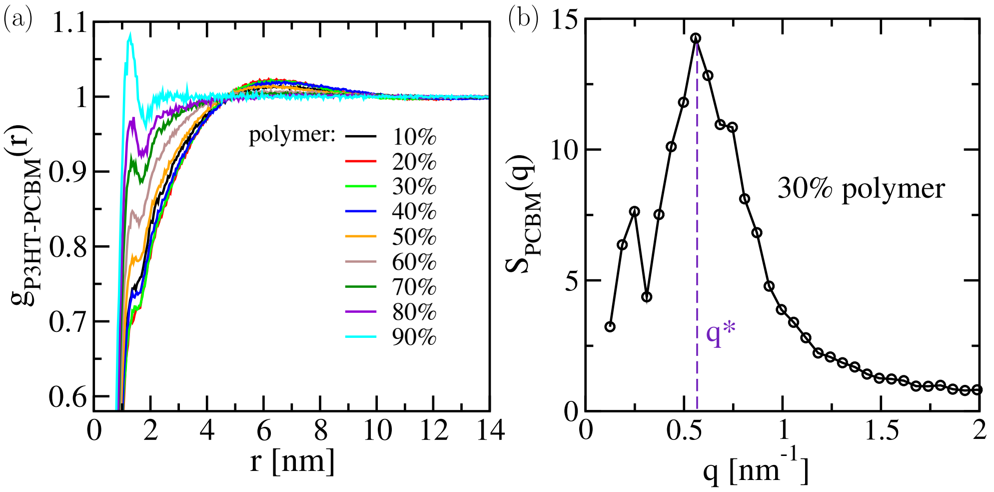

Figure 4.18: (a) The pair correlation function, calculated over pairs of mutually different species, is shown for different compositions, i.e. weight-% of polymers. Calculations were performed for $\chi = 0$, $\nu = 6.81$ and polymerization degree $N = 17$ hexylthiophenes. (b) The structure factor, calculated from the PCBM particle centers, for a composition for which the phase segregation is strong. A clearly visible peak evolves at low q-values, indicating a characteristic mesoscopic length scale at $d \approx 12\,\mathrm{nm}$.

position with less than 70 weight-% of polymers, indicating the evolution of polymer-enriched domains on mesoscopic length scales in these systems. The evolution of a mesoscopic length scale, indicating the onset of phase segregation, can additionally be monitored in the structure factor, calculated from the PCBM particle positions. An example is shown in Fig. 4.18b, in which a clearly visible peak at $q^* \approx 0.55\,\mathrm{nm}^{-1}$ arises, corresponding to a length scale of approximately $12\,\mathrm{nm}$.

For a brief conclusion, the model study suggests that the generic behavior of polymer ordering enhances the overall phase separation of the system.

4.7 Conclusions

In this part of the thesis, a coarse-grained modeling approach for partially ordered, liquid crystalline biaxial-nematic mesophases of poly(3-hexylthiophene) was introduced. It combines a top-down approach for modeling the macroscopic thermodynamic behavior of the system with a bottom-up coarse-graining scheme for polymer backbone configurations, retaining a relatively detailed molecular representation. This offered the possibility of charge transport related calculations.

Despite the fact that the non-bonded interactions are soft, it was found that the macroscopic material properties described with this method, for example Frank elastic constants, have typical values reported for real polymer LC material [98, 99]. Furthermore, the dependence of the isotropic-nematic transition on chain length agrees qualitatively with experimental findings [148].
In the isotropic melt, a majority of rather short conjugated segments was found, due to frequent torsional defects which are homogeneously distributed along the chain backbone. For biaxially ordered morphologies, a significant amount of chains was found in a fully conjugated state (the distribution of the conjugation length is peaked at $l = N$) and the torsional defects tend to localize near the chain ends. The specific distribution of conjugation lengths influences the density of states for such systems, which was found to have a three-level structure. Interestingly, site energies have been found weakly correlated.

The model incorporates many of the microscopic details that are crucial for reintroducing atomistic details into the coarse-grained morphologies, e.g. backbone conformations and thus the explicit spatial orientation of thiophene rings. This motivated a further elaboration of a multiscale modeling approach in order to reintroduce atomistic degrees of freedom via an intermediate coarse-graining step. This will be the topic of the following chapter.

5 Reinsertion of atomistic details into coarse-grained morphologies

Parts of this chapter have been accepted for publication:
P. Gemünden, C. Poelking, K. Kremer, K. Ch. Daoulas, and D. Andrienko, "Effect of Mesoscale Ordering on the Density of States of Polymeric Semiconductors", Macromolecular Rapid Communications (2015), DOI:10.1002/marc.201400725.

5.1 Motivation

The model presented in the previous chapter aimed at the approximation of large-scale, partially ordered morphologies of polymeric semiconductors - here, as a test case, of P3HT. For the ansatz, a high degree of coarse-graining was used (one CG interaction site represents a whole thiophone unit including the hexyl side chain), which allows for a significant overlap of coarse-grained segments. Hence, the equilibration of liquid crystalline mesophases on large scales was possible.

In order to use the generated morphologies further for calculations related to charge transport, ultimately, an atomistically resolved morphology is crucial. The resulting coarse-grained structures cannot be used directly for such cal-

culations, since monomers show significant overlap and side chains are not explicitly present (compare results discussed in ch. 4.5.2).
In this chapter, a backmapping scheme for atomistic details is developed. This scheme enables to reiterate the local structure of the coarse-grained morphologies and, eventually, reintroduce atoms on backbones and side chains. At the final stage, the backmapping leads to large-scale samples with atomistic details.

For polymers, strategies for the backmapping of atomistic details have been reported for a variety of systems. In a first systematic approach [8, 9], a procedure was presented to first parameterize a coarse-grained bead-spring model from an underlying atomistic representation at a rather high temperature. In a second step, the atoms were put back systematically, and the structures were relaxed at full atomistic detail. The structural properties, such as neutron scattering patterns, have been compared to experiments and showed relatively good agreement. However, simulations have been performed for high temperature melts, and in this regime the local packing of the liquid does not rely on many structural details. For more ordered structures, the systematic approach of generating a coarse-grained potential from an atomistic reference system is more involved. A recent study demonstrated a full coarse-graining - fine-graining cycle for liquid crystalline mesophases of macromolecules [199]. In this work, the idea was to sample the coarse-grained potential parameters from an atomistic reference system close to the disorder-order transition. The coarse-grained simulation was subsequently used to drive the system towards the transition to liquid crystalline order, which was preserved after the backmapping of atoms [199]. In many other cases, however, the transferability, i.e. the ability of using the same coarse-grained potential at different state points of the systems, is rather limited [14, 16].

The relaxation of a system after backmapping at the atomistic level is usually not an equilibration with respect to the global energy minimum. The dynamics is, already for moderate system sizes and complexity, too slow when all atoms are present. Having reintroduced atomistic details, the global structure may relax to a local energy minimum, and further equilibration may not be observed in finite simulation time. With the ansatz presented in this chapter, the equilibration of the system is performed on different length scales *separately*, starting from the coarse level via an intermediate stage to the fine scale.

In chapter 4, a model was developed in order to generate large-scale liquid crystalline mesophases of conjugated polymers with a different degree of mesoscopic order (amorphous, uniaxial-nematic, biaxial-nematic). Despite the fact that in such systems liquid crystalline phases are important *on their own*, the liquid crystalline mesophase may be seen as an approximation to the partially ordered, semi-crystalline structure of the real material (see ch. 4.1 for a more general motivation). The generated morphologies capture the main aspects of the mesophase symmetry and molecular details of the real system. A reintroduction of atomistic details and subsequent equilibration allows for a generic investigation of structure-property relations from fully atomistic large-scale samples. For example, in the spirit of the investigations in ch. 4, one can study the relationship between mesoscale order and the energetic landscape that is important for charge transport.

Compared to other available coarse-graining schemes for similar systems in the literature [54, 69, 185], the biaxial model in this work takes structural details into account that enhance the backmapping. For example, it incorporates the information about explicit thiophene ring orientation. However, the main challenge is the reintroduction of explicit side chains.

In order to approach this challenge, a full backmapping strategy is developed, first for the most simple case of disordered melts. Following that, a strategy for the systematic backmapping of atoms into more ordered, biaxial liquid crystalline structures is presented. A brief outlook summarizes how this strategy can be used for a systematic study of charge transport related properties in partially ordered mesophases.

5.2 Backmapping in P3HT: Roadmap

The backmapping is performed in several intermediate steps, illustrated in a workflow diagram in Fig. 5.1. For the test configurations, in which atomistic details are backmapped, three representative configurations are chosen, obtained with the soft coarse-grained model described in ch. 4. A fully amorphous mesophase as well as a uniaxially and a biaxially ordered mesophase are considered. These configurations were obtained at the reference temperature $T = 500\,\mathrm{K}$, with interaction parameters $\kappa = 6\,\mathrm{k_BT}$, $\nu = 2.5\,\mathrm{k_BT}$ (uniaxial mesophase, $\lambda = 0$) and $\lambda = 5.5\,\mathrm{k_BT}$ (biaxial mesophase, $\nu = 0$). For the initial density, $4\,\mathrm{hexylthiophenes/nm^3}$ is set, motivated by previous experimental data (see ch. 4 for details). The volumetric properties of each phase (uniaxial, biaxial or amorphous) after backmapping are fine-tuned during a final relaxation in the nPT ensemble.

The local packing of these configurations is refined with an intermediate coarse-grained potential, which is derived from an atomistic reference melt. Therefore, an existing P3HT structure in the crystalline phase was heated above the melting temperature and quenched to the reference temperature. For the derivation of the intermediate coarse-grained potential, the interactions between thiophene units were obtained from an Iterative Boltzmann Inversion (IBI). This algorithm was described earlier (see ch. 2.1.2 and middle panel in Fig. 5.1).

In the last step, the original atomistic force field is gradually restored and the system is locally relaxed at full atomistic details (see right upper panel in Fig. 5.1).

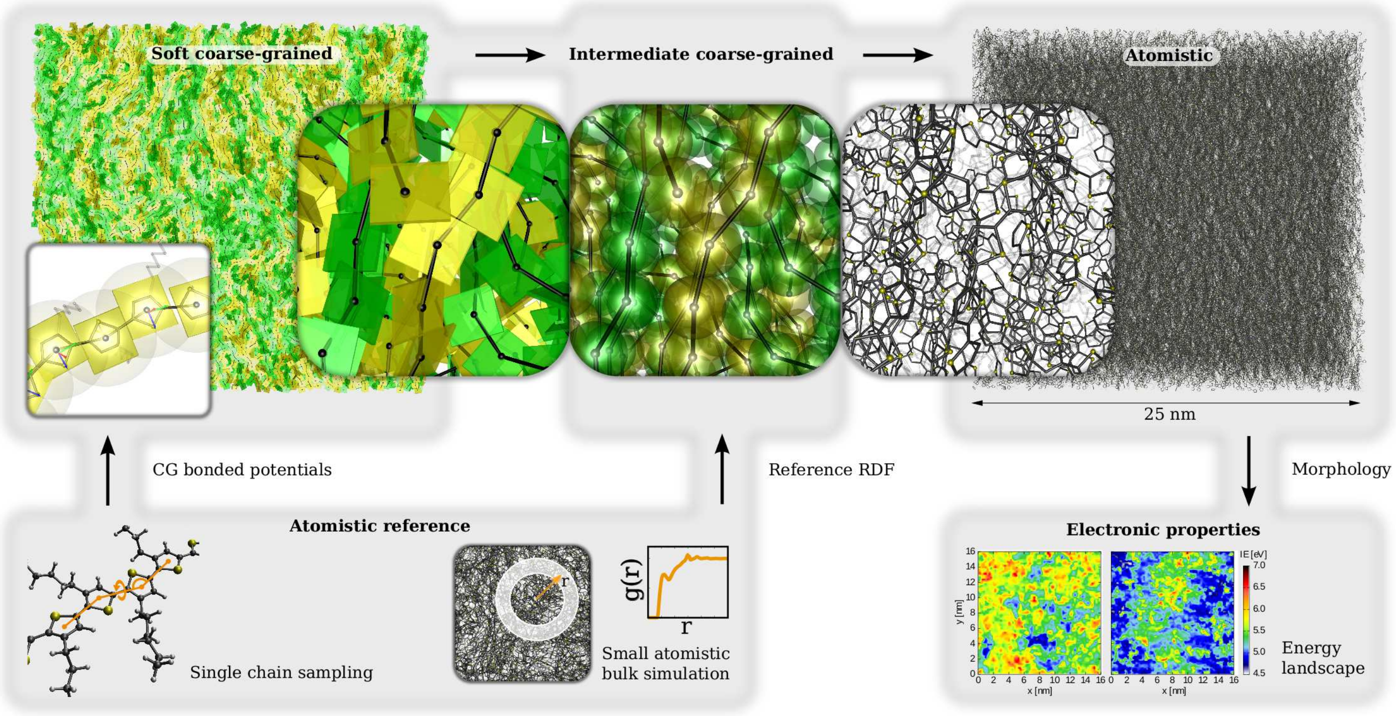

Figure 5.1: Workflow diagram for generation of large-scale amorphous and liquid crystalline morphologies of conjugated polymers with full atomistic details. The morphology on large scales (i.e., low resolution) is obtained with the soft coarse-grained model described in ch. 4. An atomistic single chain reference serves as an input for the parameterization (top left and lower panel). The local structure is reiterated with an intermediate CG model, creating the excluded volume of monomers (top middle panel). The intermediate model is parameterized from small atomistic bulk simulations (middle lower panel). Eventually, all atoms on backbones and side chains are reintroduced and structures are locally relaxed at full atomistic detail (top right panel). They serve as an input for the calculation of electronic properties (right bottom panel).

5.2.1 Intermediate model - relaxing local structure

The morphologies obtained from the approach with soft anisotropic potentials are lacking a realistic local packing since segments are overlapping.
In order to correct for the latter, the liquid structure is reiterated in an intermediate backmapping step, recovering the realistic excluded volume of a thiophene in the bulk. This step is particularly important in the scope of the reinsertion of explicit side chains (see sec. 5.2.2). The coarse-grained potential which generates the correct packing is derived iteratively from a small atomistic bulk reference simulation, which was used to obtain the specific target structure for the reiteration step (see middle panel of Fig. 5.1 for an illustration).
Prior to the derivation of the intermediate CG potential, the prerequisite step of generating a bulk reference structure is shortly described. For this purpose, the atomistic reference melt was generated from a Molecular Dynamics simulation of a bulk structure of 400 regio-regular P3HT chains, with 20 repeat units per chain. The sample was heated well above the melting temperature to $T = 750\,\mathrm{K}$ and was subsequently quenched to the reference temperature $T = 500\,\mathrm{K}$. As an initial starting configuration, a crystalline P3HT structure was used. This configuration was kindly provided by Carl Poelking and stems from earlier Molecular Dynamics studies of such systems. Conventional Berendsen thermostat and barostat coupling algorithms [237] were applied, in order to achieve a fast equilibration towards the target structure (coupling constants were set $0.1\,\mathrm{ps}$ and $0.5\,\mathrm{ps}$, respectively, with a reference pressure of $1\,\mathrm{bar}$).
All MD simulations were performed using the GROMACS package [47] with a reparameterized version of the OPLS force field [194, 195]. A long trajectory, i.e. several nanoseconds, was prepared, in order to ensure the equilibration of the main system quantifiers, e.g. the total energy and density, illustrated in Fig. 5.2.

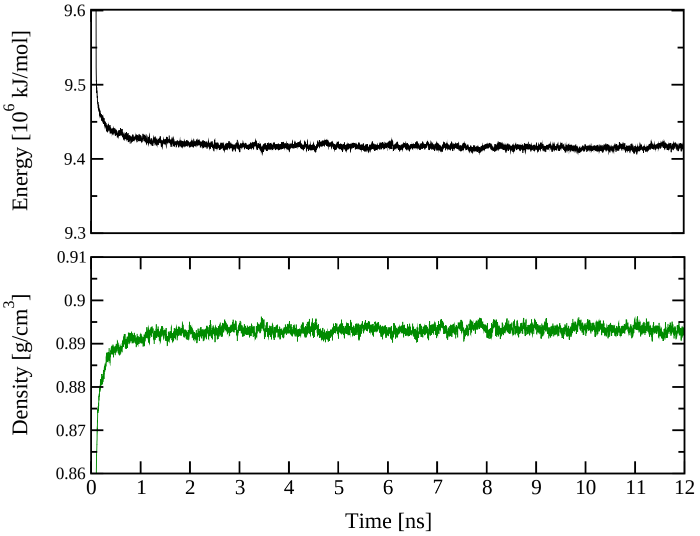

Figure 5.2: Example for the monitoring of main system quantifiers during the quench of the atomistic reference system (400 P3HT chains) at the reference temperature $T = 500\,\mathrm{K}$.

The RDF is extracted from the atomistic reference trajectory with respect to the CG mapping points. Neighbors across more than two monomers (up to 1-4 interactions) are excluded from the analysis, in accordance with the single chain sampling described in ch. 4. For the density, $\rho = 0.89\,\frac{\mathrm{g}}{\mathrm{cm}^3}$ is measured (see Fig. 5.2), which is close to values reported for an amorphous melt of P3HT 20mers at the same reference temperature in similar simulation studies [238] (note, however, that the system density might depend on the choice of the atomistic force field).

With the atomistic bulk reference at hand, the intermediate CG potential is prepared for the reiteration of local packing of thiophene segments, using the reference RDF obtained as described above. Interactions are active with respect to the CG mapping points (see middle panel of Fig. 5.1). The first guess for a suitable distance dependent pair potential is drawn from the potential of average force by inverting the reference RDF (see Fig. 5.3b). A sequence

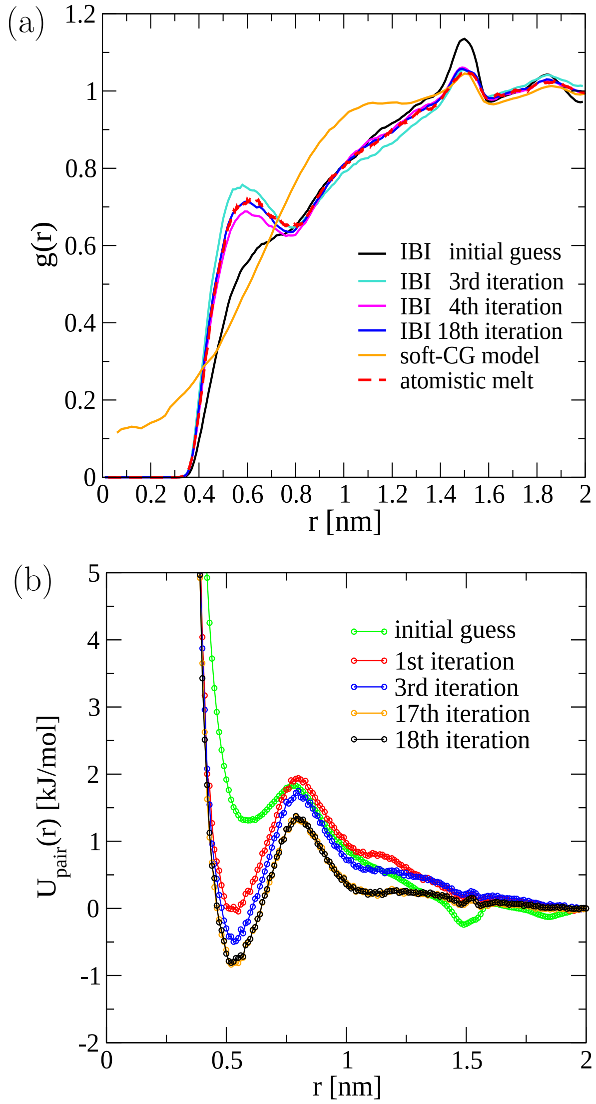

Figure 5.3: (a) RDF, as evolved during an Iterative Boltzmann Inversion (IBI), compared with the atomistic reference structure (thick, broken red line), and the RDF obtained from the soft coarse-grained model (thin orange line). Note that the local packing which is generated by the soft CG model approximates the real liquid packing, which allows for a fast reiteration towards the target RDF. (b) Pair potential, iteratively updated during IBI.

of short cycles of MD simulations is started in the NVT-ensemble with this potential. In each step, it is updated according to the Iterative Boltzmann Inversion (IBI) scheme [11, 185] using the VOTCA-CSG package [44] (here, without pressure correction in the IBI). Fig. 5.3a shows the RDF for the first few and the last iteration cycles of the IBI, as well as the corresponding pair potential in Fig. 5.3b, obtained in tabulated form. After ~ 18 iteration cycles, the RDF of the CG system cannot be distinguished from the reference. The convergence is monitored by running a few longer test simulations.

Eventually, the intermediate relaxation potential is applied to the amorphous and biaxial CG mesophases. Technically, this is done with all atoms already present in the system, however they are non-interacting with respect to non-bonded potentials. Atomistic coordinates are resolved by fine-graining coarse-grained chain backbones under the constraint that the mapping points of hexylthiophenes in the atomistic and CG representations are equal. Additionally, each thiophene is rotated in order to match its molecular axis, with the segment orientation read directly from the CG configurations. It is stressed that this is a significant advantage compared to models for which the ring orientation has to be build or guessed during the backmapping step [9, 54]. Technically, atoms belonging to a hexylthiophene are moved according to the mapping center during the intermediate relaxation, being constrained by a virtual site construction to their reference CG mapping centers (atoms are not shown in Fig. 5.1 at this stage). The virtual site constraints were used as implemented in the GROMACS package [47].

During the intermediate relaxation step, global chain conformations are monitored not to change significantly from the initial state, i.e. segments are only moving on length scales much smaller than the extension of a polymer chain. Therefore, simulation time is kept short, i.e. $t \approx 20\,\mathrm{ps}$ (in the CG simulation). Since the collective order of segments with respect to the plane normal is more sensitive to local translation and rotation of CG segments, this is more important for the biaxial mesophases. Side chains are not explicitly present (noninteracting) and chain backbones are essentially cylindrically symmetric. In the amorphous phase, the average end-to-end distance of chains is measured, ensuring a change of less than 1% during the local relaxation step.

5.2.2 Recovering atomistic morphologies

In the last step, all atoms are reintroduced explicitly (i.e. the full atomistic force field is applied) and a local relaxation of atomistically detailed morphologies is performed ("backmapping"). In the following, the individual steps used for the reintroduction of details are briefly explained.

Step 1: A realistic packing of side chains is recovered. This step is crucial, since atoms belonging to a hexyl chain potentially overlap with neighboring groups (this procedure is similar to the local reiteration of excluded volume on the level of CG segments, see sec. 5.2.1). For this purpose, backbone conformations are practically frozen, using a strong restraining potential which constraints CG mapping centers to their instantaneous positions. In this way, the global morphology is preserved. A Stochastic Dynamics (SD) integrator is used together with force-capped Lennard-Jones (LJ) interactions, as implemented in the GROMACS package [47], for the removal of overlap on atomistic scale in the early stage of simulations. Thereby, hard excluded volume repulsion is modified by interpolating the original LJ potential at short distances with a soft-core interaction, in order to remove the unphysical overlap in a controlled way. Hence, side chain conformations can relax with respect to their local environment. It is monitored that an end group has moved a distance of only a few carbon bond lengths on average. Empirically, the removal of atomistic overlap is obtained fast, on time scales below $100\,\mathrm{ps}$. In the first step of atomistic backmapping, Coulomb interactions are not present. The temperature is coupled with the Berendsen thermostat [237] to the reference value $T = 500\,\mathrm{K}$. Following this first relaxation with force-capped LJ poten-

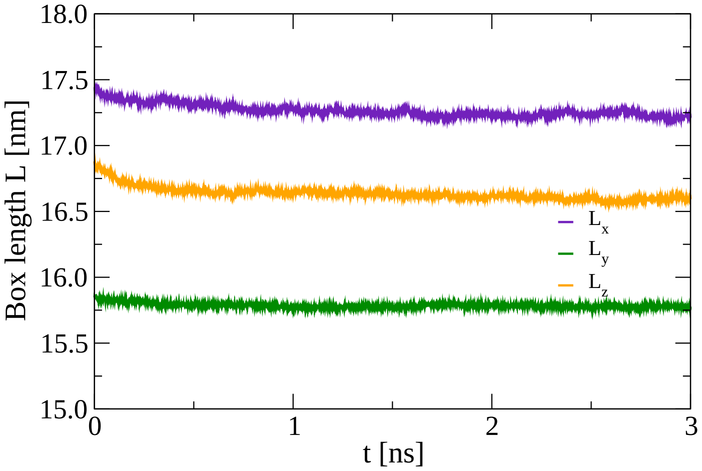

Figure 5.4: Spatial extension of the simulation box for the example of a backmapped biaxial mesophase, during the last stage of full atomistic backmapping.

tials, the full LJ interaction is recovered, while Coulomb interactions remain deactivated. The simulation is continued for $t = 100\,\mathrm{ps}$.

Step 2: Second, simulations in the NPT-ensemble are performed, in order to correct for a realistic packing density in the mesophase of choice. For the morphologies obtained with the soft CG model (see ch. 4) an initial guess for the number density is used, according to the value reported from experiments on crystalline P3HT at room temperature [177]. In particular for the biaxial mesophase, this is an important step, as the intermediate CG model was constructed by default with an isotropic potential, which cannot correct for the anisotropic packing density in the real material. Fig. 5.4 shows an example of the evolution of the simulation box length in all three spatial dimensions during the last step of full atomistic backmapping. Note that chains are aligned along the x-axis in this example, while thiophene plane normals are collectively aligned along z. The simulation box becomes clearly anisotropic, in

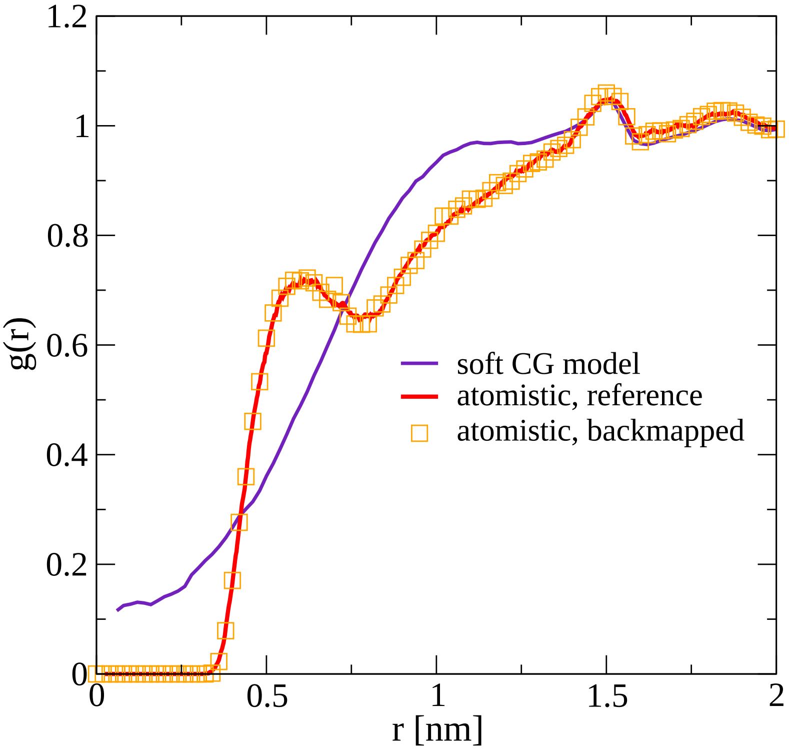

Figure 5.5: RDF, measured after a full backmapping cycle (orange squares) for a large amorphous system (1.8×10^6 atoms) at the reference temperature $T = 500\,\mathrm{K}$, compared with the atomistic reference structure (thick red line) and the soft CG model (solid purple line).

contrast to the backmapped amorphous and uniaxial-nematic phases.

For amorphous mesophases, structures have been relaxed with unconstrained MD simulations (NPT-ensemble) for a few nanoseconds at the reference temperature, until the total energy and the density have stabilized. Fig. 5.5 shows a comparison of the radial distribution function calculated after backmapping (orange squares) with the structure of the initial atomistic reference system (solid red line). Both structures are very close to each other and cannot be

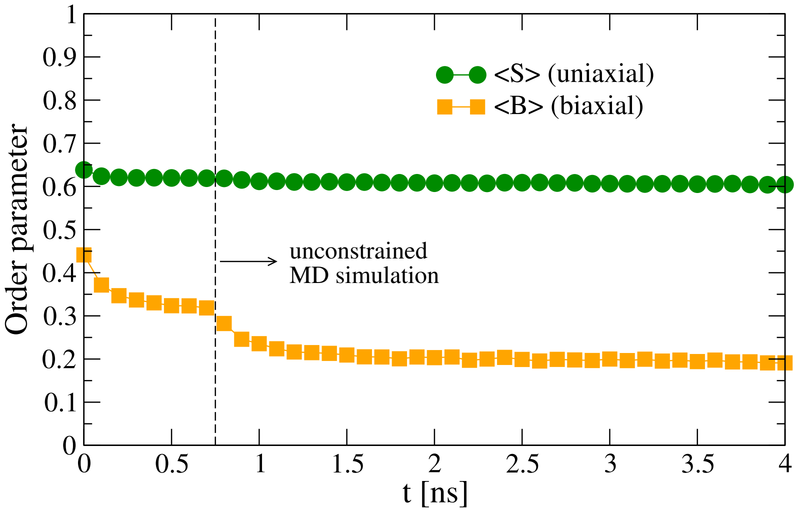

Figure 5.6: Evolution of order parameters in the second step of backmapping for a partially ordered, biaxial mesophase. S quantifies uniaxial-nematic alignment of chain backbones. B is a “true” biaxial measure, vanishing in the amorphous *and* in the uniaxial-nematic mesophase. Data is shown for $T = 300\,\mathrm{K}$, for which significant biaxial order (i.e., $B \approx 0.2$) is preserved after a full backmapping cycle. The dashed line indicates the release of dihedral restraining potentials, which were used for preserving the planar chain conformations in the early stage of relaxation.

distinguished by eye. The system was quenched to $300\,\mathrm{K}$ for all following analysis, since charge transport related measurements are typically performed at room temperature. At this temperature, a density $\rho \approx 1.03\,\frac{\mathrm{g}}{\mathrm{cm}^3}$ is measured, which is close to the regime reported experimentally for P3HT (note however that experiments typically involve much higher molecular weights) [177].

For biaxially ordered mesophases, the last stage of backmapping is more challenging. In order to prevent the mesophase to loose the biaxial order of chain segments, dihedral angles are coupled to a strong restraining potential,

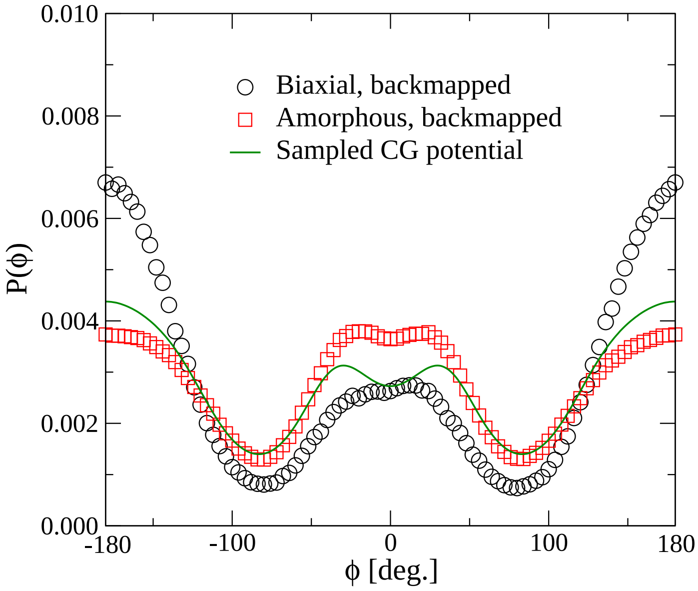

Figure 5.7: Distribution of torsion angles (normalized), after backmapping in the amorphous (red squares) and the biaxial phase (black circles). For comparison, a distribution sampled from the CG potential is shown, which was initially obtained from a reference simulation of a single chain at $T = 370\,\mathrm{K}$ (compare ch. 4.3.2). All distributions are shown for the final stage of backmapping, at temperature $T = 300\,\mathrm{K}$.

fixing the individual torsional conformations of chains. The systems are subsequently relaxed in SD simulations for $800\,\mathrm{ps}$, see Fig. 5.6. Following that, an unconstrained MD simulation is performed for several nanoseconds, until the total energy and the density stabilized. Fig. 5.6 shows the uniaxial and biaxial nematic order parameter for the last stage of full atomistic backmapping. The uniaxial nematic order ($S \approx 0.6$) is found relatively stable over time. For biaxial order, quantified by the order parameter B (see ch. 4 for details), a significant decrease at the initial stages of constrained and unconstrained runs is observed. However, both parameters stabilize within a few nanoseconds run-

time at $S \approx 0.6$ and $B \approx 0.2$, respectively.
Fig. 5.7 shows a comparison of torsion angle distributions for the backmapped amorphous (red squares) and biaxial phase (black circles), both at the reference temperature $T = 300\,\mathrm{K}$. A pronounced increase in torsion angles close to $\phi \pm 180°$ can be observed for the biaxial phase, which indicates the pronounced planarization of chain backbones compared to the amorphous phase. Additionally, a distribution sampled from the CG potential is shown (solid line), obtained from a Boltzmann-Inversion of the corresponding distribution from an atomistic reference simulation of a single chain in Θ-solvent condition at the reference temperature $T = 370\,\mathrm{K}$ (see ch. 4.3.2). Assuming transferability (compare ch. 4.3.2), the distribution was rescaled to the same reference temperature $T = 300\,\mathrm{K}$.
It is briefly noted that for significantly higher temperatures, above $T \approx 400\,\mathrm{K}$, the global biaxial order could not be stabilized, i.e. the system tends to drive into an uniaxial mesophase in this case.

5.2.3 Applications

In this chapter, the ability to generate atomistically resolved mesophases at large scales with different degree of mesoscopic order - from amorphous via nematic to biaxial nematic ordering - was demonstrated. In a collaboration with Carl Poelking and Denis Andrienko, these structures have been analyzed in order to understand the role of mesoscale chain ordering for charge transport. The atomistic resolution which was restored with the backmapping procedure allows the accurate parameterization of molecular fields and field responses, that give rise to electrostatic and polarization effects.

Figure 5.8 shows the ionization energy landscape averaged over a $2\,\mathrm{nm}$ thick slice of the amorphous and biaxial mesophase. The calculations of the results shown in this figure were carried out by collaborator Carl Poelking, taking

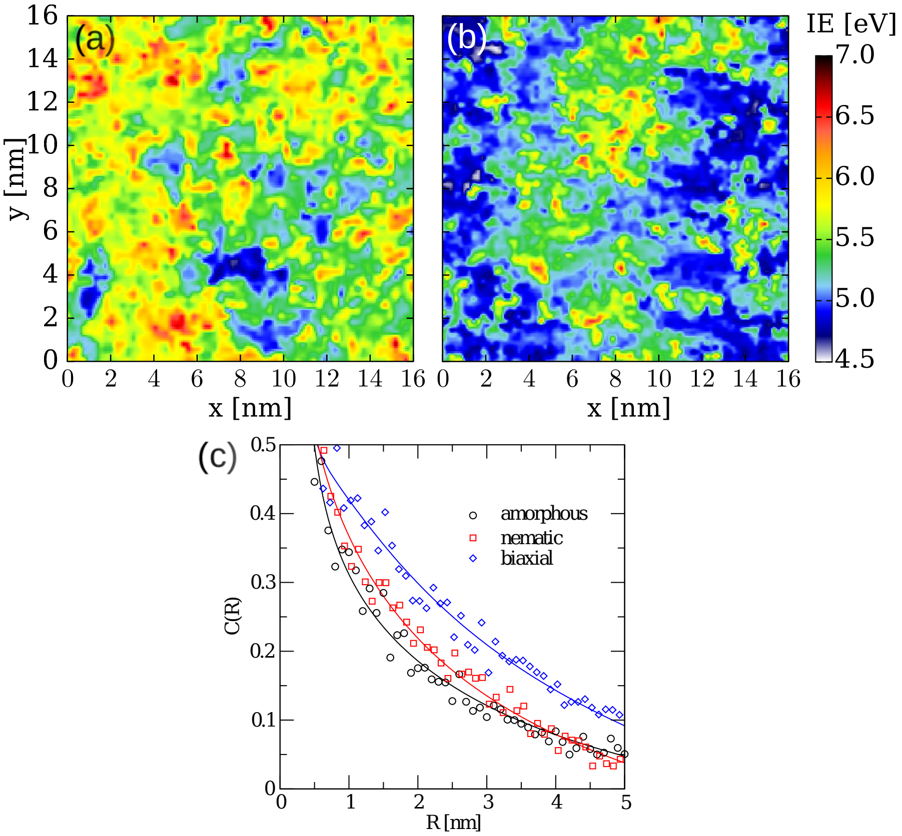

Figure 5.8: Spatially resolved ionization energy for holes, averaged over a 2 nm-thick slice of an (a) amorphous and (b) biaxial mesophase. The chains are aligned with their backbones along the x-axis. For the biaxial mesophase, correlation “islands” are visibly aligned with the nematic director. (c) The spatial site-energy correlation function for the amorphous, uniaxial-nematic and biaxial mesophase. The increase of correlations is partially due to long-range order (compare with Fig. 4.15).
All calculations for the results shown in this figure have been performed by Carl Poelking. For more results and discussions on the charge transport related properties, see Refs. [3, 239]

into account electrostatic and polarization contributions (for further details, see Refs. [228, 229], as well as the publication underlying this chapter). The energetic landscape is increasingly correlated for liquid crystalline morphologies, most pronounced for the biaxial mesophase. Fig 5.8a shows an example for an amorphous mesophase, in which the energy landscape is fragmented. Fig 5.8b presents the analog for a biaxial mesophase, in which correlations are visible as patches of low ionization energy that align with the nematic director (along the x-axis). Fig 5.8c summarizes the increase of the site-energy correlation function from the amorphous via the nematic to the biaxial mesophase. Partially, this correlation is due to long-range order (compare with the analysis presented earlier in ch. 4.5.2), and partially due to electrostatic interactions. An increasing correlation of the energetic landscape reduces the site energy differences in the system, facilitating charge transfer in the material. For a detailed discussion of the charge transport related investigations, see the publication underlying this chapter [3].

5.3 Conclusions

In this chapter, a hierarchical scheme for backmapping of atomistic details into partially ordered, large-scale morphologies of conjugated polymers was presented. As a test case, the method has been validated for poly(3-hexylthiophene) (P3HT). In this scheme, morphologies with increasing mesoscopic order - from amorphous to uniaxial-nematic to biaxial-nematic order - have been equilibrated on large scales with the soft coarse-grained model introduced in chapter 4. With the help of an intermediate coarse-grained model, derived systematically from small atomistic reference simulations, a realistic local packing of thiophene units was recovered, which is a crucial step in order to reintroduce explicit side chains in the following. In a last step, all atoms on backbones and side chains were reintroduced and the structures were locally relaxed with the full atomistic force field.

It was found that large scale ordering can be retained after backmapping. Therefore, a number of positional and conformational constraints have been used for retaining most aspects of molecular ordering in the mesophase while backmapping. For the amorphous phase, relaxation is fast and no additional constraints are needed for retaining the global conformations of the chains. This was not surprising, since the intermediate coarse-grained model was derived from the same amorphous structure, thus the intermediate model samples (approximately) the same global conformations than those obtained with the soft coarse-grained model.

For the biaxial mesophase, the situation is more difficulties. A substantial degree of planar ordering is lost during the last steps of backmapping into biaxial liquid crystalline morphologies (compare sec. 5.2.2). Therefore, a strong restraining potential for the torsional angles was used, in order to preserve the planar order of chain backbones.

However, two questions remain. First, it is not obvious if the amount of biaxial order which was found after backmapping ($B \approx 0.2$) is limited by the structure at atomistic detail itself. In other words, it is not clear if the strength of ordering is limited by the fact that the morphology at atomistic detail is significantly unstable in a biaxially ordered mesophase. The biaxial order does not take into account the preferential lamellar stacking of thiophenes in the crystalline phase, i.e. there is no periodicity in the density distribution. The second question is how one could improve the intermediate coarse-grained model, in order to arrive at atomistic structures with an increased degree of planar ordering - and, eventually, an increased amount of π-overlap. In the following, it is briefly outlined how these two questions could be adressed in future work.

In order to understand the reason why the biaxial order parameter drops significantly during the backmapping procedure, there is a demand for a further, systematic accounting of simulation parameters while backmapping. These parameters are diverse. One first way of improving the backmapping could be the iterative refinement of the initial starting volume used for the soft coarse-grained simulations (compare ch. 4). In this study, this was assumed from experimentally reported values of a P3HT structure at room temperature. Since after a backmapping cycle, the approximate target volume at the chosen temperature is known, this information could be used for improving the starting configurations in a self-consistent way. This may reduce the very high forces at the first initial steps of relaxation, which negatively affect the planar orientation.

The second question was how one could improve on the planar ordering and π-packing of chains on the level of the coarse-grained models. Currently, there may be two possible pathways. First, the soft coarse-grained model could be extended in order to account for a packing with positional periodicity, i.e. biaxial smectic ordering [240, 241]. In that way, chains could not only be brought to structures with planarization of chain backbones, but also with a strong π-overlap once the atomistic details are backmapped. A second, possibly alternative improvement could be made at the stage of the intermediate coarse-grained model. The potential derived from the Iterative Boltzmann Inversion was calculated from an amorphous structure. The potential has one pronounced minimum and, thus, does not resolve many of the microscopic structural details such as monomer anisotropy. In other approaches, a local packing which takes into account the π-stacking of monomers was introduced on the basis of a pair potential which was parameterized from a crystalline structure [242, 243]. Such pair potentials have *many* minima, resolving the underlying details of non-isotropic packing at close distances.

To summarize, both strategies, a refined soft coarse-grained potential and/or a refined intermediate potential could improve for a generation of large-scale, partially ordered mesophases which are closer to the real material.

6 Summary and outlook

This thesis addresses the development of generic, particle-based models for polymeric soft matter systems at large scales, in which the microscopic details are linked to the large-scale morphology of the material. The models are developed in a *top down* approach, in order to reproduce the macroscopic phase behavior of the system and, at the same time, incorporate the essential molecular features at the microscale. A representative example of such an interplay between the molecular details and long range order are polymeric materials which tend to crystallize. This behavior is observed for many polymeric semiconductors, for which the effect of anisotropic π-stacking interactions leads to lamellar-like, crystalline packing [177]. The problem of modeling such hierarchically ordered morphologies is approached in this thesis starting from a less ordered state of matter - the liquid crystalline phase.

Methodologically, the basic idea of the modeling framework is to impose a generic phase behavior through a Hamiltonian given as a functional of local order parameters, similar to the ansatz in field-theoretical approaches to liquid crystalline polymers [26, 121–124]. Models developed in this spirit have been used earlier for functionals expressed through scalar order parameters, e.g. the local segment density [32–34, 93, 94]. In these approaches, particle-based, pairwise interactions are explicitly derived from the functional. The connection between a particle-based and a field-based representation helps to parameterize the pairwise potentials, because the interaction parameters can be estimated from the functional in the mean field limit [31, 34].

As one of the main developments in this thesis, the approach in which pairwise potentials are derived from a functional is extended to account for more complex, tensorial liquid crystalline order parameters, capturing nematic and biaxial-nematic symmetry.

In chapter 3, a generic model for nematic liquid crystalline polymers (LCP), which was used in Ref. [69], was developed further. It is based on pairwise interactions, derived from a functional of the local density and the local nematic orientation tensor. The interactions are soft, i.e. on the order of the thermal energy k_BT even for fully overlapping segments. The generic polymer model was investigated with Monte Carlo simulations, in order to generate and analyze large-scale nematic LCP morphologies. It was shown that the modeling framework can be used to address fundamental physical questions about the macroscopic behavior of LCP. Accordingly, the density and director fluctuation spectra in the system were measured. The long-wave length behavior of these fluctuation spectra is connected to macroscopic material properties, i.e. elastic constants. The generic characteristics of the scattering contours predicted by theories for LCP and reported from experiments, as for example the bowtie-shaped pattern of the density structure factor, is confirmed by the simulations. One of the main results presented in this thesis is the linear dependence of the splay Frank elastic constant on the chain length, which is in agreement with the predictions by Meyer [103] and following theories [103–105, 108]. The result disagrees with an earlier estimation by de Gennes [101], who predicted a quadratic scaling with chain length.

In chapter 4, the modeling scheme was extended to more complex molecular geometries and more complex macroscopic phase behavior. A first step was presented towards reflecting more closely the main additional features of the mesoscale structure found for many polymeric semiconductors. Namely, the ordered phase exhibits an alignment of chain backbones on average parallel to each other and, additionally, co-planar, biaxially oriented chain segments due

to π-stacking interactions. The model accounts for the interplay of the underlying anisotropy of the molecular architecture and π-stacking interactions and the biaxial mesoscale symmetry.
As a test case, biaxial liquid crystalline mesophases of poly(3-hexylthiophene) (P3HT) were studied, assuming that each thiophene segment including the attached side chain can be described as an object with plate-like symmetry. The bonded potentials were derived in a systematic way from an atomistic reference system. Using Monte Carlo simulation techniques, it was possible to equilibrate systems in the biaxial state with a box length up to $\sim 50\,\mathrm{nm}$ and chains with 32 repeat units.
The model is general and can be applied to various molecular architectures. It has been found that the director fluctuations measured from the simulation reflect a realistic order of magnitude for the elastic constants. Furthermore, the transition from the isotropic to the liquid crystalline phases appears at weaker coupling strength for increasing chain length, in agreement with experimental findings. Even without considering atomistic degrees of freedom in the coarse-grained model, it was possible to analyze the morphologies with respect to properties that are important for charge transport. For example, it was possible to connect the conjugation length distribution of the chains to the mesoscopic order in the material. For the biaxial phase, a correlated energetic landscape was observed, even though no electrostatic interactions were considered.

In chapter 5, the biaxially ordered large-scale morphologies described in ch. 4 were investigated further regarding the properties that are relevant for charge transport. Ultimately, an accurate description of the latter relies on the atomistic structure. In order to reach the atomistic level, a hierarchical scheme for the reinsertion of atomistic details (*backmapping*) into LCP mesophases with different degrees of order was developed. The scheme was tested for a sequence of an amorphous, a nematic and a biaxial system. The method is based on the idea to restore an approximate excluded volume of chain segments with an intermediate coarse-grained model, which facilitates the reinsertion of atomistic details and, in particular, the explicit side chains. The methodological framework is general and not limited to P3HT. As an outlook, an analysis of correlations in the energy landscape was briefly presented, taking into account electrostatic contributions.

A short outlook on the extension of the coarse-grained modeling scheme to describe multicomponent systems was presented in ch. 4. Such blend systems exhibit a complex interplay between ordering effects of each component individually (e.g. crystallization in the pure phase) and the phase behavior of the mixture. A systematic understanding of the latter effects is important for basic theory and practical applications, for example for the control of the bicontinuous, phase separated morphologies in P3HT:PCBM blends. The model developed in ch. 4 could serve as a tool for investigating the interplay of ordering effects and phase separation on a generic level. In first test simulations, the model showed promising features in this respect, such as the sensitivity of the phase behavior on the nematic coupling strength.
The investigation of generic relationships between mesoscopic order and molecular conformations for polymeric semiconductors was described in the chapters 4 and 5 for the sequence of amorphous via nematic to biaxial mesophases. As already mentioned, a lamellar-like packing due to π-stacking interactions is experimentally observed in the crystalline phase of real P3HT [177], which is not captured by the biaxial model proposed in this thesis. Such patterns could be described with the soft coarse-grained model when extended to account for smectic ordering [240, 241]. Hence, the incorporation of smectic order parameters could refine the description of packing details and thereby facilitate the backmapping procedure discussed in ch. 5. Along the same line, the intermediate step of the backmapping scheme may be improved by substituting a systematically coarse-grained model which considers a larger extend of local packing effects, such as planar π-stacking (compare Refs. [242, 243]).

Appendix

1 Pair potential evaluation

The following calculation illustrates the explicit transformation of the functional of local density and the nematic and biaxial order tensors into a pairwise potential using the density clouds discussed in the chapters 3 and 4.
Starting from the functional

$$\begin{aligned}\frac{H_{biaxial}\left[\hat{\rho},\hat{\boldsymbol{Q}},\hat{\boldsymbol{B}}\right]}{k_BT} = \rho_0 \Bigg[& \int d\boldsymbol{r}\, \frac{\kappa}{2}\left(\frac{\hat{\rho}(\boldsymbol{r})}{\rho_0}-1\right)^2 \\ & -\frac{\nu}{3}\int d\boldsymbol{r}\, \hat{\boldsymbol{Q}}(\boldsymbol{r}):\hat{\boldsymbol{Q}}(\boldsymbol{r}) \\ & -\frac{\mu}{3}\int d\boldsymbol{r}\, \{\hat{\boldsymbol{Q}}(\boldsymbol{r}):\hat{\boldsymbol{B}}(\boldsymbol{r})+\hat{\boldsymbol{B}}(\boldsymbol{r}):\hat{\boldsymbol{Q}}(\boldsymbol{r})\} \\ & -\frac{\lambda}{4}\int d\boldsymbol{r}\, \hat{\boldsymbol{B}}(\boldsymbol{r}):\hat{\boldsymbol{B}}(\boldsymbol{r}) \Bigg], \end{aligned} \tag{1}$$

with $\hat{\boldsymbol{Q}} = \hat{\boldsymbol{Q}}^{(1)}$ for brevity.

The averaged local segment density, as well as the nematic and biaxial orientation tensors are each defined by a weighted sum (see ch. 3 and 4):

$$\begin{aligned}\hat{\Phi}_\omega(\boldsymbol{r}) &= \int d\boldsymbol{r}'\omega(|\boldsymbol{r}-\boldsymbol{r}'|)\hat{\rho}(\boldsymbol{r}'),\\ \hat{\boldsymbol{Q}}_\omega(\boldsymbol{r}) &= \int d\boldsymbol{r}'\omega(|\boldsymbol{r}-\boldsymbol{r}'|)\hat{\boldsymbol{Q}}(\boldsymbol{r}'),\\ \hat{\boldsymbol{B}}_\omega(\boldsymbol{r}) &= \int d\boldsymbol{r}'\omega(|\boldsymbol{r}-\boldsymbol{r}'|)\hat{\boldsymbol{B}}(\boldsymbol{r}'),\end{aligned} \tag{2}$$

with $\hat{\rho}(\boldsymbol{r}') = \sum\limits_{i,s}\delta(\boldsymbol{r}-\boldsymbol{r}_{i,s})$, using the short notation $\boldsymbol{r}_{i,s} = \boldsymbol{r}_i(s)$ in this appendix. The weight function $\omega(|\boldsymbol{r}|)$ is normalized,

$$\int d\boldsymbol{r}\omega(|\boldsymbol{r}|) = 1, \tag{3}$$

and its explicit form reads

$$\omega(|\boldsymbol{r}|) = \begin{cases}\frac{1}{C}, & \text{for } |\boldsymbol{r}| \leq \sigma\\ 0, & \text{otherwise}\end{cases}. \tag{4}$$

Thus, the value of the weight function is $\frac{1}{C}$ within the radius σ, and is zero outside.

The normalization yields

$$\int d\boldsymbol{r}\omega(|\boldsymbol{r}|) = \frac{4\pi\sigma^3}{3}\frac{1}{C} \overset{!}{=} 1, \tag{5}$$

and finally

$$C = \frac{4\pi\sigma^3}{3}. \tag{6}$$

Subsequently, in the energy functional (eq. 1) expressed by local interactions (i.e. by the delta-function), the quantities $\hat{\rho}(\boldsymbol{r})$, $\hat{\boldsymbol{Q}}(\boldsymbol{r})$ and $\hat{\boldsymbol{B}}(\boldsymbol{r})$ are substituted by the averaged quantities $\hat{\varPhi}_\omega(\boldsymbol{r})$, $\hat{\boldsymbol{Q}}_\omega(\boldsymbol{r})$ and $\hat{\boldsymbol{B}}_\omega(\boldsymbol{r})$.

$$
\begin{aligned}
\frac{H_{biaxial}}{k_B T} = \rho_0 \Bigg[& \int d\boldsymbol{r}\ \frac{\kappa}{2} \Bigg(\Bigg(\frac{1}{\rho_0} \int d\boldsymbol{r}' \omega(|\boldsymbol{r}-\boldsymbol{r}'|) \sum_{(i,j)} \delta(\boldsymbol{r}'-\boldsymbol{r}_{i,j}) \Bigg) - 1 \Bigg) \\
& \Bigg(\Bigg(\frac{1}{\rho_0} \int d\boldsymbol{r}'' \omega(|\boldsymbol{r}-\boldsymbol{r}''|) \sum_{(t,s)} \delta(\boldsymbol{r}''-\boldsymbol{r}_{t,s}) \Bigg) - 1 \Bigg) \\
& -\frac{\nu}{3} \int d\boldsymbol{r}\ \Bigg(\frac{1}{\rho_0} \int d\boldsymbol{r}' \omega(|\boldsymbol{r}-\boldsymbol{r}'|) \sum_{(i,j)} \delta(\boldsymbol{r}'-\boldsymbol{r}_{i,j}) \boldsymbol{q}(\boldsymbol{r}_{i,j}) \Bigg) : \\
& \Bigg(\frac{1}{\rho_0} \int d\boldsymbol{r}'' \omega(|\boldsymbol{r}-\boldsymbol{r}''|) \sum_{(t,s)} \delta(\boldsymbol{r}''-\boldsymbol{r}_{i,j}) \boldsymbol{q}(\boldsymbol{r}_{t,s}) \Bigg) \\
& -\frac{\mu}{3} \int d\boldsymbol{r}\ \Bigg\{ \Bigg(\frac{1}{\rho_0} \int d\boldsymbol{r}' \omega(|\boldsymbol{r}-\boldsymbol{r}'|) \sum_{(i,j)} \delta(\boldsymbol{r}'-\boldsymbol{r}_{i,j}) \boldsymbol{q}(\boldsymbol{r}_{i,j}) \Bigg) : \\
& \Bigg(\frac{1}{\rho_0} \int d\boldsymbol{r}'' \omega(|\boldsymbol{r}-\boldsymbol{r}''|) \sum_{(t,s)} \delta(\boldsymbol{r}''-\boldsymbol{r}_{t,s}) \boldsymbol{b}(\boldsymbol{r}_{t,s}) \Bigg) + \\
& \Bigg(\frac{1}{\rho_0} \int d\boldsymbol{r}' \omega(|\boldsymbol{r}-\boldsymbol{r}'|) \sum_{(i,j)} \delta(\boldsymbol{r}'-\boldsymbol{r}_{i,j}) \boldsymbol{q}(\boldsymbol{r}_{i,j}) \Bigg) : \\
& \Bigg(\frac{1}{\rho_0} \int d\boldsymbol{r}'' \omega(|\boldsymbol{r}-\boldsymbol{r}''|) \sum_{(t,s)} \delta(\boldsymbol{r}''-\boldsymbol{r}_{t,s}) \boldsymbol{b}(\boldsymbol{r}_{t,s}) \Bigg) \Bigg\} \\
& -\frac{\lambda}{4} \int d\boldsymbol{r}\ \Bigg(\frac{1}{\rho_0} \int d\boldsymbol{r}' \omega(|\boldsymbol{r}-\boldsymbol{r}'|) \sum_{(i,j)} \delta(\boldsymbol{r}'-\boldsymbol{r}_{i,j}) \boldsymbol{b}(\boldsymbol{r}_{i,j}) \Bigg) : \\
& \Bigg(\frac{1}{\rho_0} \int d\boldsymbol{r}'' \omega(|\boldsymbol{r}-\boldsymbol{r}''|) \sum_{(t,s)} \delta(\boldsymbol{r}''-\boldsymbol{r}_{t,s}) \boldsymbol{b}(\boldsymbol{r}_{t,s}) \Bigg) \Bigg]
\end{aligned}
\tag{7}
$$

$$
\begin{aligned}
=&\frac{\kappa}{\rho_0 2}\sum_{(i,j)}\sum_{(t,s)}\int d\boldsymbol{r}\omega(|\boldsymbol{r}-\boldsymbol{r}_{i,j}|)\omega(|\boldsymbol{r}-\boldsymbol{r}_{t,s}|)-\frac{\kappa}{2}\sum_{(i,j)}\int d\boldsymbol{r}\omega(|\boldsymbol{r}-\boldsymbol{r}_{i,j}|)\\
&-\frac{\kappa}{2}\sum_{(t,s)}\int d\boldsymbol{r}\omega(|\boldsymbol{r}-\boldsymbol{r}_{t,s}|)+\frac{\rho_0\kappa}{2}\int d\boldsymbol{r}\\
&-\frac{\nu}{\rho_0 3}\sum_{(i,j)}\sum_{(t,s)}\left[\int d\boldsymbol{r}\omega(|\boldsymbol{r}-\boldsymbol{r}_{i,j}|)\omega(|\boldsymbol{r}-\boldsymbol{r}_{t,s}|)\right]\boldsymbol{q}(\boldsymbol{r}_{i,j}):\boldsymbol{q}(\boldsymbol{r}_{t,s})\\
&-\frac{\mu}{\rho_0 2}\sum_{(i,j)}\sum_{(t,s)}\left[\int d\boldsymbol{r}\omega(|\boldsymbol{r}-\boldsymbol{r}_{i,j}|)\omega(|\boldsymbol{r}-\boldsymbol{r}_{t,s}|)\right]\\
&\times\left[\boldsymbol{q}(\boldsymbol{r}_{i,j}):\boldsymbol{b}(\boldsymbol{r}_{t,s})+\boldsymbol{b}(\boldsymbol{r}_{i,j}):\boldsymbol{q}(\boldsymbol{r}_{t,s})\right]\\
&-\frac{\lambda}{\rho_0 3}\sum_{(i,j)}\sum_{(t,s)}\left[\int d\boldsymbol{r}\omega(|\boldsymbol{r}-\boldsymbol{r}_{i,j}|)\omega(|\boldsymbol{r}-\boldsymbol{r}_{t,s}|)\right]\boldsymbol{b}(\boldsymbol{r}_{i,j}):\boldsymbol{b}(\boldsymbol{r}_{t,s})\\
=&\frac{1}{\rho_0}\sum_{(i,j)}\sum_{(t,s)}\left[\int d\boldsymbol{r}\omega(|\boldsymbol{r}-\boldsymbol{r}_{i,j}|)\omega(|\boldsymbol{r}-\boldsymbol{r}_{t,s}|)\right]\\
&\times\left[\frac{\kappa}{2}-\frac{\nu}{3}\boldsymbol{q}(\boldsymbol{r}_{i,j}):\boldsymbol{q}(\boldsymbol{r}_{t,s})\right.\\
&\left.-\frac{\mu}{3}\left(\boldsymbol{q}(\boldsymbol{r}_{i,j}):\boldsymbol{q}(\boldsymbol{r}_{t,s})+\boldsymbol{b}(\boldsymbol{r}_{i,j}):\boldsymbol{q}(\boldsymbol{r}_{t,s})\right)-\frac{\lambda}{4}\boldsymbol{b}(\boldsymbol{r}_{i,j}):\boldsymbol{b}(\boldsymbol{r}_{t,s})\right]\\
&-\frac{\kappa n N}{2}.
\end{aligned}
\tag{8}
$$

In the nVT-ensemble, the last term is constant and can be neglected in the simulation.

The expression

$$
\frac{1}{\rho_0}\int d\boldsymbol{r}\omega(|\boldsymbol{r}-\boldsymbol{r}_{i,j}|)\omega(|\boldsymbol{r}-\boldsymbol{r}_{t,s}|)\equiv u(r=|\boldsymbol{r}_{i,j}-\boldsymbol{r}_{t,s}|)
\tag{9}
$$

is, with the specific choice of the weighting function $\omega(r)$ in eq. 4, an isotropic pair potential. It can be calculated analytically, which will be shown in the following.

$\omega(|\boldsymbol{r}-\boldsymbol{r}_{i,j}|)$ and $\omega(|\boldsymbol{r}-\boldsymbol{r}_{t,s}|)$ are spheres with radius σ around the segment centers-of-masses $\boldsymbol{r}_{i,j}$ and $\boldsymbol{r}_{t,s}$.

One possibility to calculate the overlap volume is to use a coordinate frame in which the centers of the spheres lie along the x-axis, separated by a distance $r = |\boldsymbol{r}_{i,j} - \boldsymbol{r}_{t,s}|$. In Ref. [244], it has been demonstrated to decompose the overlap volume into smaller sub-volumes, which is briefly rephrased here. Assume that the vector which connects both centers-of-masses points along the x-axis (freedom of choosing a coordinate system), see Fig. 1.

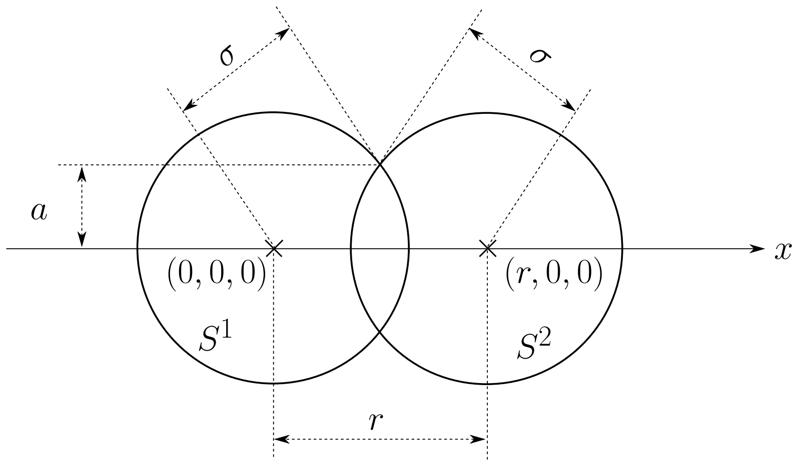

Figure 1: Scheme, illustrating a possible choice of coordinate frame in order to calculate the overlap integral eq. 9. This figure is adopted from Ref. [244].

Again, using the freedom of choosing an appropriate reference coordinate system, the origin is moved in a way that it coincides with the vector pointing along the direction connecting the centers of the two density clouds [244]. For all points in space within the area of the two spheres S^1 and S^2, the following relations hold [244]:

$$x^2 + y^2 + z^2 = \sigma^2 \text{ in } S^1, \tag{10}$$

$$(x - r)^2 + y^2 + z^2 = \sigma^2 \text{ in } S^2, \tag{11}$$

or equivalently

$$y^2 + z^2 = \sigma^2 - x^2, \tag{12}$$

$$y^2 + z^2 = \sigma^2 - (x - r)^2. \tag{13}$$

$$(12), (13) \Rightarrow \sigma^2 - x^2 = \sigma^2 - (x - r)^2 \tag{14}$$

$$\Leftrightarrow (x - r)^2 - x^2 = 0 \text{ in } S^1 \cap S^2 \tag{15}$$

$$\begin{aligned} x^2 - 2xr + r^2 - x^2 &= 0 \\ 2xr &= r^2 \\ x &= \frac{r}{2} \end{aligned} \tag{16}$$

Substituting eq. 16 in eq. 10 gives [244]

$$y^2 + z^2 = \sigma^2 - x^2 = \sigma^2 - \left(\frac{r}{2}\right)^2,$$

which is a relation that is true for all points lying on a circle with radius

$$a = \sqrt{\sigma^2 - \left(\frac{r}{2}\right)^2}. \tag{17}$$

The volume of the intersection of the spheres fixed at distance r is therefore the volume of the two spherical caps with radius a [244]. Since the radii of the spheres are equal, the volumes of the caps are equal.

The distance from the sphere center to the base of the cap is

$$r' = \frac{r}{2} \tag{18}$$

and the height of the cap is [244]

$$h = \sigma - \frac{r}{2}. \tag{19}$$

The volume of the cap can thus be written

$$V(\sigma, h) = \frac{1}{3}\pi h^2(3\sigma - h), \tag{20}$$

and the total volume of the intersection [244]

$$\begin{aligned} V(\sigma, h) &= \frac{2}{3}\pi h^2(3\sigma - h) \\ &= \frac{2}{3}\pi(2\sigma + \frac{r}{2})(\sigma - \frac{r}{2})^2 \\ &= \frac{2\pi\sigma^3}{3}(2 + \frac{r}{2\sigma})(1 - \frac{r}{2\sigma})^2. \end{aligned} \tag{21}$$

Eventually, the pair potential, i.e. eq. 9, for a pair of segments with index (i, j) and (t, s), reads [34, 244]

$$u(r) = \begin{cases} \frac{3}{8\rho_0\pi\sigma^3}\left(2 + \frac{r}{2\sigma}\right)\left(1 - \frac{r}{2\sigma}\right)^2, & \text{for } r \leq 2\sigma \\ 0, & \text{otherwise} \end{cases}. \tag{22}$$

For the special cases of minimum and maximum intersection, one finds:

$$\begin{aligned} u(2\sigma) &= 0 \\ \text{and } u(0) &= \frac{3}{4\pi\rho_0\sigma^3} = \frac{1}{\rho_0 \text{volume(sphere)}}. \end{aligned} \tag{23}$$

2 Compressibility calculations

With the system energy defined by the energy functional

$$\begin{aligned}\frac{H_{biaxial}\left[\hat{\rho},\hat{\boldsymbol{Q}},\hat{\boldsymbol{B}}\right]}{k_BT} = \rho_0 \Bigg[& \int d\boldsymbol{r}\; \frac{\kappa}{2}\left(\frac{\hat{\rho}(\boldsymbol{r})}{\rho_0}-1\right)^2 \\ & -\frac{\nu}{3}\int d\boldsymbol{r}\; \hat{\boldsymbol{Q}}(\boldsymbol{r}) : \hat{\boldsymbol{Q}}(\boldsymbol{r}) \\ & -\frac{\mu}{3}\int d\boldsymbol{r}\; \{\hat{\boldsymbol{Q}}(\boldsymbol{r}) : \hat{\boldsymbol{B}}(\boldsymbol{r}) + \hat{\boldsymbol{B}}(\boldsymbol{r}) : \hat{\boldsymbol{Q}}(\boldsymbol{r})\} \\ & -\frac{\lambda}{4}\int d\boldsymbol{r}\; \hat{\boldsymbol{B}}(\boldsymbol{r}) : \hat{\boldsymbol{B}}(\boldsymbol{r}) \Bigg], \end{aligned} \tag{24}$$

and the translational entropy of the chains, the free energy can be expressed in the mean field limit for $\nu = \mu = \lambda = 0$ by [69]

$$\frac{F}{k_BT} = V\left[\frac{\bar{\rho}}{N}\ln\left(\frac{\bar{\rho}}{N}\right) + \frac{\kappa\rho_0}{2}\left(\frac{\bar{\rho}}{\rho_0}-1\right)^2\right], \tag{25}$$

in which the contribution of the conformational entropy of the chains is neglected.

The orientational order tensors

$$\begin{aligned}\hat{Q}_{\alpha\beta}(\boldsymbol{r}) = & \frac{1}{\rho_0}\sum_{i=1}^{n}\sum_{j=1}^{N}\delta\left(\boldsymbol{r}-\boldsymbol{r}_i(j)\right)\left[\frac{3}{2}n^{(1)}_{i,\alpha}(j)n^{(1)}_{i,\beta}(j) - \frac{\delta_{\alpha\beta}}{2}\right], \\ \hat{B}_{\alpha\beta}(\boldsymbol{r}) = & \frac{1}{\rho_0}\sum_{i=1}^{n}\sum_{j=1}^{N}\delta\left(\boldsymbol{r}-\boldsymbol{r}_i(j)\right)\left[n^{(2)}_{i,\alpha}(j)n^{(2)}_{i,\beta}(j) - n^{(3)}_{i,\alpha}(j)n^{(3)}_{i,\beta}(j)\right]\end{aligned} \tag{26}$$

can be calculated for a system with perfect biaxial order. Perfect alignment, in this case, is understood as perfect nematic order with respect to the first molecular axis,

$$\begin{aligned}
&n^{(1)}_{i,x}(j) = n^{(1)}_{i,y}(j) = 0, \\
&n^{(1)}_{i,z}(j) = 1 \qquad\qquad \forall\, i = \{1, 2, \dots\} \text{ and } \forall\, j = \{1, 2, \dots\}, \qquad (27)
\end{aligned}$$

as well as the perfect alignment of the secondary molecular axis,

$$\begin{aligned}
&n^{(2)}_{i,y}(j) = n^{(2)}_{i,z}(j) = 0, \\
&n^{(2)}_{i,x}(j) = 1 \qquad\qquad \forall\, i = \{1, 2, \dots\} \text{ and } \forall\, j = \{1, 2, \dots\}, \\
&n^{(3)}_{i,x}(j) = n^{(3)}_{i,z}(j) = 0, \\
&n^{(3)}_{i,y}(j) = 1 \qquad\qquad \forall\, i = \{1, 2, \dots\} \text{ and } \forall\, j = \{1, 2, \dots\}. \qquad (28)
\end{aligned}$$

The molecular orientation tensors are all diagonal in this case and they read

$$\begin{aligned}
\bar{\boldsymbol{q}} &= \mathrm{diag}(\bar{q}_{xx}, \bar{q}_{yy}, \bar{q}_{zz}) = \mathrm{diag}(-\frac{1}{2}, -\frac{1}{2}, 1), \\
\bar{\boldsymbol{b}} &= \mathrm{diag}(\bar{b}_{xx}, \bar{b}_{yy}, \bar{b}_{zz}) = \mathrm{diag}(1, -1, 0). \qquad (29)
\end{aligned}$$

Averaging the operators eqs. 26 over all segments in the system,

$$\begin{aligned}
\bar{\boldsymbol{Q}} &= \int \prod_{i=1}^{n} \prod_{j=1}^{N} \left(\frac{d\boldsymbol{r}_i(j)}{V} \right) \hat{\boldsymbol{Q}} = \frac{\bar{\rho}}{\rho_0} \bar{\boldsymbol{q}}, \\
\bar{\boldsymbol{B}} &= \int \prod_{i=1}^{n} \prod_{j=1}^{N} \left(\frac{d\boldsymbol{r}_i(j)}{V} \right) \hat{\boldsymbol{B}} = \frac{\bar{\rho}}{\rho_0} \bar{\boldsymbol{b}}, \qquad (30)
\end{aligned}$$

the double dot products in the functional expression eq. 24 can be calculated for the perfect biaxial state:

$$\begin{aligned}
\bar{\boldsymbol{Q}} : \bar{\boldsymbol{Q}} &= \left(\frac{\bar{\rho}}{\rho_0}\right)^2 \bar{\boldsymbol{q}} : \bar{\boldsymbol{q}} = \left(\bar{q}_{zz}^2 + \frac{\bar{q}_{zz}^2}{4} + \frac{\bar{q}_{zz}^2}{4}\right)\left(\frac{\bar{\rho}}{\rho_0}\right)^2 = \frac{3}{2}\bar{q}_{zz}^2\left(\frac{\bar{\rho}}{\rho_0}\right)^2, \\
\bar{\boldsymbol{Q}} : \bar{\boldsymbol{B}} + \bar{\boldsymbol{B}} : \bar{\boldsymbol{Q}} &= \left(\frac{\bar{\rho}}{\rho_0}\right)^2 2\, \bar{\boldsymbol{q}} : \bar{\boldsymbol{b}} = 2\left(\frac{\bar{\rho}}{\rho_0}\right)^2 \left(-\frac{\bar{q}_{zz}}{2}\bar{b}_{xx} + \frac{\bar{q}_{zz}}{2}\bar{b}_{xx}\right), \\
\bar{\boldsymbol{B}} : \bar{\boldsymbol{B}} &= \left(\frac{\bar{\rho}}{\rho_0}\right)^2 \bar{\boldsymbol{b}} : \bar{\boldsymbol{b}} = \left(\bar{b}_{xx}^2 + \bar{b}_{xx}^2\right)\left(\frac{\bar{\rho}}{\rho_0}\right)^2 = 2\bar{b}_{xx}^2\left(\frac{\bar{\rho}}{\rho_0}\right)^2. \qquad (31)
\end{aligned}$$

Eventually, the free energy of the perfectly ordered liquid can be estimated in the mean field limit,

$$\frac{F}{k_B T} = V\left[\frac{\bar{\rho}}{N}\ln\left(\frac{\bar{\rho}}{N}\right) + \frac{\kappa\rho_0}{2}\left(\frac{\bar{\rho}}{\rho_0} - 1\right)^2 - \frac{1}{2\rho_0}(\nu\bar{q}_{zz}^2 + \lambda\bar{b}_{xx}^2)\bar{\rho}^2\right]. \qquad (32)$$

The compressibility of the system can be derived with the help of the equation of state, $P = -\frac{\partial F}{\partial V}$, through the relation

$$\begin{aligned}
\frac{1}{k_B T \kappa_T} = -V\frac{\partial P}{\partial V} &= \frac{n}{\rho_0 V^2}\left(\kappa n N^2 - \lambda\bar{b}_{xx}^2 n N^2 - \nu\bar{q}_{zz}^2 n N^2 + \rho_0 V\right) \\
&= \frac{\kappa}{\rho_0}\bar{\rho}^2 - \frac{\nu\bar{q}_{zz}^2}{\rho_0}\bar{\rho}^2 - \frac{\lambda\bar{b}_{xx}^2}{\rho_0}\bar{\rho}^2 + \frac{n}{V} \\
&= \frac{\bar{\rho}}{N} + \left(\frac{\kappa}{\rho_0} - \frac{\nu\bar{q}_{zz}^2}{\rho_0} - \frac{\lambda\bar{b}_{xx}^2}{\rho_0}\right)\bar{\rho}^2. \qquad (33)
\end{aligned}$$

In the special case $\bar{\rho} = \rho_0$, this reduces to

$$\frac{1}{k_B T \kappa_T} = \frac{n}{V} + \left(\kappa - \nu\bar{q}_{zz}^2 - \lambda\bar{b}_{xx}^2\right)\rho_0. \qquad (34)$$

3 Definition of biaxial order parameters

The molecular axes $\boldsymbol{n}^{(1)}$, $\boldsymbol{n}^{(2)}$ and $\boldsymbol{n}^{(3)}$, defining the molecular orientation of a biaxial coarse-grained segment in ch. 4, form a right-handed tripod $\boldsymbol{n}^{(1)} \perp \boldsymbol{n}^{(2)} \perp \boldsymbol{n}^{(3)}$ that is rotated according to the movement of the molecule with respect to the laboratory frame.

For quantifying the collective biaxial order of segments, an order parameter that characterizes the cooperative alignment of two molecular axis has to be considered [28, 245]. Straley used in Ref. [201] four relevant order parameters in terms of Euler angles formed by three molecular axes with respect to a laboratory frame:

$$\begin{aligned}
S &= \langle \frac{1}{2}\left(3\cos^2(\theta) - 1\right)\rangle, \\
T &= \langle \sin^2(\theta)\cos(2\phi)\rangle, \\
U &= \langle \sin^2(\theta)\cos(2\psi)\rangle, \\
V &= \langle \frac{1}{2}\left(1+\cos^2(\theta)\right)\cos(2\phi)\cos(2\psi) - \cos(\theta)\sin(2\phi)\sin(2\psi)\rangle, \qquad (35)
\end{aligned}$$

for describing a biaxial phase of a system consisting of biaxial particles.

For a biaxial mesophase formed by biaxial segments, the parameters S and V are the most important measures [222]. S describes nematic order of the primary molecular axis $\boldsymbol{n}^{(1)}$ along the director $\boldsymbol{Z}$ that corresponds to the same molecular axis. One can rewrite S and V in cartesian form [222]. Imposing $|\boldsymbol{Z}| = 1$ and $|\boldsymbol{n}^{(1)}| = 1$, S can be rewritten as [221]

$$\begin{aligned} S &= \langle \frac{1}{2}\left(3\left(\boldsymbol{Z}^T\boldsymbol{n}^{(1)}\right)\left(\boldsymbol{n}^{(1)^T}\boldsymbol{Z}\right) - \boldsymbol{Z}^T\mathrm{diag}(1,1,1)\boldsymbol{Z}\right)\rangle \\ &= \langle \boldsymbol{Z}^T\left(\frac{3}{2}\boldsymbol{n}^{(1)}\boldsymbol{n}^{(1)^T} - \frac{1}{2}\mathrm{diag}(1,1,1)\right)\boldsymbol{Z}\rangle \\ &= \langle \boldsymbol{Z}^T Q^{zz}\boldsymbol{Z}\rangle. \end{aligned} \tag{36}$$

One can define similar definitions of the order matrices for the remaining two molecular axes [222],

$$\begin{aligned} Q^{xx} &= \frac{3}{2}\boldsymbol{n}^{(2)}\boldsymbol{n}^{(2)^T} - \frac{1}{2}\mathrm{diag}(1,1,1), \\ Q^{yy} &= \frac{3}{2}\boldsymbol{n}^{(3)}\boldsymbol{n}^{(3)^T} - \frac{1}{2}\mathrm{diag}(1,1,1). \end{aligned} \tag{37}$$

Subsequently, the order parameter V, which indicates the biaxial order due to the alignment of the second and third director, can be equally rewritten [222]. For a perfectly ordered biaxial system, the remaining two directors $\boldsymbol{X}$ and $\boldsymbol{Y}$, with respect to the alignment of the molecular axes $\boldsymbol{n}^{(2)}$ and $\boldsymbol{n}^{(3)}$, respectively, build an orthonormal system with Z, and V reads in cartesian form [222]

$$V = \frac{1}{3}\langle \boldsymbol{X}^T Q^{xx}\boldsymbol{X} + \boldsymbol{Y}^T Q^{yy}\boldsymbol{Y} - \boldsymbol{X}^T Q^{yy}\boldsymbol{X} - \boldsymbol{Y}^T Q^{xx}\boldsymbol{Y}\rangle. \tag{38}$$

In order to define in a biaxial system with three molecular directions the specific molecular axis for determining the order parameter S is in principle arbitrary [221].

In this thesis, the convention described by Low in Ref. [221] is used, which is a modification of the definitions used by Allen in Ref. [222]. This definition is shortly rephrased in the following.

Given a sample $\{\{\boldsymbol{n}_{1,i}, \boldsymbol{n}_{2,i}, \boldsymbol{n}_{3,i}\}\}$, with $\boldsymbol{n}_{1,i}$, $\boldsymbol{n}_{2,i}$ and $\boldsymbol{n}_{3,i}$ the molecular axes of the molecule with index i, and i running over all molecules in the system, one calculates the ensemble averages of all three orientation tensors $\boldsymbol{Q}^{xx}$, $\boldsymbol{Q}^{yy}$ and $\boldsymbol{Q}^{zz}$. The corresponding eigenvectors and eigenvalues are calculated, and

the maximum absolute eigenvalue $\lambda_{\max} = \max\{|\lambda_i|\}$ and the corresponding normalized eigenvector $\boldsymbol{v}_{\max}$ are determined, with $|\boldsymbol{v}_{\max}| = 1$.
The dyadic $Q^{\max}$, out of the three tensors $\boldsymbol{Q}^{xx}$, $\boldsymbol{Q}^{yy}$ and $\boldsymbol{Q}^{zz}$, which corresponds to $\boldsymbol{v}_{\max}$ and $\lambda_{\max}$ is taken, and the nematic order parameter

$$S = \langle \boldsymbol{v}_{\max}^T Q^{\max} \boldsymbol{v}_{\max} \rangle \tag{39}$$

is calculated. Subsequently, the remaining six eigenvalues of the remaining two dyadics are determined, and from this subset the maximum *positive* eigenvalue $\lambda_{2,\max} = \max\{\lambda_j\}$ and the corresponding eigenvector $\boldsymbol{v}_{2,\max}$ are picked. The eigenvector is projected to the plane perpendicular to $\boldsymbol{v}_{\max}$:

$$\boldsymbol{v}_{2,\max}^{\text{proj}} = \frac{\boldsymbol{v}_{2,\max} - \left(\boldsymbol{v}_{\max}^T \boldsymbol{v}_{2,\max}\right) \boldsymbol{v}_{\max}}{\left|\boldsymbol{v}_{2,\max} - \left(\boldsymbol{v}_{\max}^T \boldsymbol{v}_{2,\max}\right) \boldsymbol{v}_{\max}\right|}. \tag{40}$$

The set of directors is then completed to a right-handed orthonormal system with $\boldsymbol{v}_{3,\max}^{\text{proj}}$, by evaluating the cross product

$$\boldsymbol{v}_{3,\max}^{\text{proj}} = \boldsymbol{v}_{\max} \times \boldsymbol{v}_{2,\max}^{\text{proj}}. \tag{41}$$

The biaxial order parameter V is eventually calculated as

$$\begin{aligned} V = \frac{1}{3} \langle & \boldsymbol{v}_{2,\max}^{\text{proj}} Q^{\text{2nd}} \boldsymbol{v}_{2,\max}^{\text{proj}} + \boldsymbol{v}_{3,\max}^{\text{proj}} Q^{\text{3rd}} \boldsymbol{v}_{3,\max}^{\text{proj}} \\ & - \boldsymbol{v}_{2,\max}^{\text{proj}} Q^{\text{3rd}} \boldsymbol{v}_{2,\max}^{\text{proj}} - \boldsymbol{v}_{3,\max}^{\text{proj}} Q^{\text{2nd}} \boldsymbol{v}_{3,\max}^{\text{proj}} \rangle. \end{aligned} \tag{42}$$

4 Local coordinate system

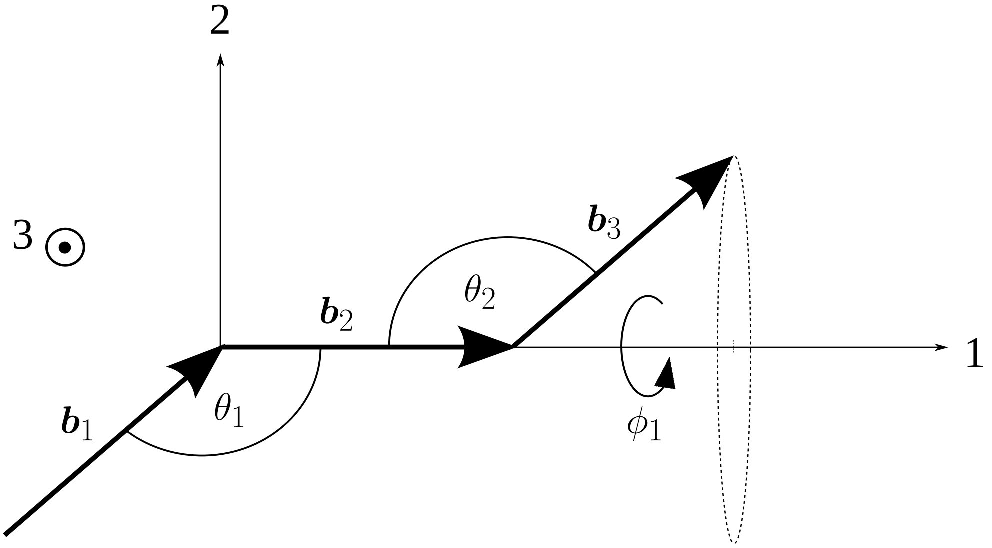

Figure 2: Scheme, illustrating the local coordinate frame used for the sampling of reptation moves according to the bonded potentials. The labeling of the frame axes 1, 2 and 3 is arbitrary and denotes the frame that is fixed to the molecular orientation. The first two bond vectors, $\boldsymbol{b}_1$ and $\boldsymbol{b}_2$ lie in the 1-2-frame, while a positive ϕ moves the bond vector $\boldsymbol{b}_3$ towards the positive 3-axis out of the plane.

The figure shows the choice of a local molecular coordinate frame for the sampling of the bond vectors in ch. 4, using the labeling and convention of the dihedral angle given by Flory [17]. A dihedral angle $\phi = 0$ therefore defines the *trans*-configuration of the three consecutive bonds $\boldsymbol{b}_1$, $\boldsymbol{b}_2$ and $\boldsymbol{b}_3$. The transformation to the molecular frame facilitates significantly the sampling of bond vectors in a reptation (or in general a more complex) update move according to the bonded potentials [215, 246]. In the following calculation, the length of the bonds are kept explicitly. However, in the simulation the bonds are unit vectors and therefore have equal lengths.

The bond vectors $\boldsymbol{b}_1$ and $\boldsymbol{b}$ are assumed to lie in the 1-2-plane. Thus, one can write all three bond vectors explicitly in terms of two bond vectors θ_1, θ_2 and the dihedral angle ϕ:

$$\begin{aligned}
\boldsymbol{b}_1 &= \begin{pmatrix} b_1 \cos(\pi - \theta_1) \\ b_1 \sin(\pi - \theta_1) \\ 0 \end{pmatrix} = \begin{pmatrix} -b_1 \cos(\theta_1) \\ b_1 \sin(\theta_1) \\ 0 \end{pmatrix}, \\
\boldsymbol{b}_2 &= \begin{pmatrix} b_2 \\ 0 \\ 0 \end{pmatrix}, \\
\boldsymbol{b}_3 &= \begin{pmatrix} b_3 \cos(\pi - \theta_2) \\ b_3 \sin(\pi - \theta_2) \cos(\phi) \\ b_3 \sin(\pi - \theta_2) \sin(\phi) \end{pmatrix} = \begin{pmatrix} -b_3 \cos(\theta_2) \\ b_3 \sin(\theta_2) \cos(\phi) \\ b_3 \sin(\theta_2) \end{pmatrix}. \qquad (43)
\end{aligned}$$

The third, out-of-plane bond $\boldsymbol{b}_3$ can be expanded in the basis $\{\boldsymbol{b}_1, \boldsymbol{b}_2, \boldsymbol{b}_1 \times \boldsymbol{b}_2\}$,

$$\boldsymbol{b}_3 = a\, \boldsymbol{b}_1 + b\, \boldsymbol{b}_2 + c\, \left[\boldsymbol{b}_1 \times \boldsymbol{b}_2\right]. \qquad (44)$$

Scalar products of $\boldsymbol{b}_3$ with the remaining two bond vectors, using the expansion in eq. 44, read:

$$\begin{aligned}
(\boldsymbol{b}_3 \cdot \boldsymbol{b}_1) &= a\, b_1^2 + b\, (\boldsymbol{b}_2 \cdot \boldsymbol{b}_1), \\
(\boldsymbol{b}_3 \cdot \boldsymbol{b}_2) &= a\, (\boldsymbol{b}_1 \cdot \boldsymbol{b}_2) + b\, b_2^2. \qquad (45)
\end{aligned}$$

From a substitution of the explicit initial definitions in terms of the three angles it follows that

$$\begin{aligned}
\boldsymbol{b}_1 \cdot \boldsymbol{b}_2 &= -b_1 b_2 \cos(\theta_1), \\
\boldsymbol{b}_3 \cdot \boldsymbol{b}_1 &= b_1 b_3 \cos(\theta_1) \cos(\theta_2) + b_1 b_3 \sin(\theta_1) \sin(\theta_2) \cos(\phi), \\
\boldsymbol{b}_3 \cdot \boldsymbol{b}_2 &= -b_2 b_3 \cos(\theta_2). \qquad (46)
\end{aligned}$$

This defines a set of linear equations,

$$\begin{aligned} b_1b_3\cos(\theta_1)\cos(\theta_2) + b_1b_3\sin(\theta_1)\sin(\theta_2)\cos(\phi) = &\quad a\, b_1^2 - b\, b_1b_2\cos(\theta_1) \\ -b_2b_3\cos(\theta_2) = &\quad -a\, b_1b_2\cos(\theta_1) + b\, b_2^2, \end{aligned}$$

$$\begin{pmatrix} b_1^2 & -b_1b_2\cos(\theta_1) \\ -b_1b_2\cos(\theta_1) & b_2^2 \end{pmatrix} \begin{pmatrix} a \\ b \end{pmatrix}$$

$$= \begin{pmatrix} b_1b_3(\cos(\theta_1)\cos(\theta_2) + \sin(\theta_1)\sin(\theta_2)\cos(\phi) \\ -b_2b_3\cos(\theta_2) \end{pmatrix}. \tag{47}$$

The solution gives the three vector components of $\boldsymbol{b}_3$ in the basis $\{\boldsymbol{b}_1, \boldsymbol{b}_2, \boldsymbol{b}_1 \times \boldsymbol{b}_2\}$:

$$\begin{aligned} a &= (b_3\cos(\phi)\csc(\theta_1)\sin(\theta_2))/b_1 \\ b &= (-b_3\cos(\theta_2) + b_3\cos(\phi)\cot(\theta_1)\sin(\theta_2))/b_2 \\ c &= (b_3\csc(\theta_1)\sin(\phi)\sin(\theta_2))/(b_1b_2) \end{aligned} \tag{48}$$

Acknowledgements

This thesis would not have been possible without the support and encouragement from many collaborators, colleagues and friends, whom I would like to thank.

First of all, I am deeply grateful to my supervisor Prof. Kurt Kremer for the opportunity to join the Theory Group of the Max-Planck-Institute for Polymer Research in Mainz. I thank him for his many ideas and suggestions concerning my doctoral project. It has been a great experience over the past years.

I would like to thank Prof. Ulrich Schwarz for acting as a second referee of this thesis, as well as all committee members for their effort.

I am grateful to my project leader and direct supervisor Dr. Kostas Daoulas for the time he spent sharing his knowledge and ideas in order to push the project forward.

I thank the MORPHEUS project team within the InnovationLab GmbH in Heidelberg for collaborations and interesting discussions.

During the last three years, I very much enjoyed the inspiring atmosphere and the collaborations with colleagues in the Theory Group. Among them, I would like to especially point out Carl Poelking, whom I owe many thanks not only for his help with technical questions but also for his valuable advice from which I have learned a lot. Furthermore, I would like to thank Dr. Denis Andrienko for the collaboration, which I very much enjoyed.

I met many colleagues and friends during the time spent on my doctoral project at the MPIP in Mainz. Among them, I would like to mention Konstantin Koschke, Olga Bezkorovaynaya, Rengin Peköz, Gustav Waschatko, Sang-

hamitra Neogi, Sebastian Fritsch, Jens Kahlen, Guojie Zhang, Livia Moreira, Senbo Xiao, Jens Wehner, Nikita Tretyakov, Anton Melnyk and Pascal Kordt. I thank Claudia Mangold for the time sharing the office and for her friendship. Finally, I thank my family and Michèle for their love and support.

Bibliography

[1] Gemünden, P.; Poelking, C.; Kremer, K.; Andrienko, D.; Daoulas, K. C. *Macromolecules*, **2013**, *46*, 5762–5774.

[2] Gemünden, P.; Daoulas, K. C. *Soft Matter*, **2014**, *11*, 532–544.

[3] Gemünden, P.; Poelking, C.; Kremer, K.; Daoulas, K. C.; Andrienko, D. *accepted for publication in: Macromolecular Rapid Communications*, **2015**, *DOI: 10.1002/marc.201400725*.

[4] Allen, M. P.; Tildesley, D. J. *Computer Simulation of Liquids*. Oxford University Press, 1987.

[5] Alberts, B.; Johnson, A.; Lewis, J.; Raff, M.; Roberts, K.; Walter, P. *Molecular Biology of the Cell*. Garland Science, 4th edition, 2002.

[6] Wang, Z.-J.; Deserno, M. *J. Phys. Chem. B*, **2010**, *114*, 11207–11220.

[7] Reynwar, B. J.; Illya, G.; Harmandaris, V. A.; Müller, M. M.; Kremer, K.; Deserno, M. *Nature*, **2007**, *447*, 461–464.

[8] Tschöp, W.; Kremer, K.; Hahn, O.; Batoulis, J.; Bürger, T. *Acta Polymerica*, **1998**, *49*, 75–79.

[9] Tschöp, W.; Kremer, K.; Batoulis, J.; Bürger, T.; Hahn, O. *Acta Polymerica*, **1998**, *49*, 61–74.

[10] Müller-Plathe, F. *ChemPhysChem*, **2002**, *3*, 754–769.

[11] Reith, D.; Pütz, M.; Müller-Plathe, F. *J. Comp. Chem.*, **2003**, *24*, 1624–1636.

[12] Izvekov, S.; Voth, G. A. *J. Phys. Chem. B*, **2005**, *109*, 2469–2473.

[13] Noid, W. G.; Chu, J.-W.; Ayton, G. S.; Krishna, V.; Izvekov, S.; Voth, G. A.; Das, A.; Andersen, H. C. *The Journal of Chemical Physics*, **2008**, *128*, 244114.

[14] Peter, C.; Kremer, K. *Soft Matter*, **2009**, *5*, 4357–4366.

[15] Noid, W. G. Methods in Molecular Biology. Humana Press, 2013.

[16] Louis, A. A. *J. Phys.: Condens. Matter*, **2002**, *14*, 9187.

[17] Flory, P. J. *Principles of Polymer Chemistry*. Cornell University Press, 1953.

[18] Doi, M.; Edwards, S. F. *The theory of polymer dynamics*. Clarendon Press ; Oxford University Press, Oxford [Oxfordshire]; New York, 1987.

[19] Cotton, J. P.; Decker, D.; Benoit, H.; Farnoux, B.; Higgins, J.; Jannink, G.; Ober, R.; Picot, C.; des Cloizeaux, J. *Macromolecules*, **1974**, *7*, 863–872.

[20] Daoud, M.; Cotton, J. P.; Farnoux, B.; Jannink, G.; Sarma, G.; Benoit, H.; Duplessix, C.; Picot, C.; de Gennes, P. G. *Macromolecules*, **1975**, *8*, 804–818.

[21] de Gennes, P.-G. *Scaling Concepts in Polymer Physics*. Cornell University Press, 1979.

[22] des Cloizeaux, J.; Jannink, G. *Polymers in Solution: Their Modelling and Structure*. OUP Oxford, 2010.

[23] Evans, R. in *Fundamentals of Inhomogeneous Fluids*, Henderson, D., Ed. Marcel Dekker, Inc., New York, 1992.

[24] Hansen, J.-P.; McDonald, I. R. *Theory of Simple Liquids: with Applications to Soft Matter*. Academic Press, Elsevier, Oxford, UK, 4th edition, 2013.

[25] de Gennes, P. G.; Prost, J. *The Physics of Liquid Crystals*. Clarendon Press, Oxford, 1995.

[26] Hołyst, R.; Vilgis, T. A. *Macromol. Theory Simul.*, **1996**, *5*, 573–643.

[27] Matteis, G. D.; Sonnet, A. M.; Virga, E. G. *Continuum Mech. Thermodyn.*, **2008**, *20*, 347–374.

[28] Zannoni, C. in *Polarized Spectroscopy of Ordered Systems*, Samori', B.; Thulstrup, E. W., Eds., NATO ASI Series, pp 57–83. Springer Netherlands, 1988.

[29] Laradji, M.; Guo, H.; Zuckermann, M. J. *Phys. Rev. E*, **1994**, *49*, 3199–3206.

[30] Daoulas, K. C.; Müller, M. *The Journal of Chemical Physics*, **2006**, *125*, 184904–184904–18.

[31] Daoulas, K. C.; Müller, M.; de Pablo, J. J.; Nealey, P. F.; Smith, G. D. *Soft Matter*, **2006**, *2*, 573.

[32] Pike, D. Q.; Detcheverry, F. A.; Müller, M.; de Pablo, J. J. *The Journal of Chemical Physics*, **2009**, *131*, 084903.

[33] Detcheverry, F. A.; Pike, D. Q.; Nealey, P. F.; Müller, M.; de Pablo, J. J. *Faraday Discussions*, **2010**, *144*, 111.

[34] Müller, M. *Journal of Statistical Physics*, **2011**, *145*, 967–1016.

[35] Daoulas, K. C. *Bridging particle-based and field theoretical representations for modelling complex fluids*. Habilitation thesis, Georg-August-Universität Göttingen, Göttingen, 2011.

[36] Yin, W.; Dadmun, M. *ACS Nano*, **2011**, *5*, 4756–4768.

[37] Kline, R. J.; McGehee, M. D.; Kadnikova, E. N.; Liu, J.; Fréchet, J. M. J.; Toney, M. F. *Macromolecules*, **2005**, *38*, 3312–3319.

[38] Pascui, O. F.; Lohwasser, R.; Sommer, M.; Thelakkat, M.; Thurn-Albrecht, T.; Saalwächter, K. *Macromolecules*, **2010**, *43*, 9401–9410.

[39] Murtola, T.; Bunker, A.; Vattulainen, I.; Deserno, M.; Karttunen, M. *Phys. Chem. Chem. Phys.*, **2009**, *11*, 1869–1892.

[40] Deserno, M.; Kremer, K.; Paulsen, H.; Peter, C.; Schmid, F. in *From Single Molecules to Nanoscopically Structured Materials*, Basché, T.; Müllen, K.; Schmidt, M., Eds., Advances in Polymer Science, pp 237–283. Springer International Publishing, 2013.

[41] Noid, W. G. *The Journal of Chemical Physics*, **2013**, *139*, 090901.

[42] Potestio, R.; Peter, C.; Kremer, K. *Entropy*, **2014**, *16*, 4199–4245.

[43] Ehrenfest, P.; Ehrenfest, T. *Begriffliche Grundlagen der statistischen Auffassung in der Mechanik*. Encyklopädie Der mathematischen Wissenschaften, Nr. 4. Teubner, Leipzig, 1912.

[44] Rühle, V.; Junghans, C.; Lukyanov, A.; Kremer, K.; Andrienko, D. *J. Chem. Theory Comput.*, **2009**, *5*, 3211–3223.

[45] Likos, C. N. *Physics Reports*, **2001**, *348*, 267–439.

[46] Ercolessi, F.; Adams, J. B. *EPL*, **1994**, *26*, 583.

[47] Hess, B.; Kutzner, C.; van der Spoel, D.; Lindahl, E. *J. Chem. Theory Comput.*, **2008**, *4*, 435–447.

[48] Plimpton, S.; Crozier, P.; Thompson, A. *Sandia National Laboratories*, **2007**.

[49] Limbach, H. J.; Arnold, A.; Mann, B. A.; Holm, C. *Computer Physics Communications*, **2006**, *174*, 704–727.

[50] Halverson, J. D.; Brandes, T.; Lenz, O.; Arnold, A.; Bevc, S.; Starchenko, V.; Kremer, K.; Stuehn, T.; Reith, D. *Computer Physics Communications*, **2013**, *184*, 1129–1149.

[51] Noid, W. G.; Chu, J.-W.; Ayton, G. S.; Voth, G. A. *J. Phys. Chem. B*, **2007**, *111*, 4116–4127.

[52] Fritsch, S. *Scale bridging concepts in molecular simulation: coarse-graining and thermodynamic coupling*. PhD thesis, Johannes Gutenberg-Universität Mainz, 2013.

[53] Lyubartsev, A.; Laaksonen, A. *Physical Review E*, **1995**, *52*, 3730–3737.

[54] Rühle, V.; Kirkpatrick, J.; Kremer, K.; Andrienko, D. *phys. stat. sol. (b)*, **2008**, *245*, 844–848.

[55] Jochum, M.; Andrienko, D.; Kremer, K.; Peter, C. *The Journal of Chemical Physics*, **2012**, *137*, 064102–064102–9.

[56] Hirschfelder, J. O.; Curtiss, C. F.; Bird, R. B. *Molecular theory of gases and liquids*. Structure of matter series. John Wiley & Sons, Inc., New York, 1954.

[57] Chandler, D. *Introduction to modern statistical mechanics*. Oxford University Press, New York, 1987.

[58] Soper, A. K. *Chemical Physics*, **1996**, *202*, 295–306.

[59] Henderson, R. L. *Physics Letters A*, **1974**, *49*, 197–198.

[60] Shell, M. S. *The Journal of Chemical Physics*, **2008**, *129*, 144108.

[61] Chaimovich, A.; Shell, M. S. *The Journal of Chemical Physics*, **2011**, *134*, 094112.

[62] Praprotnik, M.; Site, L. D.; Kremer, K. *The Journal of Chemical Physics*, **2005**, *123*, 224106.

[63] Praprotnik, M.; Site, L. D.; Kremer, K. *Annual Review of Physical Chemistry*, **2008**, *59*, 545–571.

[64] Fritsch, S.; Poblete, S.; Junghans, C.; Ciccotti, G.; Delle Site, L.; Kremer, K. *Phys. Rev. Lett.*, **2012**, *108*, 170602.

[65] Hirschfelder, J. O.; McClure, F. T.; Weeks, I. F. *The Journal of Chemical Physics*, **1942**, *10*, 201–214.

[66] Jones, J. E. *Proceedings of the Royal Society A: Mathematical, Physical and Engineering Sciences*, **1924**, *106*, 463–477.

[67] Marrink, S. J.; Risselada, H. J.; Yefimov, S.; Tieleman, D. P.; de Vries, A. H. *J. Phys. Chem. B*, **2007**, *111*, 7812–7824.

[68] Rossi, G.; Monticelli, L.; Puisto, S. R.; Vattulainen, I.; Ala-Nissila, T. *Soft Matter*, **2011**, *7*, 698–708.

[69] Daoulas, K. C.; Rühle, V.; Kremer, K. *Journal of Physics: Condensed Matter*, **2012**, *24*, 284121.

[70] Kremer, K.; Grest, G. S. *The Journal of Chemical Physics*, **1990**, *92*, 5057–5086.

[71] Düchs, D.; Schmid, F. *J. Phys.: Condens. Matter*, **2001**, *13*, 4853.

[72] Cooke, I. R.; Kremer, K.; Deserno, M. *Phys. Rev. E*, **2005**, *72*, 011506.

[73] Fraaije, J. G. E. M. *The Journal of Chemical Physics*, **1993**, *99*, 9202–9212.

[74] Schmid, F. *J. Phys.: Condens. Matter*, **1998**, *10*, 8105.

[75] Fredrickson, G. *The Equilibrium Theory of Inhomogeneous Polymers*. International series of monographs on physics. Oxford University Press, 2006.

[76] Müller, M.; de Pablo, J. J. *Annual Review of Materials Research*, **2013**, *43*, 1–34.

[77] Landau, L. D.; Ginzburg, V. L. *Zh. Eksp. Teor. Fiz.*, **1950**, *20*, 1064.

[78] Flory, P. J. *The Journal of Chemical Physics*, **1942**, *10*, 51–61.

[79] Huggins, M. L. *The Journal of Chemical Physics*, **1941**, *9*, 440–440.

[80] Chen, L.-Q. *Annual Review of Materials Research*, **2002**, *32*, 113–140.

[81] Cahn, J. W.; Hilliard, J. E. *The Journal of Chemical Physics*, **1958**, *28*, 258–267.

[82] Chaikin, P. M.; Lubensky, T. C. *Principles of Condensed Matter Physics*. Cambridge University Press, 1995.

[83] Baeurle, S. A. *J Math Chem*, **2008**, *46*, 363–426.

[84] Edwards, S. F. *Proc. Phys. Soc.*, **1965**, *85*, 613.

[85] Soga, K. G.; Guo, H.; Zuckermann, M. J. *EPL*, **1995**, *29*, 531.

[86] Soga, K. G.; Zuckermann, M. J.; Guo, H. *Macromolecules*, **1996**, *29*, 1998–2005.

[87] Besold, G.; Guo, H.; Zuckermann, M. J. *J. Polym. Sci. B Polym. Phys.*, **2000**, *38*, 1053–1068.

[88] Eastwood, J. W.; Hockney, R. W.; Lawrence, D. N. *Computer Physics Communications*, **1980**, *19*, 215–261.

[89] Deserno, M.; Holm, C. *The Journal of Chemical Physics*, **1998**, *109*, 7678–7693.

[90] Deserno, M.; Holm, C. *The Journal of Chemical Physics*, **1998**, *109*, 7694–7701.

[91] Gemünden, P.; Behringer, H. *The Journal of Chemical Physics*, **2013**, *138*, 024904.

[92] Poniewierski, A.; Hołyst, R. *Phys. Rev. Lett.*, **1988**, *61*, 2461–2464.

[93] Detcheverry, F. A.; Pike, D. Q.; Nealey, P. F.; Müller, M.; de Pablo, J. J. *Phys. Rev. Lett.*, **2009**, *102*, 197801.

[94] Ramírez-Hernández, A.; Müller, M.; Pablo, J. J. d. *Soft Matter*, **2013**, *9*, 2030–2036.

[95] Oseen, C. W. *Trans. Faraday Soc.*, **1933**, *29*, 883–899.

[96] Frank, F. C. *Discuss. Faraday Soc.*, **1958**, *25*, 19–28.

[97] Zheng-Min, S.; Kléman, M. *Molecular Crystals and Liquid Crystals*, **1984**, *111*, 321–328.

[98] Kléman, M. *Faraday Discuss. Chem. Soc.*, **1985**, *79*, 215–224.

[99] Frezzato, D.; Moro, G. J.; Tittelbach, M.; Kothe, G. *The Journal of Chemical Physics*, **2003**, *119*, 4060–4069.

[100] Kléman, M.; Lavrentovich, O. D. *Soft Matter Physics: An Introduction*. Springer Science & Business Media, 2003.

[101] de Gennes, P. G. *Molecular Crystals and Liquid Crystals*, **1976**, *34*, 177–182.

[102] de Gennes, P. G. in *Polymer Liquid Crystals*, Ciferri, A.; Krigbaum, W. R.; Meyer, R. B., Eds. Academic Press, New York, 1982.

[103] Meyer, R. B. in *Polymer Liquid Crystals*, Ciferri, A.; Krigbaum, W. R.; Meyer, R. B., Eds. Academic Press, New York, 1982.

[104] Le Doussal, P.; Nelson, D. R. *EPL*, **1991**, *15*, 161.

[105] Kamien, R. D.; Le Doussal, P.; Nelson, D. R. *Phys. Rev. A*, **1992**, *45*, 8727–8750.

[106] Kamien, R. D.; Le Doussal, P.; Nelson, D. R. *Phys. Rev. E*, **1993**, *48*, 4116–4117.

[107] Selinger, J. V.; Bruinsma, R. F. *Phys. Rev. A*, **1991**, *43*, 2910–2921.

[108] Nelson, D. R. *Physica A: Statistical Mechanics and its Applications*, **1991**, *177*, 220–232.

[109] Gay, J. G.; Berne, B. J. *The Journal of Chemical Physics*, **1981**, *74*, 3316–3319.

[110] Berardi, R.; Fava, C.; Zannoni, C. *Chemical Physics Letters*, **1995**, *236*, 462–468.

[111] Allen, M. P.; Warren, M. A.; Wilson, M. R.; Sauron, A.; Smith, W. *The Journal of Chemical Physics*, **1996**, *105*, 2850–2858.

[112] Lebwohl, P. A.; Lasher, G. *Phys. Rev. A*, **1972**, *6*, 426–429.

[113] Romano, S. *International Journal of Modern Physics B*, **1998**, *12*, 2305–2323.

[114] Luckhurst, G. R.; Romano, S. *Liquid Crystals*, **1999**, *26*, 871–884.

[115] Forster, D. *Annals of Physics*, **1974**, *84*, 505–534.

[116] Vroege, G. J.; Odijk, T. *Macromolecules*, **1988**, *21*, 2848–2858.

[117] Reinitzer, F. *Monatshefte für Chemie*, **1888**, *9*, 421–441.

[118] Blumstein, A. *Liquid Crystalline Order in Polymers*. Elsevier, 2012.

[119] Onsager, L. *Annals of the New York Academy of Sciences*, **1949**, *51*, 627–659.

[120] Maier, W.; Saupe, A. *Z. Naturforsch., 13a, 564–570 (1959); 14a, 882–900 (1959); 15a, 287–292 (1960)*, **1959**.

[121] Hamm, M.; Goldbeck-Wood, G.; Zvelindovsky, A. V.; Sevink, G. J. A.; Fraaije, J. G. E. M. *The Journal of Chemical Physics*, **2002**, *116*, 3152–3161.

[122] Pryamitsyn, V.; Ganesan, V. *The Journal of Chemical Physics*, **2004**, *120*, 5824–5838.

[123] Kumar, N. A.; Ganesan, V. *The Journal of Chemical Physics*, **2012**, *136*, 101101.

[124] Wang, Q. *Soft Matter*, **2011**, *7*, 3711–3716.

[125] Luckhurst, G. R.; Zannoni, C. *Nature*, **1977**, *267*, 412–414.

[126] Vink, R. L. C.; Schilling, T. *Phys. Rev. E*, **2005**, *71*, 051716.

[127] Prestipino, S.; Saija, F. *The Journal of Chemical Physics*, **2007**, *126*, 194902.

[128] Hughes, Z. E.; Stimson, L. M.; Slim, H.; Lintuvuori, J. S.; Ilnytskyi, J. M.; Wilson, M. R. *Computer Physics Communications*, **2008**, *178*, 724–731.

[129] Wilson, M. R. *International Reviews in Physical Chemistry*, **2005**, *24*, 421–455.

[130] Chandrasekhar, S. *Rep. Prog. Phys.*, **1976**, *39*, 613.

[131] Schopohl, N.; Sluckin, T. J. *Phys. Rev. Lett.*, **1987**, *59*, 2582–2584.

[132] Sonnet, A.; Kilian, A.; Hess, S. *Phys. Rev. E*, **1995**, *52*, 718–722.

[133] Taratuta, V. G.; Hurd, A. J.; Meyer, R. B. *Phys. Rev. Lett.*, **1985**, *55*, 246–249.

[134] Taratuta, V. G.; Lonberg, F.; Meyer, R. B. *Phys. Rev. A*, **1988**, *37*, 1831–1834.

[135] Ao, X.; Wen, X.; Meyer, R. B. *Physica A: Statistical Mechanics and its Applications*, **1991**, *176*, 63–71.

[136] Lee, S.-D.; Meyer, R. B. *Liquid Crystals*, **1990**, *7*, 15–29.

[137] Odijk, T. *Liquid Crystals*, **1986**, *1*, 553–559.

[138] Grosberg, A. Y.; Zhestkov, A. V. *Polymer Science U.S.S.R.*, **1986**, *28*, 97–104.

[139] Dijkstra, M.; Frenkel, D. *Phys. Rev. E*, **1994**, *50*, 349–357.

[140] Kamien, R. D.; Grest, G. S. *Phys. Rev. E*, **1997**, *55*, 1197–1200.

[141] Poelking, C.; Daoulas, K.; Troisi, A.; Andrienko, D. in *P3HT Revisited – From Molecular Scale to Solar Cell Devices*, Ludwigs, S., Ed., Advances in Polymer Science, pp 139–180. Springer Berlin Heidelberg, 2014.

[142] Winokur, M. J.; Spiegel, D.; Kim, Y.; Hotta, S.; Heeger, A. J. *Synthetic Metals*, **1989**, *28*, 419–426.

[143] Zhao, Y.; Yuan, G.; Roche, P.; Leclerc, M. *Polymer*, **1995**, *36*, 2211–2214.

[144] DeLongchamp, D. M.; Kline, R. J.; Jung, Y.; Lin, E. K.; Fischer, D. A.; Gundlach, D. J.; Cotts, S. K.; Moad, A. J.; Richter, L. J.; Toney, M. F.; Heeney, M.; McCulloch, I. *Macromolecules*, **2008**, *41*, 5709–5715.

[145] Hugger, S.; Thomann, R.; Heinzel, T.; Thurn-Albrecht, T. *Colloid Polym Sci*, **2004**, *282*, 932–938.

[146] Chabinyc, M. L. *Journal of Vacuum Science & Technology B*, **2008**, *26*, 445–457.

[147] McCulloch, I.; Heeney, M.; Bailey, C.; Genevicius, K.; MacDonald, I.; Shkunov, M.; Sparrowe, D.; Tierney, S.; Wagner, R.; Zhang, W.; Chabinyc, M. L.; Kline, R. J.; McGehee, M. D.; Toney, M. F. *Nat Mater*, **2006**, *5*, 328–333.

[148] Ho, V.; Boudouris, B. W.; Segalman, R. A. *Macromolecules*, **2010**, *43*, 7895–7899.

[149] Grell, M.; Bradley, D. D. C. *Adv. Mater.*, **1999**, *11*, 895–905.

[150] McCulloch, B.; Ho, V.; Hoarfrost, M.; Stanley, C.; Do, C.; Heller, W. T.; Segalman, R. A. *Macromolecules*, **2013**, *46*, 1899–1907.

[151] Heffner, G. W.; Pearson, D. S. *Macromolecules*, **1991**, *24*, 6295–6299.

[152] Livadaru, L.; Netz, R. R.; Kreuzer, H. J. *Macromolecules*, **2003**, *36*, 3732–3744.

[153] Levine, Y. K.; Gomes, A. E.; Martins, A. F.; Polimeno, A. *The Journal of Chemical Physics*, **2005**, *122*, 144902.

[154] Wilson, M. R. *Chem. Soc. Rev.*, **2007**, *36*, 1881–1888.

[155] Vettorel, T.; Besold, G.; Kremer, K. *Soft Matter*, **2010**, *6*, 2282–2292.

[156] Zhang, G.; Moreira, L. A.; Stuehn, T.; Daoulas, K. C.; Kremer, K. *ACS Macro Lett.*, **2014**, *3*, 198–203.

[157] Rusakov, V.; Shliomis, M. *Journal de Physique Lettres*, **1985**, *46*, 935–943.

[158] de Gennes, P. G. *The Journal of Chemical Physics*, **1971**, *55*, 572.

[159] Kremer, K.; Grest, G. S.; Carmesin, I. *Phys. Rev. Lett.*, **1988**, *61*, 566–569.

[160] Metropolis, N.; Rosenbluth, A. W.; Rosenbluth, M. N.; Teller, A. H.; Teller, E. *The Journal of Chemical Physics*, **1953**, *21*, 1087–1092.

[161] Svenšek, D.; Veble, G.; Podgornik, R. *Phys. Rev. E*, **2010**, *82*, 011708.

[162] Svenšek, D.; Grason, G. M.; Podgornik, R. *Phys. Rev. E*, **2013**, *88*, 052603.

[163] Pelletier, O.; Bourgaux, C.; Diat, O.; Davidson, P.; Livage, J. *Eur. Phys. J. E*, **2000**, *2*, 191–198.

[164] Lubensky, T. C. *Phys. Rev. A*, **1970**, *2*, 2497–2514.

[165] Allen, M. P.; Frenkel, D. *Phys. Rev. A*, **1988**, *37*, 1813–1816.

[166] O'Brien, P. A.; Allen, M. P.; Cheung, D. L.; Dennison, M.; Masters, A. *Phys. Rev. E*, **2008**, *78*, 051705.

[167] Williams, D. R.; Halperin, A. *Journal de Physique II*, **1993**, *3*, 69–89.

[168] Vives, E.; Lindgård, P.-A. *Phys. Rev. B*, **1991**, *44*, 1318–1328.

[169] Higgins, J. S.; Benoît, H. C. *Polymers and Neutron Scattering*. Clarendon Press, Oxford, 1994.

[170] McCullough, R. D. *Advanced Materials*, **1998**, *10*, 93–116.

[171] McCulloch, I.; Heeney, M.; Chabinyc, M. L.; DeLongchamp, D.; Kline, R. J.; Coelle, M.; Duffy, W.; Fischer, D.; Gundlach, D.; Hamadani, B.; Hamilton, R.; Richter, L.; Salleo, A.; Shkunov, M.; Sporrowe, D.; Tierney, S.; Zhong, W. *Adv. Mater.*, **2009**, *21*, 1091–1109.

[172] Boudreault, P.-L. T.; Najari, A.; Leclerc, M. *Chem. Mater.*, **2010**, *23*, 456–469.

[173] McCulloch, I.; Ashraf, R. S.; Biniek, L.; Bronstein, H.; Combe, C.; Donaghey, J. E.; James, D. I.; Nielsen, C. B.; Schroeder, B. C.; Zhang, W. *Acc. Chem. Res.*, **2012**, *45*, 714–722.

[174] Geoghegan, M.; Hadziioannou, G. *Polymer Electronics*. Oxford Master Series in Physics 22, 2013.

[175] Poelking, C.; Andrienko, D. *Macromolecules*, **2013**, *46*, 8941–8956.

[176] Dang, M. T.; Hirsch, L.; Wantz, G. *Adv. Mater.*, **2011**, *23*, 3597–3602.

[177] Prosa, T. J.; Winokur, M. J.; Moulton, J.; Smith, P.; Heeger, A. J. *Macromolecules*, **1992**, *25*, 4364–4372.

[178] Prosa, T. J.; Winokur, M. J.; McCullough, R. D. *Macromolecules*, **1996**, *29*, 3654–3656.

[179] Yuan, Y.; Zhang, J.; Sun, J.; Hu, J.; Zhang, T.; Duan, Y. *Macromolecules*, **2011**, *44*, 9341–9350.

[180] Noriega, R.; Rivnay, J.; Vandewal, K.; Koch, F. P. V.; Stingelin, N.; Smith, P.; Toney, M. F.; Salleo, A. *Nature Materials*, **2013**, *12*, 1038–1044.

[181] Poelking, C. *Charge-Transport Simulations in Polymeric Organic Semiconductors*. Master's Thesis, University of Heidelberg, 2013.

[182] Marcus, R. A. *The Journal of Chemical Physics*, **1956**, *24*, 966–978.

[183] Stingelin, N. *Polym. Int.*, **2012**, *61*, 866–873.

[184] Sun, K.; Xiao, Z.; Lu, S.; Zajaczkowski, W.; Pisula, W.; Hanssen, E.; White, J. M.; Williamson, R. M.; Subbiah, J.; Ouyang, J.; Holmes, A. B.; Wong, W. W. H.; Jones, D. J. *Nat Commun*, **2015**, *6*.

[185] Huang, D. M.; Faller, R.; Do, K.; Moulé, A. J. *Journal of Chemical Theory and Computation*, **2010**, *6*, 526–537.

[186] Do, K.; Huang, D. M.; Faller, R.; Moulé, A. J. *Physical Chemistry Chemical Physics*, **2010**, *12*, 14735.

[187] Schwarz, K. N.; Kee, T. W.; Huang, D. M. *Nanoscale*, **2013**, *5*, 2017–2027.

[188] Jankowski, E.; Marsh, H. S.; Jayaraman, A. *Macromolecules*, **2013**, *46*, 5775–5785.

[189] Pershin, A.; Donets, S.; Baeurle, S. A. *The Journal of Chemical Physics*, **2012**, *136*, 194102.

[190] Kremer, K.; Müller-Plathe, F. *Molecular Simulation*, **2002**, *28*, 729–750.

[191] Fukunaga, H.; Takimoto, J.; Doi, M. *The Journal of Chemical Physics*, **2002**, *116*, 8183.

[192] Fritz, D.; Harmandaris, V. A.; Kremer, K.; van der Vegt, N. F. A. *Macromolecules*, **2009**, *42*, 7579–7588.

[193] Ryckaert, J.-P.; Bellemans, A. *Faraday Discuss. Chem. Soc.*, **1978**, *66*, 95–106.

[194] Jorgensen, W. L.; Tirado-Rives, J. *Journal of the American Chemical Society*, **1988**, *110*, 1657–1666.

[195] McDonald, N. A.; Jorgensen, W. L. *The Journal of Physical Chemistry B*, **1998**, *102*, 8049–8059.

[196] DuBay, K. H.; Hall, M. L.; Hughes, T. F.; Wu, C.; Reichman, D. R.; Friesner, R. A. *J. Chem. Theory Comput.*, **2012**, *8*, 4556–4569.

[197] Hunter, C. A.; Sanders, J. K. M. *J. Am. Chem. Soc.*, **1990**, *112*, 5525–5534.

[198] Feng, X.; Marcon, V.; Pisula, W.; Hansen, M. R.; Kirkpatrick, J.; Grozema, F.; Andrienko, D.; Kremer, K.; Müllen, K. *Nat Mater*, **2009**, *8*, 421–426.

[199] Mukherjee, B.; Delle Site, L.; Kremer, K.; Peter, C. *J. Phys. Chem. B*, **2012**, *116*, 8474–8484.

[200] Freiser, M. J. *Phys. Rev. Lett.*, **1970**, *24*, 1041–1043.

[201] Straley, J. P. *Phys. Rev. A*, **1974**, *10*, 1881–1887.

[202] Sonnet, A. M.; Virga, E. G.; Durand, G. E. *Phys. Rev. E*, **2003**, *67*, 061701.

[203] Helfand, E.; Tagami, Y. *The Journal of Chemical Physics*, **1972**, *56*, 3592–3601.

[204] Helfand, E. *The Journal of Chemical Physics*, **1975**, *62*, 999–1005.

[205] Fredrickson, G. H.; Ganesan, V.; Drolet, F. *Macromolecules*, **2001**, *35*, 16–39.

[206] Düchs, D.; Schmid, F. *The Journal of Chemical Physics*, **2004**, *121*, 2798–2805.

[207] Ganesan, V.; Pryamitsyn, V. *The Journal of Chemical Physics*, **2003**, *118*, 4345–4348.

[208] Sonnet, A. M.; Virga, E. G. *Phys. Rev. E*, **2008**, *77*, 031704.

[209] Kriksin, Y. A.; Khalatur, P. G. *Macromol. Theory Simul.*, **2012**, *21*, 382–399.

[210] Luckhurst, G.; Zannoni, C.; Nordio, P.; Segre, U. *Molecular Physics*, **1975**, *30*, 1345–1358.

[211] Steele, W. A. *The Journal of Chemical Physics*, **1963**, *39*, 3197–3208.

[212] Kron, A. *Polym. Sci. USSR*, **1965**, *7*, 1361–1367.

[213] Wall, F. T.; Mandel, F. *The Journal of Chemical Physics*, **1975**, *63*, 4592–4595.

[214] Vacatello, M.; Avitabile, G.; Corradini, P.; Tuzi, A. *The Journal of Chemical Physics*, **1980**, *73*, 548–552.

[215] Dodd, L.; Boone, T.; Theodorou, D. *Molecular Physics*, **1993**, *78*, 961–996.

[216] Holtzer, A. *J. Polym. Sci.*, **1955**, *17*, 432–434.

[217] Cesar, B.; Rawiso, M.; Mathis, A.; François, B. *Synthetic Metals*, **1997**, *84*, 241–242.

[218] Hsu, H.-P.; Paul, W.; Binder, K. *Macromolecules*, **2010**, *43*, 3094–3102.

[219] Lecommandoux, S.; Chécot, F.; Borsali, R.; Schappacher, M.; Deffieux, A.; Brûlet, A.; Cotton, J. P. *Macromolecules*, **2002**, *35*, 8878–8881.

[220] Lang, A.; N Likos, C.; Watzlawek, M.; Löwen, H. *J. Phys.: Condens. Matter*, **2000**, *12*, 5087.

[221] Low, R. J. *Eur. J. Phys.*, **2002**, *23*, 111.

[222] Allen, M. P. *Liquid Crystals*, **1990**, *8*, 499–511.

[223] Eppenga, R.; Frenkel, D. *Molecular Physics*, **1984**, *52*, 1303–1334.

[224] Longa, L.; Stelzer, J.; Dunmur, D. *The Journal of Chemical Physics*, **1998**, *109*, 1555–1566.

[225] Bouhassoune, M.; Mensfoort, S. v.; Bobbert, P.; Coehoorn, R. *Organic Electronics*, **2009**, *10*, 437–445.

[226] Coehoorn, R.; Pasveer, W. F.; Bobbert, P. A.; Michels, M. A. J. *Phys. Rev. B*, **2005**, *72*, 155206.

[227] Baessler, H. *phys. stat. sol. (b)*, **1993**, *175*, 15–56.

[228] Rühle, V.; Lukyanov, A.; May, F.; Schrader, M.; Vehoff, T.; Kirkpatrick, J.; Baumeier, B.; Andrienko, D. *J. Chem. Theory Comput.*, **2011**, *7*, 3335–3345.

[229] Poelking, C.; Tietze, M.; Elschner, C.; Olthof, S.; Hertel, D.; Baumeier, B.; Würthner, F.; Meerholz, K.; Leo, K.; Andrienko, D. *Nat Mater*, **2014**, *advance online publication*.

[230] Poelking, C.; Ivanov, V.; Kremer, K.; Risko, C.; Brédas, J.-L.; Andrienko, D.; Eunkyung, C. *J. Phys. Chem. C*, **2013**, *117*, 1633–1640.

[231] Rühle, V.; Kirkpatrick, J.; Andrienko, D. *The Journal of Chemical Physics*, **2010**, *132*, 134103–134103–9.

[232] Kohler, B. E.; Woehl, J. C. *The Journal of Chemical Physics*, **1995**, *103*, 6253–6256.

[233] Schrader, M.; Körner, C.; Elschner, C.; Andrienko, D. *J. Mater. Chem.*, **2012**, *22*, 22258–22264.

[234] Schrader, M.; Fitzner, R.; Hein, M.; Elschner, C.; Baumeier, B.; Leo, K.; Riede, M.; Bäuerle, P.; Andrienko, D. *J. Am. Chem. Soc.*, **2012**, *134*, 6052–6056.

[235] Ballantyne, A. M.; Chen, L.; Dane, J.; Hammant, T.; Braun, F. M.; Heeney, M.; Duffy, W.; McCulloch, I.; Bradley, D. D. C.; Nelson, J. *Advanced Functional Materials*, **2008**, *18*, 2373–2380.

[236] Bracewell, R. N. *The Fourier transform and its applications*. McGraw-Hill series in electrical and computer engineering. McGraw Hill, Boston, 3rd ed edition, 2000.

[237] Berendsen, H. J. C.; Postma, J. P. M.; van Gunsteren, W. F.; DiNola, A.; Haak, J. R. *J. Chem. Phys.*, **1984**, *81*, 3684.

[238] Alexiadis, O.; Mavrantzas, V. G. *Macromolecules*, **2013**, *46*, 2450–2467.

[239] Poelking, C. *PhD*. PhD Thesis, University of Heidelberg, in preparation, 2015.

[240] Teixeira, P. I. C.; Osipov, M. A.; Luckhurst, G. R. *Phys. Rev. E*, **2006**, *73*, 061708.

[241] To, T. B. T.; Sluckin, T. J.; Luckhurst, G. R. *The Journal of Chemical Physics*, **2013**, *139*, 134902.

[242] Lee, C. K.; Hua, C. C.; Chen, S. A. *The Journal of Chemical Physics*, **2010**, *133*, 064902.

[243] Lee, C. K.; Hua, C. C.; Chen, S. A. *The Journal of Chemical Physics*, **2012**, *136*, 084901.

[244] Weisstein, E. W. Sphere-Sphere Intersection. From MathWorld–A Wolfram Web Resource. http://mathworld.wolfram.com/Sphere-SphereIntersection.html.

[245] Rosso, R. *Liquid Crystals*, **2007**, *34*, 737–748.

[246] Mavrantzas, V. G.; Boone, T. D.; Zervopoulou, E.; Theodorou, D. N. *Macromolecules*, **1999**, *32*, 5072–5096.